Doctoral Thesis

DUAL BEAM PULSED LASER DEPOSITION OF FUNCTIONALLY GRADED COATINGS FOR OPTICAL AND THERMAL APPLICATIONS

Chun Deng

Department of Mechanical Engineering

Graduate School of UNIST

2019

DUAL BEAM PULSED LASER DEPOSITION OF FUNCTIONALLY GRADED COATINGS FOR OPTICAL AND THERMAL APPLICATIONS

Chun Deng

Department of Mechanical Engineering

Graduate School of UNIST

DUAL BEAM PULSED LASER DEPOSITION OF FUNCTIONALLY GRADED COATINGS FOR OPTICAL AND THERMAL APPLICATIONS

A dissertation
submitted to the Graduate School of UNIST
in partial fulfillment of the
requirements for the degree of
Doctor of Philosophy

Chun Deng

12/11/2018
Approved by

Advisor
Hyungson Ki

Dual beam pulsed laser deposition of functionally graded coatings for optical and thermal applications

Chun Deng

This certifies that the thesis/dissertation of Chun Deng is approved.

12. 11. 2018

Signature
Advisor: Hyungson Ki

Signature
Committee member: Sung-Youb Kim

Signature
Committee member: Jaesung Jang

Signature
Committee member: Gun-Ho Kim

Signature
Committee member: Soon-Yong Kwon

ABSTRACT

Functional graded materials (FGMs) is a concept proposed in Japan in 1984 for a space plane project of making graded thermal barrier coatings. The basic idea is to change the compositions, microstructures continuously in the thickness direction over volume, and it results in the properties, such as conductivity, mechanical strength in gradient[1]. Over the past years, FGMs has attracted a lot of attention and a variety of applications have been realized, such as graded optical coatings, Li-ion battery separator, solar cells, thermal barrier coatings and other high-tech applications.

In this research, the author will discuss the picosecond laser dual beam pulsed laser deposition technique for several types of functional graded coating depositions for optical and thermal applications. Chapter one will be the overview part of this dissertation, we will mainly focus on the research background, motivations and literature reviews for graded functional material deposition. Many fabrication methods for thin coating deposition are introduced in this section. In chapter two we will present out research objectives and our methods, including the experimental setup - dual beam pulsed laser system with a pico/femtosecond laser combined scheme for depositing functionally graded coatings; our theoretical design of fabricating efficient and precise functional graded coatings – the pulse control scheme (attenuators are used to regulate laser beams into desirable pulses of difference lengths for accurate depositions). In chapter 3, an optical design tool for electrodynamic simulations - finite-difference time-domain (FDTD) algorithm for testing the optical coatings. It is an algorithm used for simulating electro-magnetic waves by solving the Maxwell's equations directly. Many optical characteristics can be preserved using this algorithm and accurate electromagnetic wave propagations can be obtained. In the FDTD section, an example of using FDTD for the simulations of keyholes' laser absorption is presented. In chapter 4, the design, fabrication and testing of a broadband antireflection coating for silicon based solar cell is presented. Glass-Si graded antireflection coatings are achieved by the design scheme and pulse control technique fore-mentioned, and its antireflection characteristics are measured with spectrometers and validated using FDTD simulations. In chapter 5, YSZ/SUS graded thermal barrier coating is introduced with the same fabrication techniques. Its thermal barrier effect is tested with a laser flash method with an infrared thermal camera and adhesion strength is tested with indentation cracking method. And in chapter 6, we will talk about the design, fabrication and characterization of an ultrashort focal length GRIN microlens array for NIR applicaitons combining both PLD and femtosecond laser micro-fabrication.

This research presents a novel laser pulse control scheme and pulsed laser deposition technique of some functionally graded coatings in optical or thermal applications.

TABLE OF CONTENTS

LIST OF FIGURES

LIST OF TABLES

NOMENCLATURE

Chapter I

Δd : Ablated thickness at the laser beam waist area on the target material;

R: Reflection coefficient;

τ: Pulse laser duration;

I: Intensity of the incident laser beam;

I_0: Threshold intensity of the material ablation;

ρ: Density of the bulk material;

ΔH: Evaporation latent heat of the material;

E_{th}: Threshold energy fluence of a material;

P: Background pressure in a chamber;

E: Laser energy fluence on the target surface;

D: Distance between the target and the substrate in a chamber;

r: Specific heat ratio of the elements in the plasma plume;

L: The length of the plasma plume;

Chapter II

P: Laser power;

θ: Deposited coating thickness;

b_0, b_1, b_2: Nelder model fitting coefficients;

Chapter III

ε : Permittivity of the medium;

μ : Permeability of the medium;

ρ_f : Free charge density;

J: Current density;

E: Electric field;

H: Magnetic field;

ω: Laser beam angular frequency;

E_0, H_0: Electric field and magnetic field at the beam center on the focal plane;

w_0: Beam waist;

z': Coordinate that is measured vertically from the beam waist;

$w(z')$: Beam radius at z';

$k = 2\pi / \lambda$: Wave number;

λ: Wavelength of the light;

$R(z')$: Radius of curvature of the beam's wavefront at z';

θ: Half divergence angle;

I_0: Laser intensity;

t_i: interaction time;

Chapter IV

n_1, n_2, n_{mix}: Refractive indices of material 1, material 2, and their mixture, respectively;

ϕ_1, ϕ_2: Volume fractions of material 1 and material 2;

x: Coordinate measured from the substrate surface to the given location inside the AR coating;

P: Laser power;

θ: Deposited coating thickness;

b_0, b_1, b_2: Nelder model fitting coefficients;

Chapter V

α: Denotes the physical properties of the species (density, thermal conductivity, etc.);

f: Volume fraction;

mc: Super script, stands for metallic/ceramic mixture;

m, c: Subscript, “m” or “c” stand for properties of metal or ceramic;

n_i, n_j: Number of atoms of element i and j;

I: XPS intensity;

S: Relative sensitivity factor;

Chapter VI

f: Focal length of a lens;

n: Refractive index of a material;

R: Radius of curvature at the vertex of a lens;

K: Aspherical constant of a lens;

H: Sag height of a lens;

r: Lens radius;

e: Eccentricity;

I. BACKGROUND AND MOTIVATION

1.1 Introduction of Functionally graded coating depositions

Modern technology is built up by materials, energy and modern science. And material science have gained tremendous developments over the past years[2] due to the interdisciplinary interactions and new theories, new techniques and new methods, as well as meeting the need for new applications. For the high performance and multifunction role of the demands of new materials, the functional graded materials (FGMs) concept was firstly brought up by material scientists in Japan during a project for space plane in 1984[3], for the purpose of obtaining high thermal barrier parts. Its basic idea is to tailor the internal microstructure of the composite to achieve certain desirable properties for the applications[4]. Since then this concept has drawn a lot of attention in a wide range of applications, such as thermal barrier coatings, optical coatings, electrical coatings, etc. This idea involves spatially graded materials (two or multiple) with different properties, and this not only allows people to design the materials with two or more different characteristics as they want for the final products, but also increases the number of possible material configurations for a certain design of applications[4]. Comparing with conventional materials, FGMs can provide the ability for scientists to control the deformation, dynamic response, wear, corrosion, etc. of the materials, and the ability to design for different complex environments; it also results in less residual stress and thermal stress and reduce cracking driving force[5]; most importantly, it provides the multifunctionality[6, 7]. Most commonly available FGMs are ceramic-metal composites, where the ceramic component has a high temperature and corrosion resistance and works as the thermal barrier part, while the metal has better weldability and fracture toughness[8]. Apart from the ceramic/metal configurations, metal/alloy, metal/non-metal, ceramic/non-metal, ceramic/ceramic, etc. are also possible for the FGMs, therefore a huge variety of combined properties can be achieved by mixing different materials. It is a very viable type of new materials for many practical applications.

Additionally, due to the nature of the FGMs, each end of the FGM has one constituent, and they are different from each other. This means FGMs can work as the bonding layer for two incompatible materials for better adhesion strength, it also removes the stress concentration[7, 9, 10]. FGMs can be classified into three categories in general:

(a). Functionally graded coating type, which is a graded coating deposited on the substrate with compositions in gradient;

(b). Functionally bond layer type, which is the interface layer that connects two incompatible materials;

(c). Functionally graded type, where the graded part serves as the working structure of the applications;

Based on different density gradient, FGMs can also be classified into optical FGM, composition FGM, fine FGM, etc. Based on the application fields, it can also be divided into thermal barrier FGM, biology FGM, chemical engineering FGM, electrical/magnetic FGM, etc. In Figure **1**, it shows a list of types of FGMs.

Sl.No	FGCM type	Requirements	Application
1	SiC-SiC	Corrosion resistance and hardness	Combustion chambers
2	Al-SiC	Hardness and toughness	Combustion chambers
3	SiCw/Al-alloy	Thermal resistance and chemical resistance	CNG storage cylinders, Diesel Engine pistons
4	(E-glass/epoxy	Hardness and damping properties	Brake rotors, Leaf springs
4	Al-C		Drive shafts, Hublle space telescope metering truss assembly, Turbine rotor, Turbine wheels
5	Al-SiC		Flywheels, Racing car brakes
6	SiCp/Al-alloy	High melting point, low plasticity and high hardness	Motorcycle drive sprocket, Pulleys, Torque converter reactor, Shock absorber
7	Carbon and glass fibers		Propulsion shaft
8	Glass/Epoxy		Cylindrical pressure hull, Sonar domes
9	TiAl-SiC fibers		Composite piping system, Scuba diving cylinders
10	Be-Al		Floats, Boat hulls. Wind tunnel blades, Spacecraft truss structure, Reflectors, Solar panels, Camera housing
11	Al_2O_3 /Al-alloy	Good thermal and corrosive resistance	Rocket nozzle, Wings, Rotary launchers, Engine casing
12	Carbon/Bismaleimide		Drive shaft, Propeller blades, Landing gear doors, Thrust reverser(Heat exchanger panels, Engine parts
13	Carbon/Epoxy	Lightweight and good damping properties	Helicopter components viz. Rotor drive shaft, Mast mount, Main rotor blades
14	SiCw/6061	Hard and toughness	Racing bicycle frame, Racing vehicle frame.
15	(Al-alloy/CNT),	Light weight and high stiffness	Artificial ligaments, MRI scanner cryogenic tubes, Wheelchairs, Hip joint implants, Eyeglass frames, camera tripods, Musical instruments

Figure 1. List of types of FGMs (Book: Proceedings of the 3rd international symposium on structural and functional gradient materials, 1994)

The basic concept of FGMs is shown in Figure **2** comparing with a conventional composite. For a conventional composite, two constituents are uniformly mixed together, therefore, property of

constituent 1 and property of constituent 2 keep the same level throughout the whole material volume, therefore, it is homogeneous. As for a functionally graded material, the constituents of 1 and 2 are distributed in a gradient way in space and result in a gradient of properties 1 and 2 for the material, therefore it is nonhomogeneous[11].

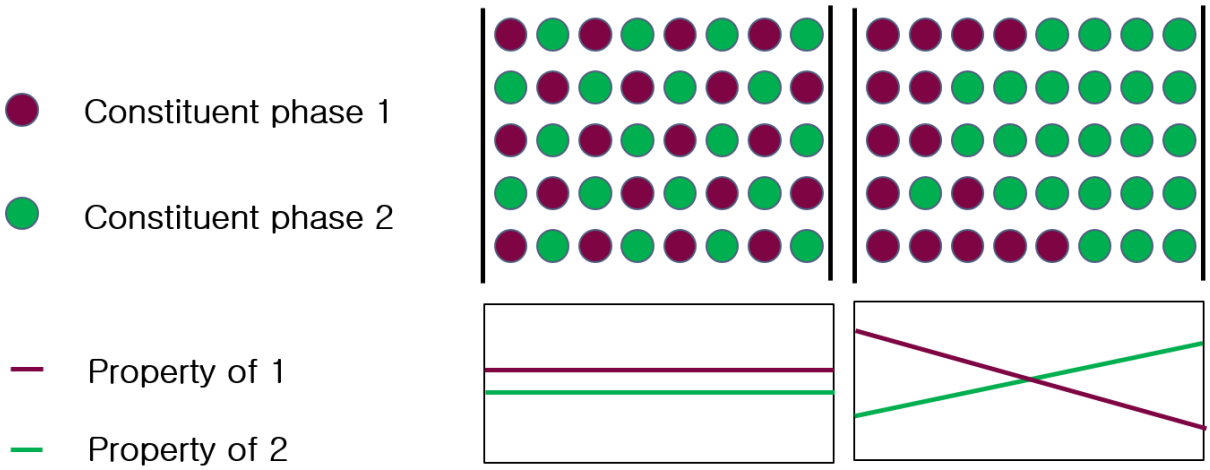

Figure 2. variation of properties in conventional composites and FGMs.

Depending on the types of the materials and the functions of the applications, there are many different physical vapor deposition (PVD) and chemical vapor deposition (CVD) fabrication methods for the functionally graded materials, but all the methods can be divided into two groups, depending on their fabrication types: mass transport or constructive processing[12, 13]. For the mass transport category, the material gradients are achieved by natural transport phenomenon such as the flow of fluid, atomic species diffusion or heat conduction[7]. For the constructive processing category, the materials are virtually built layer-by-layer with two or more materials mixing together in a way that the volume of each constituent is different in each layer and form a gradient in space over the material volume. In this category, the number of the layers can be constructed are almost unlimited, one can even design some very complex composition gradient profiles. Some of the popular techniques in this category are listed in **Figure 3**[7, 11], such as the powder metallurgy (PM), self-propagating high-temperature synthesis method (SHS) for powder stacking method; PVD or CVD, or PVD/CVD combined, plasma spray method, laser cladding method, pulsed laser deposition method, eletro-deposition method for coating depositions[7, 11-18].

Sl.NO	Process	Variability of transition function	Versatility in phase content	Type of FGM	Versatility in component geometry
1	Powder stacking	Very good	Very good	Bulk	Moderate
2	Sheet lamination	Very good	Very good	Bulk	Moderate
3	Wet powder spraying	Very good	Very good	Bulk	Moderate
4	Slurry dipping	Very good	Very good	Coating	Good
5	Jet solidification	Very good	Very good	Bulk	Very good
6	Sedimentation/centrifuging	Good	Very good	Bulk	poor
7	Filtration/slip casting	Very good	Very good	Bulk	Good
8	Laser cladding	Very good	Very good	Bulk,Coating	Very good
9	Thermal spraying	Very good	Very good	Coating ,Bulk	Good
10	Diffusion	Moderate	Very good	Joint, Coating	Good
11	Directed solidification	Moderate	Moderate	Bulk	poor
12	Electrochemical gradation	Moderate	Good	Bulk	Good
13	Foaming of polymers	Moderate	Good	Bulk	Good
14	PVD, CVD	Very good	Very good	Coating	Moderate
15	GMFC process	Very good	Moderate	Bulk	Good

Figure 3. An overview of fabrication method of FGMs

Thin film materials have also become an important subdiscipline of physics and material science over the past half century, due to the rapid developments of optoelectronics and the demands for new materials and devices for new applications. The feature sizes of devices have become smaller and smaller, for example, the size of a vacuum tube decreased from centimeter scale (in 1940s) to micrometer/nanometer scale (21st century). And this puts forward a demand for more new materials (such as FGMs) and new deposition techniques for sub-micro/nanoscale thin films.

There are multiple ways of fabricating a thin film, but the fabricating techniques can be classified into two types, physical and chemical depositions, similar to the fabricating process of FGMs fore-mentioned. Physical deposition means there are only physical changes during the deposition process, such as vacuum vapor deposition, molecular beam epitaxy (MBE), ***pulsed laser deposition***, sputtering method, etc. Chemical deposition means there are chemical reactions involved in the depositions, such as gel-sol method, chemical vapor deposition (CVD), metalorganic chemical vapor deposition, etc. Based on the state of the matter during the deposition process, the fabrication techniques can also be classified into three broad classes: vapor deposition, liquid-phase deposition and solid-state deposition. Vapor deposition is a category of fabrication methods which the target material will be vaporized and then deposited onto the substrate to form a thin film during the process, vacuum vaporization method and pulsed laser deposition etc. are included in this class. Liquid-phase deposition is a category of fabrication processes which the thin film base material along with the solution are smeared on the substrate to grow a coating directly over physical or chemical changes under heat or other types of conditions, such as spray method, gel-sol method, liquid phase epitaxial method, Langmuir-Blodgett, etc. Solid state deposition means there is a pre-grown coating on the substrate, for desired compositions, structures or properties, further moves should be taken to process the sample. Solid phase epitaxy is an example of solid state deposition. ***In this research, we will adopt the novel dual beam pulsed laser deposition for the functionally graded thin films for thermal and optical applications***.

1.2 Pulsed laser deposition (PLD)

1.2.1 Mechanisms of PLD

Shortly after the invention of the pulsed ruby laser, the first pulsed laser deposition experiment was conducted over half a century ago [19, 20] and it has become a very popular and novel deposition method for thin film deposition. When an intense pulse laser is irradiated on the surface of a target material, the material will be heated, melted and evaporated into plasma state ($T \geq 10^4$ K). The plasmas are then transported onto the substrate surface for film deposition. This process usually takes place in a vacuum chamber with/without the ambient gasses. The underlying mechanisms of PLD are multi-physical and very complex including: a. the ablation process of the target material by the laser irradiation. For short pulse lasers, the laser absorption by the target materials is usually a non-linear process; b. the development of a plasma plume with high energetic ions; c. electrons as well as neutrals and the crystalline growth of the film itself on the heated substrate. The whole pulsed laser deposition process can be divided into 4 steps:

(1). Laser ablation of the target material and creation of plasma. The target material absorbs the laser energy during laser pulse irradiation. The temperature of the target material (laser beam irradiated area) increases dramatically to melting temperature or even higher, resulting in local evaporation and sublimation of the target material. The ablated material turns into gaseous state and keeps absorb the laser energy. Then the gaseous matter is ionized by the intense laser energy and becomes dense plasma near the target surface, forming a plasma fume. The ablated material depth and laser energy input are related as follow:

$$\Delta d = [(1-R)\tau(I-I_0)]/(\rho\Delta H) \quad (1)$$

Where Δd is the ablated thickness at the laser beam waist area on the target material; R is the reflection coefficient; τ is the pulse laser duration; I is the intensity of the incident laser beam and I_0 is the threshold intensity of the material ablation, it is a parameter that related to R; ρ is the density of the bulk material and ΔH is the evaporation latent heat of the material, respectively.

(2). Dynamic of the plasma. After the plasma fume is formed, it keeps absorbing energy from the laser and keeps being ionized furtherly. The temperature and the pressure of the plasma increases drastically and a temperature and pressure gradient is formed along the normal direction from the target material surface outward, and then the plasma is expanded and ejected parallel to the normal direction isothermally (during laser pulse irradiation) and adiabatically (inbetween laser pulses). This entire process takes place within tens of nanoseconds, like a directional micro explosion, and therefore, a slender and stable plasma plume from the target material surface outward normally is generated. Its spatial shape of distribution can be governed by $\cos^n\theta$, where θ is the half divergence angle of the plasma plume at the target material surface. Depending on the types of materials, n normally ranges from $5\sim 10$.

(3). Deposition of the ablation material on the substrate. This stage is vital to determine the quality of the deposited films. The high energetic particles (E > 10 eV) emitted from the target material are bombarding the substrate surface and may cause damage to the surface by sputtering off atoms from the substrate surface but also by causing defect formation in the deposited film[21]. The sputtered species from the substrate and the particles emitted from the target form a high temperature, dense plasma collision region, which serves as a buffer for preventing the emitted particles directly hitting the substrate surface and a source for condensation of the particles. When the condensation rate is high enough, a thermal equilibrium can be reached and the film grows on the substrate surface at the expense

of the direct flow of ablation particles and the thermal equilibrium obtained. The emitted and sputtered particles flows are shown in Figure **4.**

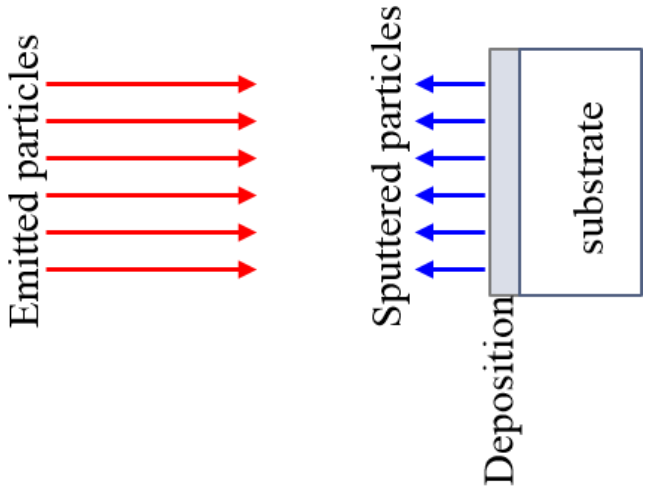

Figure 4. Emitted particles and sputtered off particles.

(4). Nucleation and growth of the thin film on the substrate surface. Due to the emitted and sputtered particles, there is a collision region near the substrate surface, therefore the particles which reaches the substrate surface through the collision region carry much less energy, and the growth of the thin film depends on these low energy particles. These low energy particles land on the surface of the substrate and form nucleus and start the nucleation. The nucleation process and growth kinetics of the coating strongly depend on several growth parameters, such as the laser parameters, substrate surface orientation, substrate surface quality, substrate surface temperature, background pressure and the ambient gasses, etc. In PLD, a large extend of supersaturation takes place on the substrate surface during the laser pulse duration. This high supersaturation induces a very large nucleation density on the surface, comparing with other types of deposition techniques and methods, such as molecular beam epitaxy or sputtering deposition. The high supersaturation forms “islands” on the film surface and will connect each other after growth. When the extend of supersaturation increases, the critical nucleus size will decrease to the radius of an atom (2D deposition), therefore higher nucleation density increases the smoothness of the deposited film.

1.2.2 Advantages of PLD

Because of the physical processes during the pulsed laser deposition, comparing with other thin coating fabrication processes, it has several advantages over other deposition methods: 1. It is suitable for multi-elements compound depositions due to its nonselective ablation feature. 2. Viable for metals, semiconductors, dielectrics and ceramics, etc. it is a superior solution for high melting point materials; 3. High quality, high performance coatings can be fabricated with PLD due to its high supersaturation for 2D growth; 4. Low requirements for substrate temperature. Some thin films with uniform orientation or single-crystal structure can be fabricated with in-situ growth at room temperature. 5. It is very easy to change the target material, therefore PLD is good for multilayer coatings fabrication and superlattice growth. Hence, we will adopt PLD as our main fabrication technique in this dissertation.

1.2.3 Factors that affect the quality of PLD deposited films

Factors which affect the quality of coatings deposited by PLD are mainly the distance between the target and the substrate D, background pressure P, laser energy fluence on the target surface E, laser repetition rate ∨and substrate temperature T, etc. Among these parameters, D, P and E are strongly associated. According to the literature, there is an optimal deposition condition empirical formula for pulsed laser deposition[22], as shown below:

$$(E - E_{th})D^{-3}P^{-1} = 8.87 \times 10^{-5}\, J/cm^5 \quad (2)$$

Where E_{th} is the threshold energy fluence of this material. Apparently, from this formula we can see, for higher P and higher D, larger E is required.

(a). Energy fluence E. Energy fluence E is a vital parameter for PLD process, and it is strongly associated with plasma generation, and has great impact on the quality of the deposited thin films. Under the conditions of chosen material type and laser wavelength, energy fluence E is the next important parameter that affects the size and density of the ejected particles from the target material. There is energy fluence threshold E_{th}, which basically means that if the energy input on the target material is below this value, the material will not be damaged and ablated, therefore, no deposition. The basic mechanism of laser and material interaction is ablation and evaporation. In order to achieve that, the laser energy fluence on the target must be larger than the threshold to generate plasma and induce the formation of evaporation layers (Knudsen layers)[23, 24]. With the same laser power, number density of emitting particles increases with decreased focused beam size on the target surface. E_{th} is generally 0.1~0.5 J/cm^2. When the input fluence is smaller than E_{th}, there is no particles deposited on the substrate. When the input fluence increases to be equal or over E_{th}, the ablation and deposition starts. With higher

energy input, higher ablation rate is realized, and higher density of plasma, higher number density of atoms which reach the substrate surface and be and deposited there is also increased. And this results in faster nucleation and finally improves the film growth rate. Although if the laser influence is too high: 1. The ejected plasma velocity will also be too high, and the energetic particles will bombard the substrate surface intensely, resulting in stronger backflow of particles from the substrate. This strong backflow effect will induce the vacancy defect to the substrate and deposited coating. 2. The temperature elevation will be very high, and the temperature difference within the beam waist will also increase, therefore, the micro explosions on the target surface become stronger, ejecting more lager size particles than evaporation, and results in low quality films. Energy fluence is the deciding factor of the species (atoms and ions) and energy level of the particles. Particle species affects the composition and structure of the coating while energy level affects the deposition rate. For PLD, a proper energy fluence of the laser should be decided carefully for the PLD process of better quality coatings. For different materials, E and E_{th} are different.

(b). Substrate temperature. The growth of a film is a recombination process of molecules, atoms and ions, and it is strongly associated with their kinetic energies and diffusion rates. Substrate temperature holds high importance of the film growth as well as the formation and elimination of defects within the deposited thin film. During a pulsed laser deposition, temperature and temperature distribution of the substrate affects both growth rate and structure of the final coating. There is no theoretical instruction of optimal substrate temperatures yet for all the materials, so one has to do experiments involving a lot of trials and errors, in order to find the optimal temperature conditions for growth of good quality films. Empirically, if the substrate temperature is too high, this might cause re-evaporation of the deposited coating, thus decreasing the deposition rate. In PLD experiments, locations of the lenses and the input of the laser power can be adjusted to obtain a well-focused bright plasma region on the target; by adjusting the distance between the substrate and the target (until the end of the plasma plume reaches the substrate surface), the optimal conditions are achieved, and it agrees with the empirical formula mentioned before. Optimal distance between target and substrate alone with the optimal energy fluence can guarantee the composition of the deposited coating is the same as the target material. Though the microstructures and quality of the deposited coating is more related to the substrate temperature.

(c). Background pressure. Background pressure mainly affects the process which the energetic particles are ejected and reach the surface of the substrate. The influences of the background pressure can be classified into two categories: 1. Ambient gas is not involved in the film growth. Under this condition, the background gas pressure only affects the kinetic energy and translational energy of the

particles, therefore the deposition rate; 2. If the ambient gas contributes to the growth of the coating, then it affects not only the deposition rate but also the compositions and micro structures of the coating itself. For example, during the deposition of an oxide thin-film, some oxygen gas is required in the chamber, it helps to reduce the oxygen vacancies inside the coating for better physical properties; but the input oxygen gas will affect the mean free path of the emitted particles. Higher gas pressure will shorten the mean free path of particles. When the mean free path is small than the distance between the target and substrate, single or multiple collisions will take place between the emitted particles and oxygen molecules. It results in atomic clusters and less smooth film surface; also, it reduces the number density and energy level of the particles, resulting lower deposition rate and lower film deposition quality.

(d). Distance between the target and the substrate. The deposited thickness of the coating at the substrate center decreases drastically with the target/substrate distance increasing, while the full width half maximum (FWHM) of the deposition increases. Maximum depth at the deposition center varies with D, and can be expressed as D^{-f}, where f is the expansion factor. For a three sphere, f=3 and for 1 dimensional line expansion, f=1. Expansion factor is a parameter which relates to the focused beam size on the target. For large size beam spot, the expansion of plasma can be simplified as 1 dimensional; if the beam size decreases, the expansion becomes a three dimensional sphere type[25, 26]. The target/substrate distance affects the angular distribution of the ejected particle flow in a vacuum chamber. The expansion rates of the plasma are anisotropic, and it affects the composition of the coating. In low vacuum condition for PLD experiments, if there is an ambient gas or D is large, the recombination of different particles tends to take place easily. Depending on the location of the substrate, there might be different particles (as in different appearance) deposited on the surface. Also, the target/substrate distance and background pressure are interconnected. When the background pressure is increased, the collision between the particles and the gas molecules becomes more intense, and the plasma plume decreases in size. The length of the plasma plume L is given by:

$$L \approx (E / P_0)^{\frac{r}{3}} \tag{3}$$

Where E is the energy fluence and P_0 is the background pressure; r is the specific heat ratio of the elements in the plasma plume. When $D \ll L$, the particle densities and plasma plume sizes are almost the same for different substrate locations; when D increases, density of small size particles also increase, and small amount of larger size particles are also formed due to recombination of the small particles during flying; when $D \gg L$, the amount of particles deposited on the substrate becomes little, the deposition rate is very low. Also, different atom species have different masses, therefore the

ejecting velocity of different atoms are different even when they have the same temperature under the irradiation of a laser beam. If the target/substrate distance D is too large, the time the particles take to reach the substrate will be vastly different. And this will affect the homogeneity of the coating. In general, we fix the distance D=4cm.

The series of studies are proposed for the study of viability of a novel deposition technique – dual beam pulsed laser deposition (PLD) for graded thin coating depositions. Two basic types of thin coatings are tested: optical and thermal barrier coatings for different applications. ***PLD*** technique along with a ***pulse control scheme*** for efficient and precise deposition will also be presented in this section. For optical thin film depositions, a ***finite-difference time-domain (FDTD)*** algorithm is also adopted for the electrodynamic simulations for the performance of the thin coatings, as a design tool as well as a validation technique. In this proposal, we will address the ***design***, ***fabrication*** and ***characterization*** of several different graded thin coating depositions: a broadband refractive-index graded antireflection coating for silicon-based solar cells (optical); a YSZ/SUS graded thermal barrier coating for high temperature applications (thermal) and fabricating ultrashort focal length micro lens array (optical) with graded coating deposition for NIR applications.

II. DUAL BEAM PULSED LASER DEPOSITION AND PULSE CONTROL SCHEME FOR FAST AND PRECISE DEPOSITIONS

2.1 Pulsed laser deposition experimental setup

In all of our experiments, we use the dual beam pulsed deposition technique for the graded coating depositions. A 355 nm wavelength, 6W picosecond laser (Coherent Talisker 355-4) was used as the main energy source. It has a Gaussian beam profile, with a repetition rate of 200 kHz and a pulse width of 10-15 ps. The pulse energy is up to 30μJ. A 50/50 reflection/transmission beam splitter is used for the main laser beam and split the beam into two with equal powers. Each split beam is controlled by a motorized attenuator (Meltrolux ML 2100), which is connected to a PC via a controller and motorized by in-house Labview programs, therefore, the intensity of each split beam is able to vary independently and simultaneously for precisely controlling the deposition process for graded coatings. Both beams are then guided into the vacuum chamber via mirrors and focused on the target materials' surfaces via plano-convex lenses. For the picosecond laser, the focused beam size on the target surface is roughly ~30μm. Each beam is focused on the target surface and generates dissimilar plasmas. The generated plasmas are naturally mixed inside the vacuum chamber and then are deposited on a cleaned substrate surface. In this manner, a graded coating with predesigned content profile can be achieved [27, 28]. The dual beam laser deposition setup scheme is shown in Figure **5**.

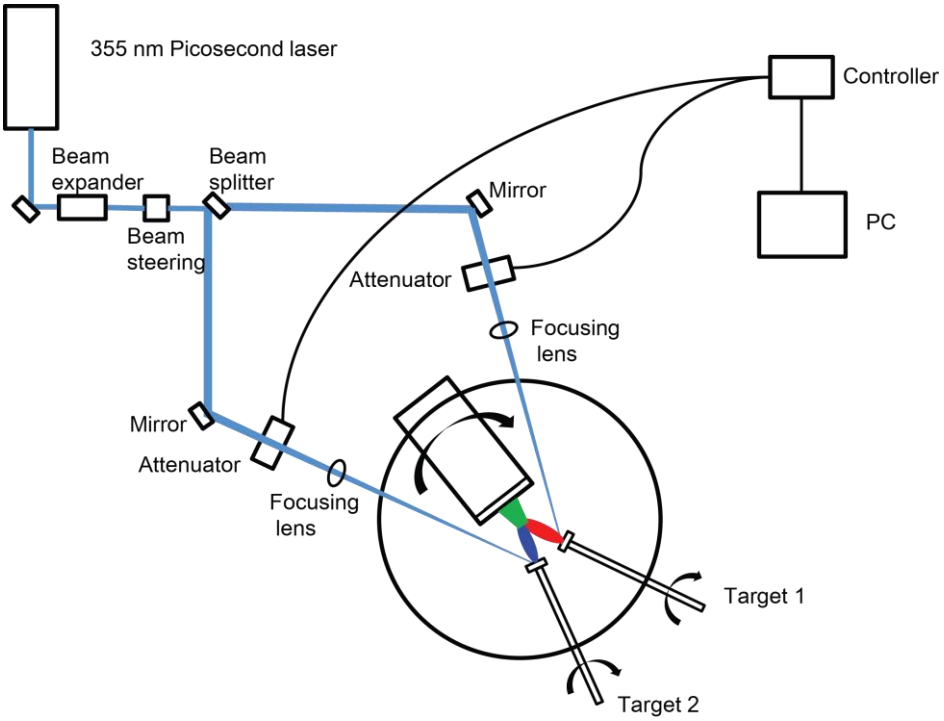

Figure 5. Schematic view of the dual beam pulsed laser deposition experimental setup.

An alternate femtosecond laser (PHAROS) is also available for the use. It is a 1030 ns wavelength femtosecond laser with a maximum power of 15W and a tunable frequency (maximum repetition rate is 200 kHz) and tunable pulse length (minimum pulse length is 220 fs). Femtosecond laser and picosecond laser are integrated together for the demands of faster and higher quality depositions. The integrated schematic of combined femtosecond and picosecond dual bean pulsed laser deposition setup is shown below in Figure **6**. Optical elements such as beam splitters, mirrors and lenses are fixed with flip mounts for more flexible optical path design. By flipping on or off the proper optical elements, the optical path opens for the femtosecond or picosecond laser. With this schematic, it is possible to do the PLD experiments with: 1. Both beams are picosecond lasers; 2. Both beams are femtosecond lasers; 3. One side is picosecond laser and the other side is femtosecond laser, in which case, it's femtosecond/picosecond laser combined.

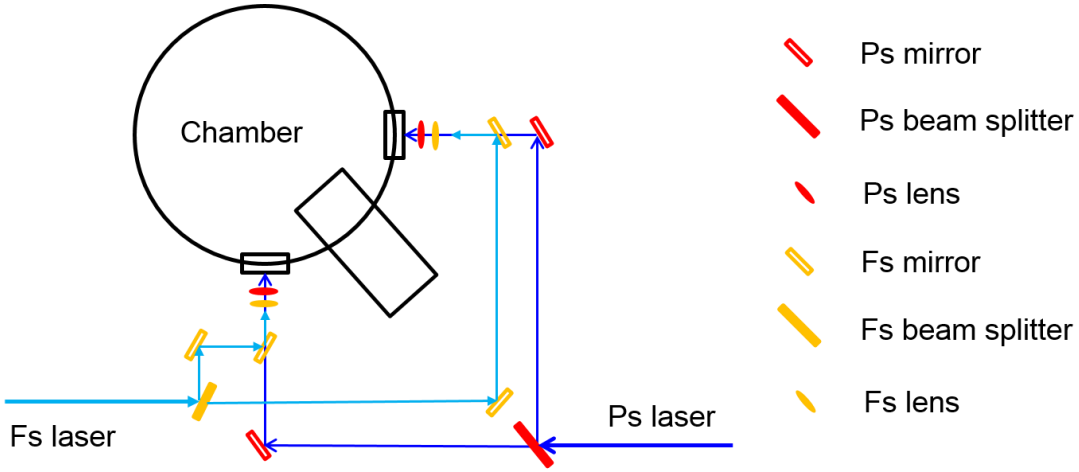

Figure 6. Schematic view of combined femtosecond and picosecond laser experimental setup.

The actual picosecond and femtosecond laser combined pulsed laser deposition system is also shown in **Figure 7**, including the vacuum chamber for depositions, two attenuators for both split beams and two beam splitters for pico and femtosecond laser, respectively. The mirrors and lenses are not labeled in this figure.

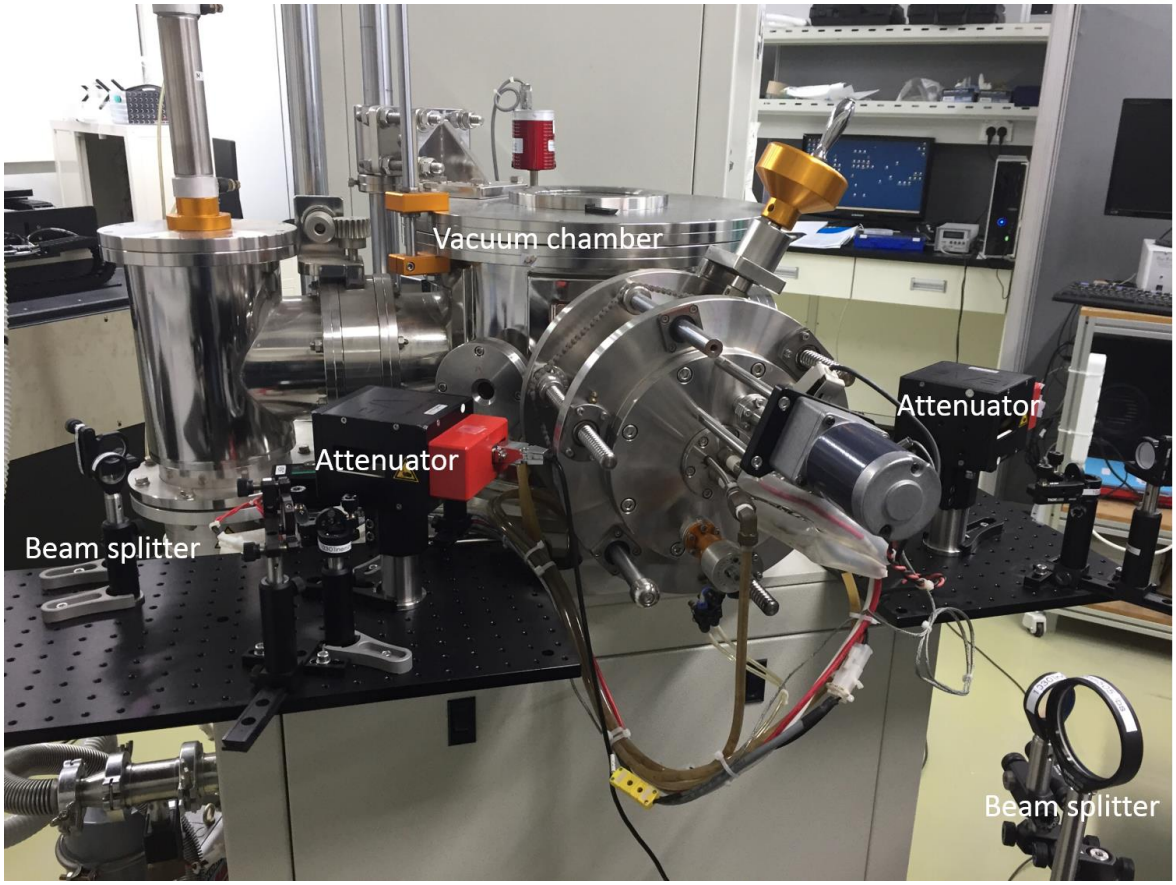

Figure 7. Actual fs/pico second laser combined PLD system.

2.2 Content profile design and pulse control scheme

The functionally graded coating can be realized by changing the composition of two or multiple materials along the coating growth direction. Before any fabrication process, the deposition rate of each material must be known precisely for the accurate design and fabrication of the graded coating. A typical deposition rate (accumulated thickness over deposition time) curve for a material is in a form of a Nelder model [29], where it is almost linear for the early stage of laser irradiation due to fast ablation, then it becomes saturated because of the defocusing effect due to the ablated materials. In reality, one often needs to shift the targets a little during depositions to overcome this issue for obtaining a continuous plasma. Nelder model is given in the form of :

$$\theta(P, t) = \frac{t}{b_0 + b_1 t + b_2 t^2} \tag{4}$$

Where θ is the deposited coating thickness and it is a function of deposition time t and deposition laser power P; b_0, b_1 and b_2 are the Nelder model fitting coefficients.

With the knowledge of the deposition data for each material, the deposition scheme can be designed and calculated. To deposit a functionally graded thin coating, firstly, we divide the whole coating thickness into several equally spaced layers. The more the layer number is, the smoother the content profile will be; but too many layers will also be a burden for calculation and Labview programming. Therefore, a proper layer number should be assigned for a smooth profile as well as a convenient design and programing. After deciding the number of layers, the thickness of each layer can be easily calculated as they are equally spaced. Now for each layer, the amounts of two target materials can also be easily calculated based on the designed content profile. From the fitted deposition data for each material, the required *effective* deposition time in each layer can also be calculated. The effective deposition time is the time required in the fabrication process to deposit the required amount of material within this layer. Since the *actual* deposition time (natural marching time) for both materials are the same, effective deposition time is always smaller or equal to the actual deposition time.

For the case of effective time smaller than the actual deposition time for one layer, the laser beam irradiation time on the target material must be reduced for a smaller amount of deposition. Therefore, we devised a method of using attenuators as laser shutters to control the effective deposition time for each material. In other word, both split beams are pulsed using the attenuators to generate the required material fluxes for the accurate coating deposition within one layer.

A more conventional way of controlling the deposition rate is by changing the laser powers at all times during depositions, which is called “Power control” method, as both high and low deposition rates are required for the accurate fabrication of the graded contents. This method requires all the deposition rates over time for all possible power values, which is impossible to be fulfilled in reality. For simplicity, only a series of deposition data curves are required to cover the whole possible range of deposition rates. For example, in order to gather the deposition data for different powers, usually the ablation threshold value (minimum power) and a maximum power value is chosen and their deposition rates over time are gathered. Apart from these two power values, at least 3 more power values are also required which should locate between the threshold and maximum powers (usually equally spaced power values). And the deposition rates over time for those powers are also gathered. For the power values which their deposition rates are unknown, their deposition rates are obtained through linear estimation, which is obtained from its nearest upper and lower known power values. Therefore, power control method not only takes a lot of time and effort in order to gather the deposition data information, but also bears considerable deposition errors, as illustrated in references [27, 30].

In this study, we adopted the "***pulse control scheme***" instead of using "Power control method". Its mechanism is shown in **Figure 8**. **Figure 8a** shows a continuous irradiation of a pulsed laser, blue pulses stand for the real laser pulses. In **Figure 8b** , an attenuator is used and it is used as a beam shutter. Word "open" stands for the shutter state being on, and the laser beam can pass through, target material is ablated and the required coating is deposited. The word "close" stands for off, and the laser beam is blocked, therefore no laser irradiates on the target, resulting in no ablation and no deposition. In **Figure 8c**, the final shaped "long pulses" are illustrated, and t1, t3 and t5 are the effective deposition times used for material depositions, and this is the basic idea of pulse control in this study. For this method, only one proper deposition data curve for one material is sufficient to build any profiles based on the pulse control technique. It is much more efficient and precise for the graded coating design and fabrication, as well as Labview programming.

`

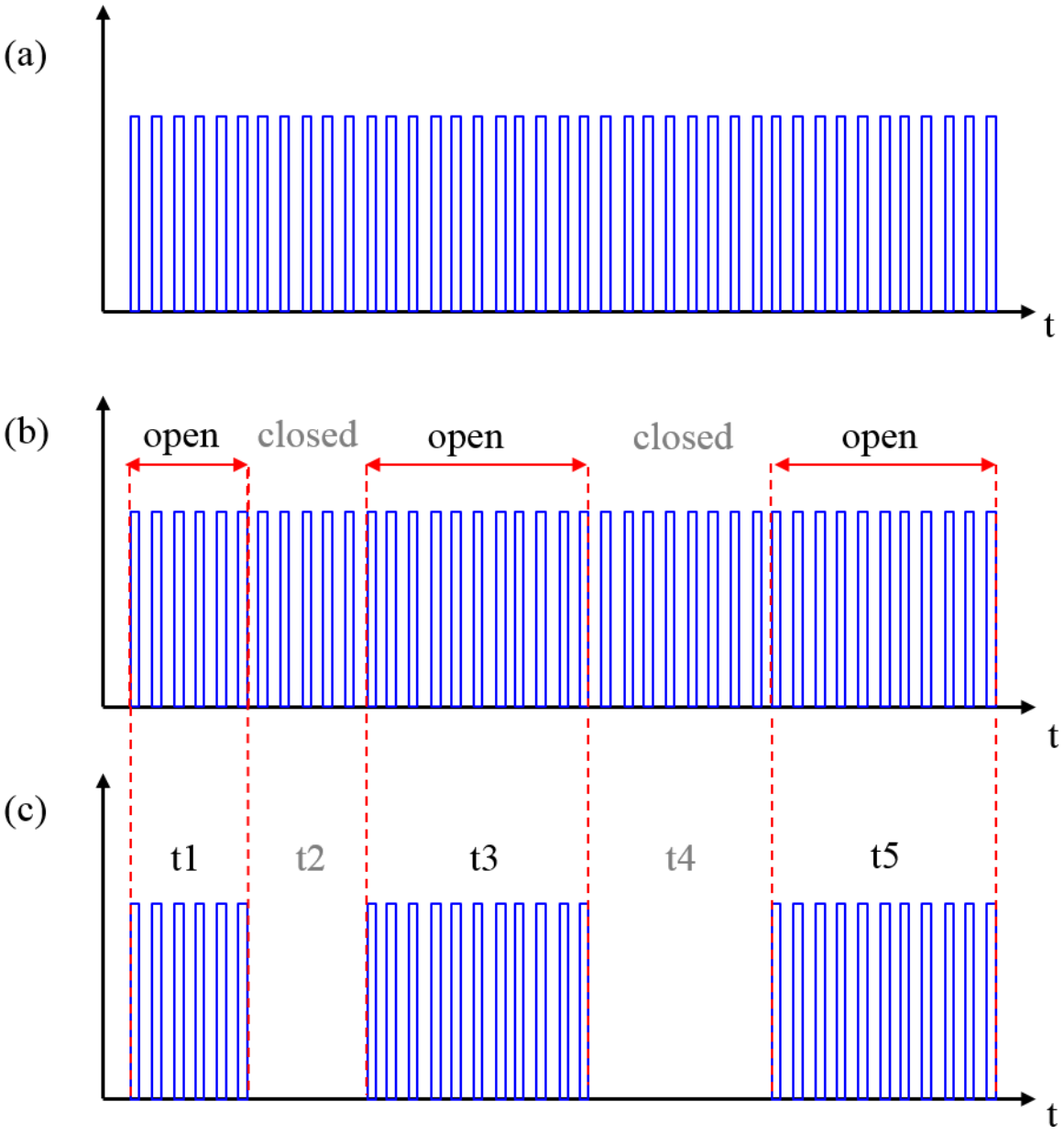

Figure 8. Mechanism of pulse control for the accurate deposition.

III. ELECTRODYNAMIC SIMULATION AS A DESIGN TOOL FOR OPTICAL COATINGS

3.1 Maxwell equations for FDTD

Any electromagnetic wave, such as a laser beam, is governed by the Maxwell equations:

$$\nabla \cdot (\varepsilon \mathbf{E}) = \rho_f \tag{5}$$

$$\nabla \cdot (\mu \mathbf{H}) = 0 \tag{6}$$

$$\nabla \times \mathbf{E} = -\frac{\partial(\mu \mathbf{H})}{\partial t} \tag{7}$$

$$\nabla \times \mathbf{H} = \frac{\partial(\varepsilon \mathbf{E})}{\partial t} + \mathbf{J} \tag{8}$$

Where ε and μ are permittivity and permeability of the medium; ρ_f and **J** are free charge density and current density; **E** and **H** are electric and magnetic field, respectively.

Maxwell's equations can be solved numerically with a finite-difference time-domain (FDTD) algorithm. All the electromagnetic characteristics such as wavelength, polarization, diffraction, all can be taken into account[31] with this method. The FDTD algorithm belongs to the general category of grid-based differential time-domain numerical techniques. It's based on the temporal and spatial terms of the required electric and magnetic field **E** and **H** on a staggered grid. By discretizing both the space and time partial derivatives of the partial differential formed time dependent Maxwell's equations, central-difference approximations can be obtained and the resulting finite-difference equations can be solved in a leapfrog manner. The electric field vector components and the magnetic vector components can be computed alternately till the desired transient or steady-state **E/M** field behavior is fully developed. The in-house Fortran programs are used for the electrodynamic simulations. In this proposal, FDTD algorithm is adopted for the electrodynamic simulations of the optical coatings deposited with PLD. In this section, we will only briefly introduce this technique and show ***an example of simulating laser keyhole absorptions*** with this algorithm[32].

3.2 An example of using FDTD for electrodynamic simulations

Laser keyhole welding has gained a lot of attentions in many areas of manufacturing due to its deep penetration capability, high precision, good quality of joints and small heat affected zone (HAZ) [33-36]. And the possibility and quality of the process strongly depend on the amount of energy absorbed from the laser. Raytracing is a technique often carried out for the calculation of the laser absorption but it only applies to simple geometries and many parameters, such as wavelength,

polarization, diffraction cannot be taken into account, resulting in less accurate results. On the other hand, Maxwell equations can be fully solved using FDTD algorithm and all the electromagnetic factors can be preserved. In this proposal, the laser energy absorption by a keyhole during the laser welding of uncoated/zinc-coated steel plates was studied using the FDTD algorithm and the wavelength enlargement method proposed by Deng and Ki [32, 37, 38]. Kim et al. recently measured the keyhole shapes during multi-mode fiber laser welding of zinc-coated and uncoated DP 590 steels by coaxially observing top and bottom surfaces of specimens [39], and their measured data were used for the simulations in this section. In their study, they simplified and constructed the keyhole shape by joining top and bottom keyhole apertures linearly, which the data were obtained through a semi-statistical frame analysis, therefore their constructed keyhole shapes were time-averaged. Electrodynamic simulations were conducted with identical experimental conditions, such as laser power, scanning speed, beam diameter, wavelength, and beam divergence angle. For the simulations, a circularly polarized continuous wave (CW) laser with a wavelength of 1070 nm and a focused beam size of 200 μm was employed as the energy source. Five different laser translation speeds along with four different laser powers were used as the processing parameters systematically. Some interesting results of the laser beam absorption characteristics are illustrated, which can only be obtained from full electrodynamic simulations, such as FDTD simulations[37].

A 2 kW multi-mode fiber laser (IPG YLS 2000) with a wavelength of 1070 nm was utilized. The beam was focused at the specimen top surface by a focusing lens with a focal length of 160 mm, and the focused beam has a top-hat intensity profile with a beam diameter of 200 μm. Two sheets of 1 mm thick DP 590 dual phase steel specimens were stacked without a gap in between, and both uncoated and zinc-coated steels were experimented. For each steel, a total of 20 experiments were conducted using four laser powers (1830, 1603, 1403, 1230 W) and five scanning speeds (21.2, 18.6, 16.3, 14.3, 12.5 mm/s). Here, the laser powers and scanning speeds were chosen systematically: laser power from 1230 to 1830 W and beam scanning speed from 12.5 to 21.2 mm/s were respectively divided into 4 and 5 equally spaced points on a logarithmic scale. Both top and bottom surfaces were separately shielded by argon gas with a flow rate of 25 l/min. **Figure 9** shows average keyhole shapes over a wide range of process parameters that were semi-statistically obtained from a coaxial observation method [39]. These keyholes were statistically averaged out of their fluctuating motions, so the beam absorption characteristics predicted by the simulation must be interpreted accordingly.

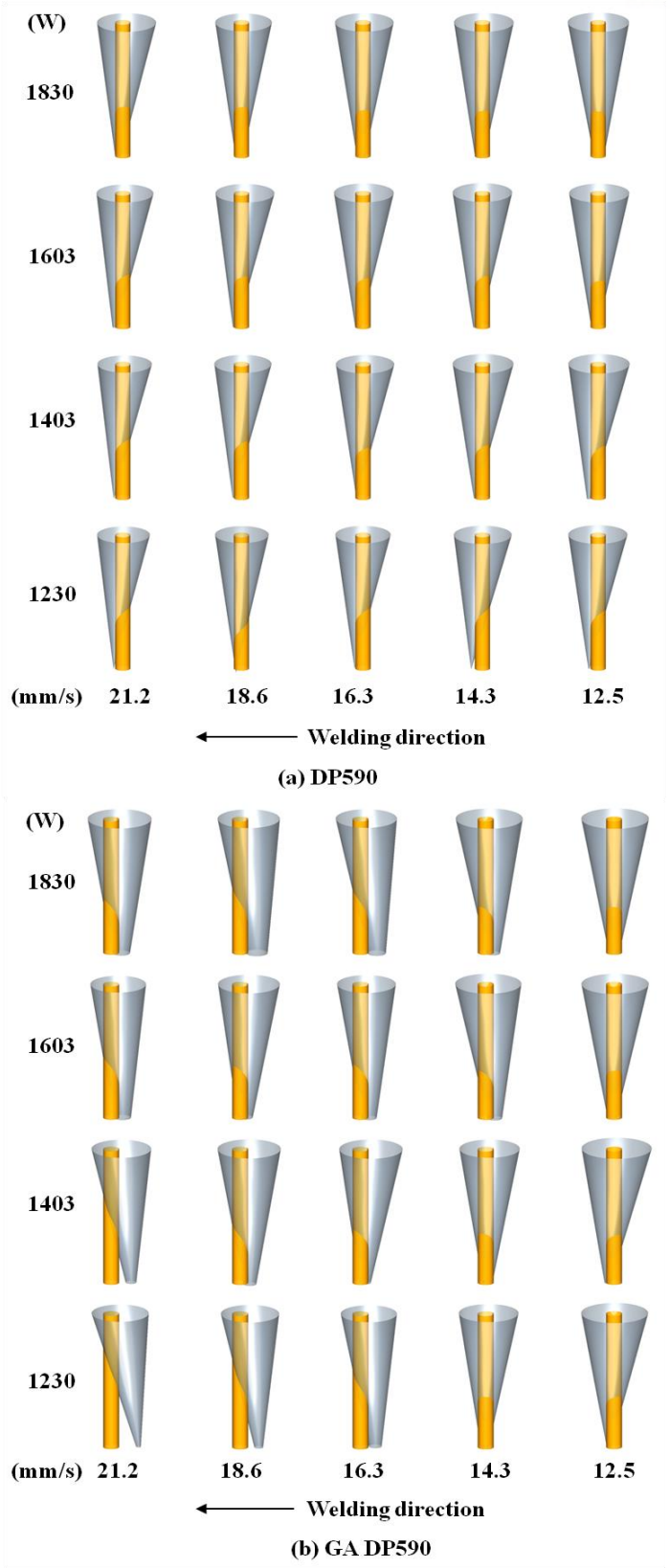

Figure 9. Re-constructed keyhole shapes for DP590 and GA DP590 based on measured data

In this study, each of the 40 cases in Figure **9** was simulated on a computational domain schematically illustrated in Figure **10**. Here, the black lines denote the computational domain while the red ones show a 2mm thick specimen with a formed keyhole. An absorbing boundary condition (ABC) must be employed to terminate the computational domain and absorb the outward traveling electromagnetic waves, so the convolutional perfectly matched layers (CPML) absorbing boundary condition was adopted in this study [40].

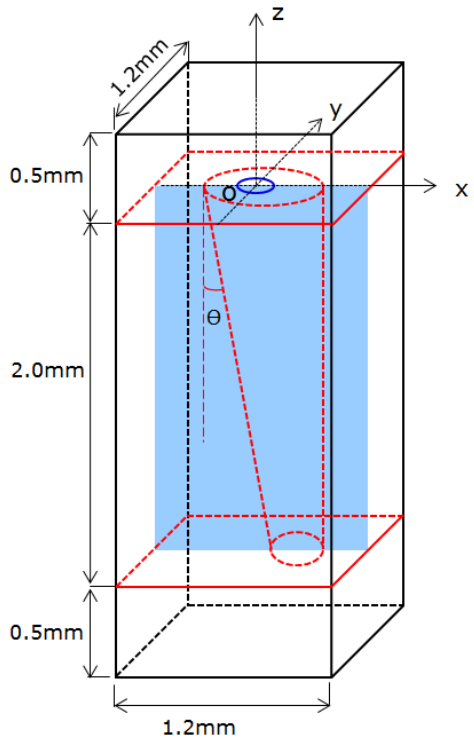

Figure 10.Schematic diagram of the computational domain with a keyhole. A laser beam is incident from the top and travels along the negative z direction. A focused beam is shown as a blue circle.

For the boundary condition for the laser beam, a Gaussian intensity profile was assumed. Note that the actual beam profile of the multi-mode fiber laser is top-hat when focused, and moving away from the focal plane, it changes to a Gaussian profile. However, it is mathematically very difficult to obtain a boundary condition for the electromagnetic field that not only yields such a beam profile but also satisfies the Maxwell equations. Therefore, in this study, a continuous-wave (CW) Gaussian beam with a wavelength of 1070 nm and a focused diameter of 200μm was used instead. It was implemented in the FDTD code in terms of the electric field and magnetic field using the paraxial beam theory as follows [41]:

$$E_{x,y}(x,y,z') = E_0 \frac{w_0}{w(z')} e^{-\frac{x^2+y^2}{w(z')^2}} \cos\left[\omega t - kz' - k\frac{x^2+y^2}{2R(z')}\right] \quad (9)$$

$$H_{x,y}(x,y,z') = H_0 \frac{w_0}{w(z')} e^{-\frac{x^2+y^2}{w(z')^2}} \cos\left[\omega t - kz' - k\frac{x^2+y^2}{2R(z')}\right] \tag{10}$$

Where ω is the laser beam angular frequency; E_0 and H_0 are the electric field and magnetic field at the beam center on the focal plane; w_0 is the beam waist; z' is the coordinate that is measured vertically from the beam waist; $w(z')$ is the beam radius at z'; $k = 2\pi/\lambda$ is the wave number (λ is the wavelength), and $R(z')$ is the radius of curvature of the beam's wavefront at z', respectively.

Different combinations of electric and magnetic field components can be used to describe different polarizations. The fiber laser used in the study has a random polarization. To closely emulate the polarization characteristic, circular polarization was assumed, so harmonically time-varying electric and magnetic field components in both x- and y-directions were assigned at the boundary plane. Also, the parameters in Eqs (9) and (10) were assigned such that the beam is focused at the specimen top surface.

One notable thing here is that the algorithm used in this study requires the increasing of the wavelength, which will inevitably affect the beam divergence as follow [41]:

$$\theta = \frac{\lambda^*}{\pi w_0} \tag{11}$$

Where θ is half the divergence angle, λ^* is the new wavelength. When the wavelength is increased, the divergence angle also increases, which is undesirable because it could change the reflection characteristics significantly, i.e., the locations where the laser beam irradiates on the keyhole surface will be changed. However, here we also notice that the fiber laser is a multi-mode laser and its beam parameter product (BPP) value is large (BPP=7.5 mm·mrad in this case), which makes the actual laser beam also diverge very fast compared with an ideal Gaussian beam. Therefore, in calculating an enlarged wavelength for simulation, we chose an enlarged wavelength such that the Gaussian beam with an enlarged wavelength has the same BPP value as the multi-mode fiber laser used for the experiment. Since the BPP value of the Gaussian beam is λ^*/π [41], the new enlarged wavelength can be determined from the following equation:

$$\mathrm{BPP} = w_0\theta = \frac{\lambda^*}{\pi} = 7.5\ \mathrm{mm}\cdot\mathrm{mrad}, \tag{12}$$

From which an enlarged wavelength of 23.54 μm is obtained. Therefore, if this wavelength is used, the divergence angle will be exactly same as that of the original laser beam. Also, because this value is

22 times larger than the original beam wavelength of 1070 nm, in three dimensions, the grid requirement will be reduced by 10648 times (22^3=10648).

For FDTD simulations, the refractive index n and extinction coefficient κ of the steel needs to be obtained. In this study, both steels were assumed as pure iron (Fe), and n and κ values for iron at 1070 nm were used (n = 3.240, κ = 4.338) [42]. Note that zinc has a boiling temperature of 907°C that is much lower than the melting temperature of iron (1538°C) so the effect of the zinc coating on Fresnel absorption is believed to be negligible. Using the wavelength enlargement algorithm [37], new simulation parameters were calculated and listed in Table 1, where, n, κ, ε_∞, ω_p and γ_p are the refractive index, extinction coefficient, dielectric constant at infinite frequency, plasma frequency and damping constant that were calculated to give exactly the same angle-dependent reflection characteristic of iron with the enlarged wavelength.

Table 1. Parameters used for FDTD simulations with an enlarged wavelength of 23.54 μm (1070×22 nm) for 1070 nm laser interaction with iron.

λ (μm)	**n**	**κ**	**ε_∞**	**ω_p (rad/s)**	**γ_p (rad/s)**
23.54μm	3.240	4.338	2.0	7.464×1014	2.1816×1014

Note that the temperature dependence of optical properties was neglected in this study. Apparently, the laser beam interacts with the liquid phase of steels at elevated temperatures, but optical properties of liquid metals are rarely available. Also, we neglected the laser beam absorption by keyhole plasmas (known as the inverse bremsstrahlung process [43]) and focused solely on the Fresnel absorption process. Note that, for a wavelength of 1070 nm, it is generally regarded that plasma absorption in a keyhole is not significant.

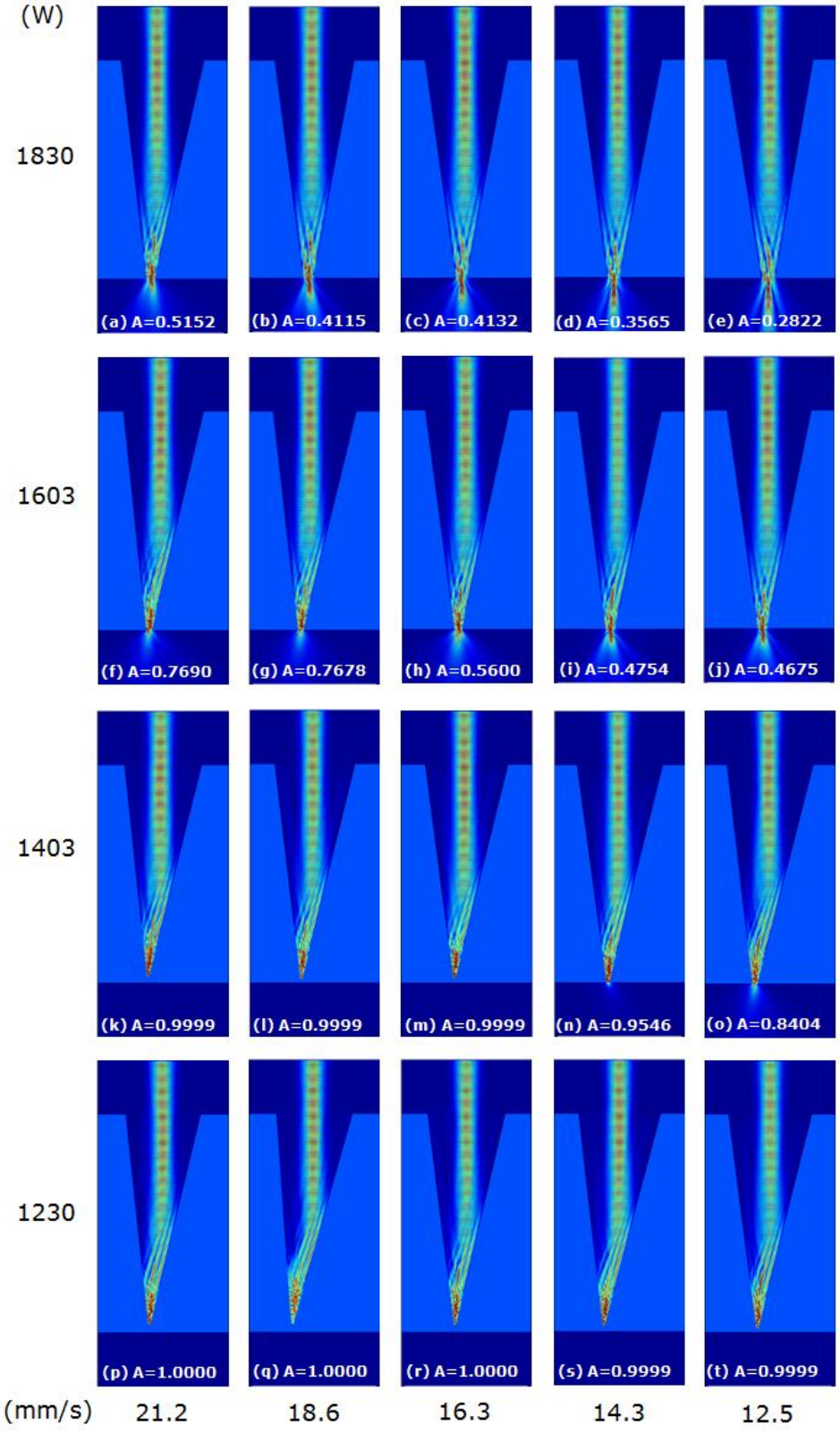

Figure 11. 1070 nm laser interaction with DP590 steel specimens (uncoated). Each plot shows the electric field propagation inside a keyhole

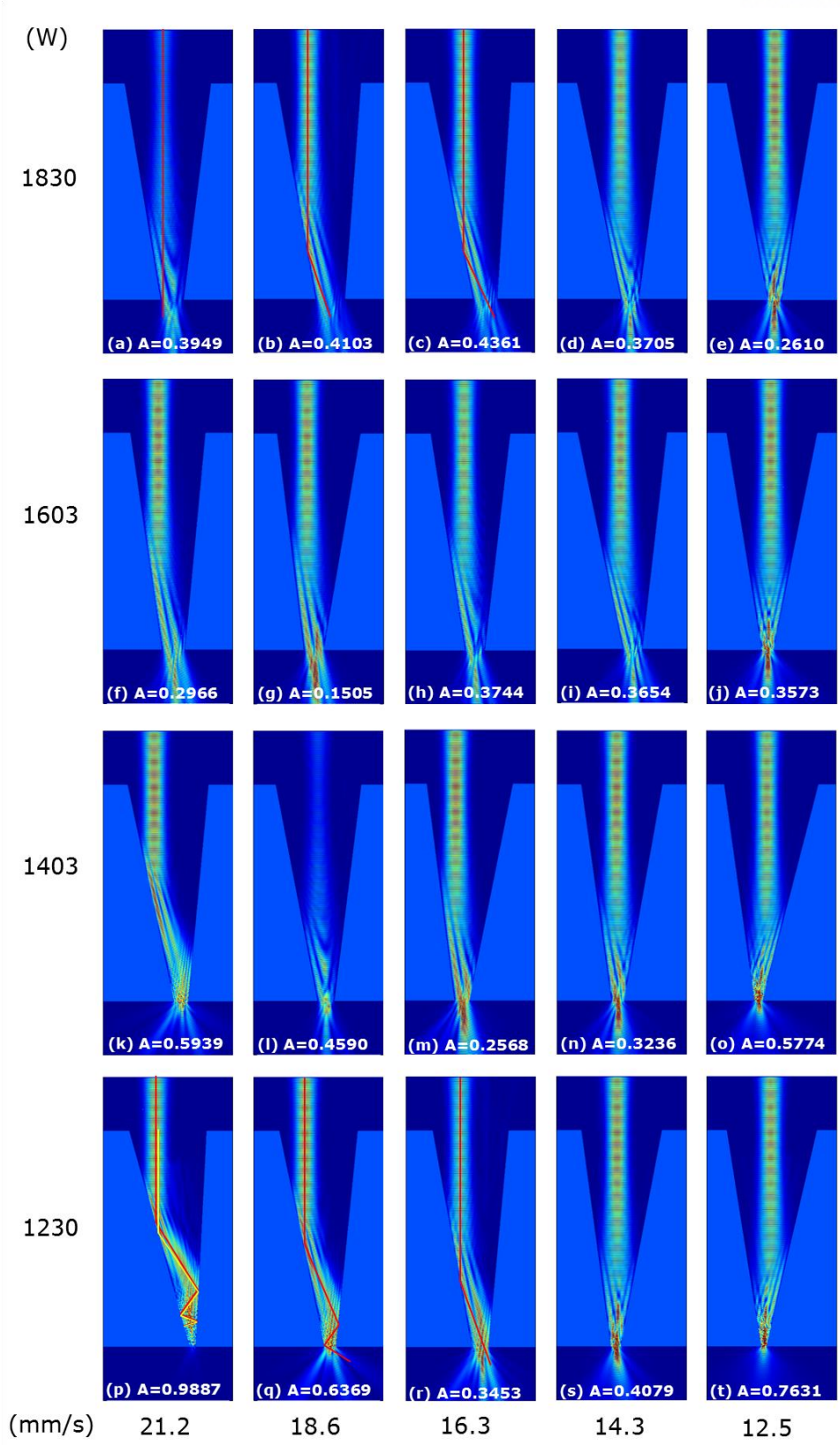

Figure 12. 1070 nm laser interaction with GA DP590 steel specimens (zinc-coated). Each plot shows the electric field propagation inside a keyhole.

In **Figure 11** and **Figure 12** the overall laser beam interaction patterns with the keyholes for uncoated and zinc-coated steels are presented. The figures are arranged in terms of laser power and scanning speed systematically. Simulations were conducted in a three-dimensional domain, though each figure only shows the electric field components on a plane that passes through the centers of the top and bottom keyhole apertures. We assumed the top and bottom apertures to be circular for simplicity, therefore, the keyhole is symmetric about this image plane. As illustrated, a laser beam is irradiated from the top and is incident into the keyhole vertically and undergoes reflections and interferences. The laser beam is numerically focused at the top surface of the keyhole and propagates downwards. In some cases, some laser beams look dimmer than others (especially, Figure **12a** and **l**) because they are located a bit away from the symmetry plan of the keyhole. Note that these keyhole data were obtained experimentally, so there were apparently some measurement errors and the laser beam cannot be perfectly aligned with a keyhole, either.

From Figure **11** and Figure **12**, several big differences can be noticed regarding the beam interaction patterns for uncoated and zinc-coated steels. For the zinc-coated steel, the laser beam is incident on the front keyhole wall while the beam is incident near the bottom keyhole aperture for the uncoated steel. As reported by Kim et al. [39], in laser welding of uncoated DP 590 steel, the keyhole internal pressure is relatively low and the amount of keyhole bottom opening is minimal. Notice that the laser beam energy is highly concentrated when the bottom aperture is small. In this case, concentrated heating will take place, which will force the bottom aperture to open again. Therefore, the opening and closing of the keyhole is controlled by the direct laser heating of the keyhole bottom area, and we believe that this is the mechanism of the opening and closing of the bottom keyhole aperture. This intense heating of the bottom area is shown clearly in Figure **11** (and also some cases in Figure **12**). On the other hand, the keyhole internal pressure is higher due to zinc evaporation for the zinc-coated steel, and the keyhole bottom aperture opens much wider and more consistently. Because of this high keyhole pressure, laser-keyhole interaction occurs on the front keyhole wall surface because otherwise the beam will just pass through the bottom aperture [39].

Because of this configurational difference, multiple reflections phenomena occur more conspicuously for zinc-coated steel. Note that a relatively low power (2 kW) laser was used for the experiment and this result may not be generalized for higher power laser welding. However, at least it can be said that at the same laser power and scanning speed the zinc-coated steel has more favorable configurations for multiple reflections.

In this study, the absorptance of a keyhole (A) was calculated using the Poynting vector as follows:

$$A = \frac{\int \left|\mathbf{n}\cdot(\mathbf{E}\times\mathbf{H})\right| dA_{top} - \int \left|\mathbf{n}\cdot(\mathbf{E}\times\mathbf{H})\right| dA_{bottom}}{\int \left|\mathbf{n}\cdot(\mathbf{E}\times\mathbf{H})\right| dA_{\text{incident}}} \quad (13)$$

Where n is the normal vector to the top and bottom (horizontal) surfaces of a specimen and the integrals in the numerator and denominator are calculated over the keyhole bottom and top apertures, respectively. Calculated laser absorptance for each case is also shown in **Figure 11** and **Figure 12**. As a comparison and validation, a traditional method of raytracing is also conducted on the same keyholes. Raytracing is method of simulating light beams by dividing them into a large number of rays based on the principles of geometry optics. For raytracing, the angle dependent absorption by the keyhole is taken into account by the refraction index and extinction number of Fe where its refraction index n=3.24 while extinction number κ=4.34; and the divergence angle of the beam is dealt with the method reported by Sohail et al[44]. Some ray tracing results are shown in Figure **13** as an example along with the correlation with FDTD simulation results, it shows that the ray tracing results are qualitatively similar to the corresponding FDTD results, therefore validating the results of FDTD. The incident and reflected rays are shown in red and back-reflected rays (ray tracing case) are shown in yellow.

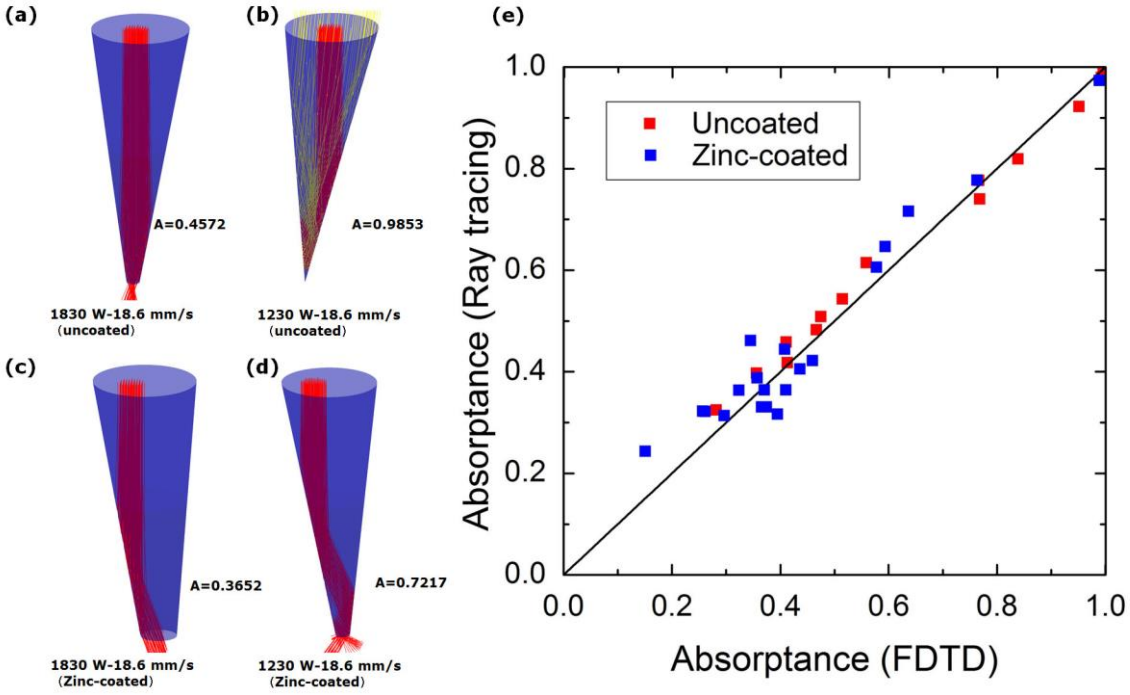

Figure 13.Ray tracing simulation examples for Zinc-coated and uncoated DP 590 with same process parameters. (e) shows the correlation between FDTD and ray tracing.

Apart from the direct electrical field plotting, the laser intensity distribution patterns on keyhole surfaces are also available with a FDTD simulation. The intensity patterns are shown for both uncoated

and zinc-coated steels in **Figure 14**. The intensity distribution patterns resemble the beam interaction patterns given in Figure **11** and Figure **12**, and therefore, the intensity distribution patterns for uncoated and zinc-coated steels are remarkably different. For the uncoated steel (DP 590), the heating occurs near the bottom aperture area, and the rear part of the keyhole is shown to be heated because of the forward bottom aperture movements. As the laser power decreases, the heating area increases in order to compensate for the decrease in energy. For the zinc-coated steel, the front keyhole walls are heated, and overall the heating area increases as the energy density decreases.

Note that an intensity distribution is very similar to the actual Joule heating pattern, so these plots can be interpreted as laser heating patterns with cautions. It contributes to the better understanding of the complex laser absorption process during laser keyhole welding.

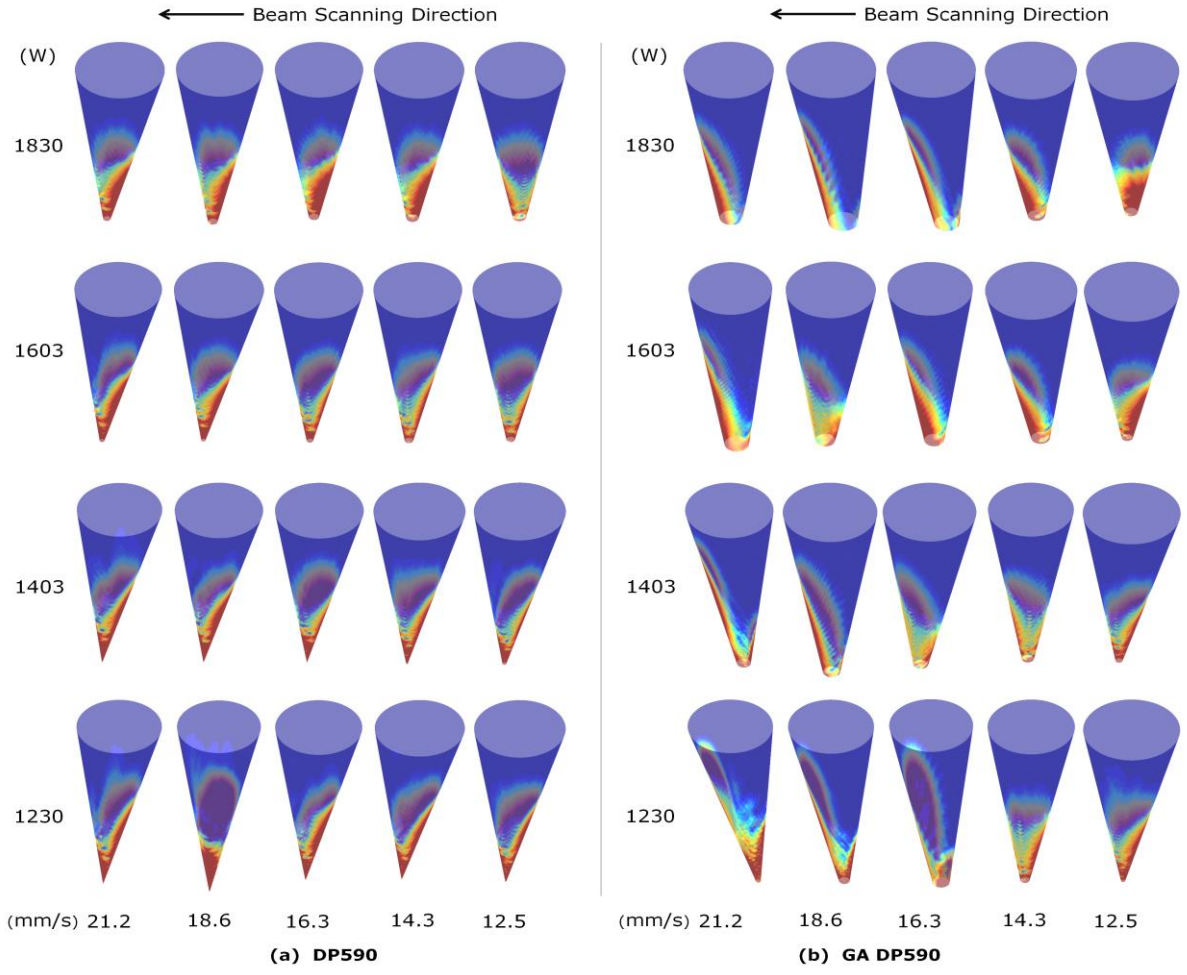

Figure 14. Intensity distribution patterns on keyhole surfaces for DP 590 (uncoated) and GA DP 590 (zinc-coated) steels.

Figure 15 presents contour plots of keyhole absorptance for uncoated and zinc-coated steels on laser intensity (I_0)-interaction time (t_i) coordinates, and the corresponding laser power and scanning speed values are shown separately. Here, the interaction time is defined as the beam diameter divided by the scanning speed. For the uncoated steel (**Figure 15a**), the absorptance decreases monotonically along the diagonal direction (toward the top-right corner), and the trend is fairly clear. Note that along the direction, energy density increases. For the zinc-coated steel, on the other hand, the absorptance decreases rather rapidly to around 0.4 and then shows an irregular pattern. We believe that this difference is another indication of more unstable keyhole motion due to zinc evaporation. In both cases, the keyhole seems to automatically decrease the amount of energy absorption as the energy density of the incident laser increases.

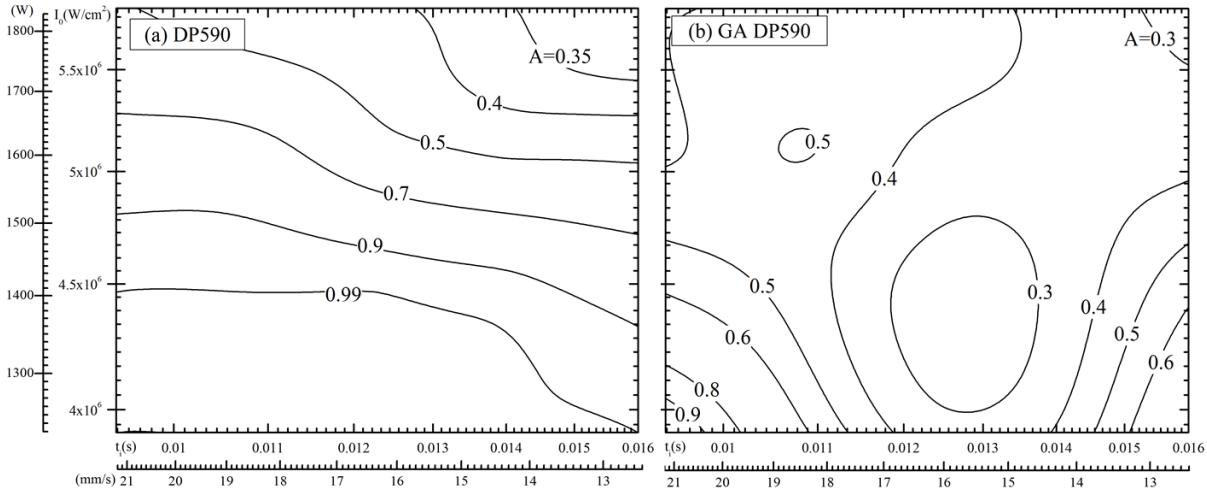

Figure 15.Contour plots of keyhole absorptance on intensity-interaction time coordinates for DP 590 (uncoated) and GA DP 590 (zinc-coated) steels

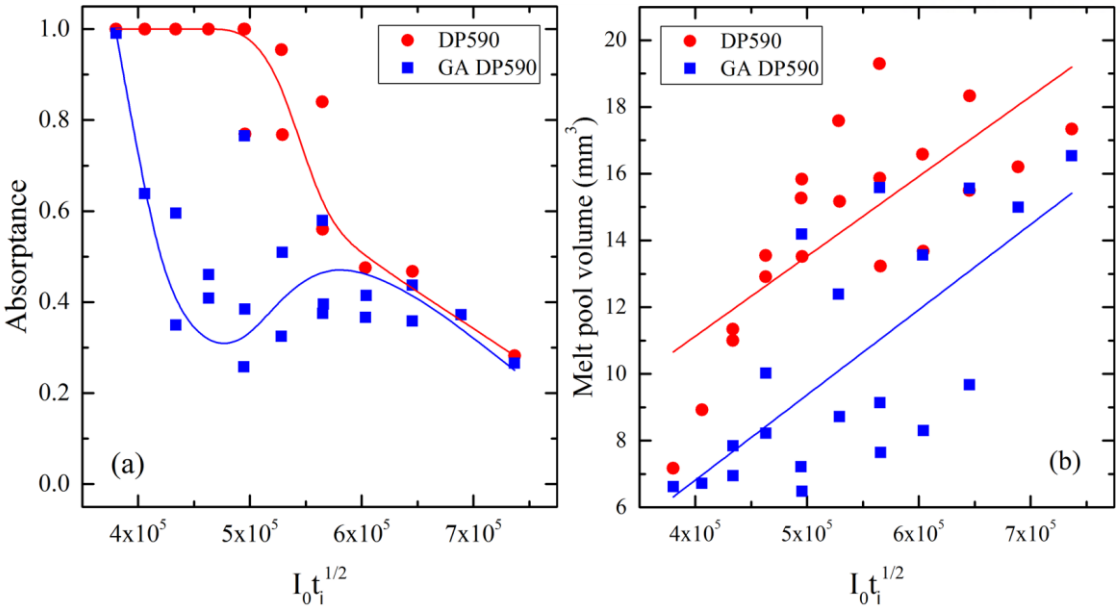

Figure 16. Keyhole absorptance and melt pool volume vs. $I_0t_i1/2$ for DP 590 (uncoated) and GA DP 590 (zinc-coated) steels

Figure **16** shows the keyhole absorptance and the melt pool volume versus $I_ot^{1/2}$. Note that $I_ot^{1/2}$ is a parameter that is proportional to the surface temperature during laser heating [45], so the x-axis can be interpreted as the degree of laser heating because a higher temperature means a more intense laser heating. In this study, the melt pool volume was calculated as $1/2(A_T + A_B)t$, where A_T and A_B are melt pool areas measured at the top and bottom specimen surfaces, and t is the specimen thickness. Both top and bottom melt pool areas were measured three times using three different melt pool images, and an average was calculated.

For the uncoated steel, the keyhole absorptance decreases as the degree of laser heating increases. Up to about $I_ot^{1/2} = \sim 5\times10^5$, the absorptance is ~100%, indicating that the entire laser energy is absorbed. As the laser heating is furthered beyond this point, less and less amount of energy is absorbed as the excess energy is lost through the keyhole bottom aperture. The trend is clearly shown. For the zinc-coated steel, up to about $I_ot^{1/2} = \sim 5.3\times10^5$, the keyhole absorptance decreases sharply from 0.9910 to ~0.2, and then jumps a little bit to follow the trend of the uncoated steel. The overall pattern is more irregular in this case, which we believe is due to more volatile keyhole movements for the zinc-coated steel.

One last important thing to note in **Figure 16** is that overall (especially at low values of $I_ot^{1/2}$) the absorptance is significantly lower for the zinc-coated steel, which we believe is caused by larger bottom apertures in the laser welding of zinc-coated steel. This lower absorptance for the zinc-coated steel can be justified by the experimental data in **Figure 16b**. As shown in this figure, although the melt pool

volume for the two steels increases as the degree of laser heating increases, it is almost consistently smaller for the zinc-coated steel. Considering that the melt pool volume is proportional to the keyhole absorptance at the same laser heating condition, the simulation result on the smaller keyhole absorptance for the zinc-coated steel can be justified.

3.3 Conclusions

In this section, we discussed the electrodynamic simulation algorithm FDTD and illustrated an example of using FDTD for the simulation of calculating the laser absorption of keyholes during laser welding. It shows that FDTD is a very powerful tool for electrodynamic simulations. The simulation will mainly be used as a design tool and validation method for the optical graded coatings.

The major findings of this study are summarized as follows:

The FDTD method with the enlarged wavelength scheme was effectively used for keyhole absorption problems. In this study, the keyhole shapes that were measured experimentally were used for simulation, and the beam divergence, polarization and focusing characteristics of the laser were matched. In this way, all the electromagnetic characteristics of the problem were naturally accounted for.

Multiple reflections phenomena occur more conspicuously for the zinc-coated steel. As the energy density decreases, the number of reflections also increases in order to absorb an enough amount of laser energy to sustain a keyhole.

For the uncoated steel, the keyhole absorptance is controlled by the keyhole bottom aperture size.

When the bottom aperture is small, laser energy is highly concentrated around there. In this case, concentrated heating will take place, and the bottom aperture will be forced to open again. This is believed to be the mechanism of the opening and closing of the bottom keyhole aperture.

For uncoated steel, the keyhole absorptance decreases as $I_o t^{1/2}$ increases, and the pattern is very regular. For zinc-coated steel, the keyhole absorptance decreases sharply first, and then increases somewhat to follow the trend of the uncoated steel. The overall pattern is more irregular.

Zinc-coated steel has a much lower keyhole absorptance than uncoated steel at the same experimental condition, which was experimentally validated by melt pool size measurement.

IV. BROADBAND ANTIREFLECTION COATING FOR SILICON-BASED SOLAR CELLS

4.1 Introduction of AR coatings

Reflections will inevitably take place when light propagates across an interface between two materials with different refractive index values. In many applications, such as in photovoltaics, however, efficient light harvesting is very important[46], therefore the use of an antireflection (AR) coating is for the applications is highly desirable. With an AR coating, the amount of light reflection can be considerably reduced, which improves the device performance[47, 48]. For many years, the reduction of light reflection from the solar cell surface has always been one of the primary focuses of solar cell research[49], and a variety of low refractive index materials and fabrication methods have been developed to build high performance AR coatings. In this section, we will discuss the design, fabrication and characterization of the PLD of antireflection coatings for silicon-based solar cells. In this study, we chose silicon and soda-lime glass as the parent materials for the deposition. In this section, broadband graded index antireflection films for silicon based solar cells will be introduced.

4.2 Design of the graded AR coating

In **Figure 17** we demonstrate the scheme of the fabrication process of a functionally graded AR coating. A laser beam is split into two and each beam is irradiated on one target material for generating plasmas for the depositions. Each beam is also motorized by an attenuator for the pulse control of an accurate graded coating composition. In **Figure 17b** and **c**, we showed the structure differences between a solar cell with a standard AR coating and a solar cell with our graded index AR coating. With our design of the AR coating, it can serve as a protective cover glass for silicon-based solar cells due to the 100% glass content as the outer surface of the coating. In this way, an AR coating and a protective glass can be deposited in a single PLD procedure and can be completely integrated into a single unit on a silicon-based solar cell. It can simplify the standard silicon-based solar-cell structure considerably.

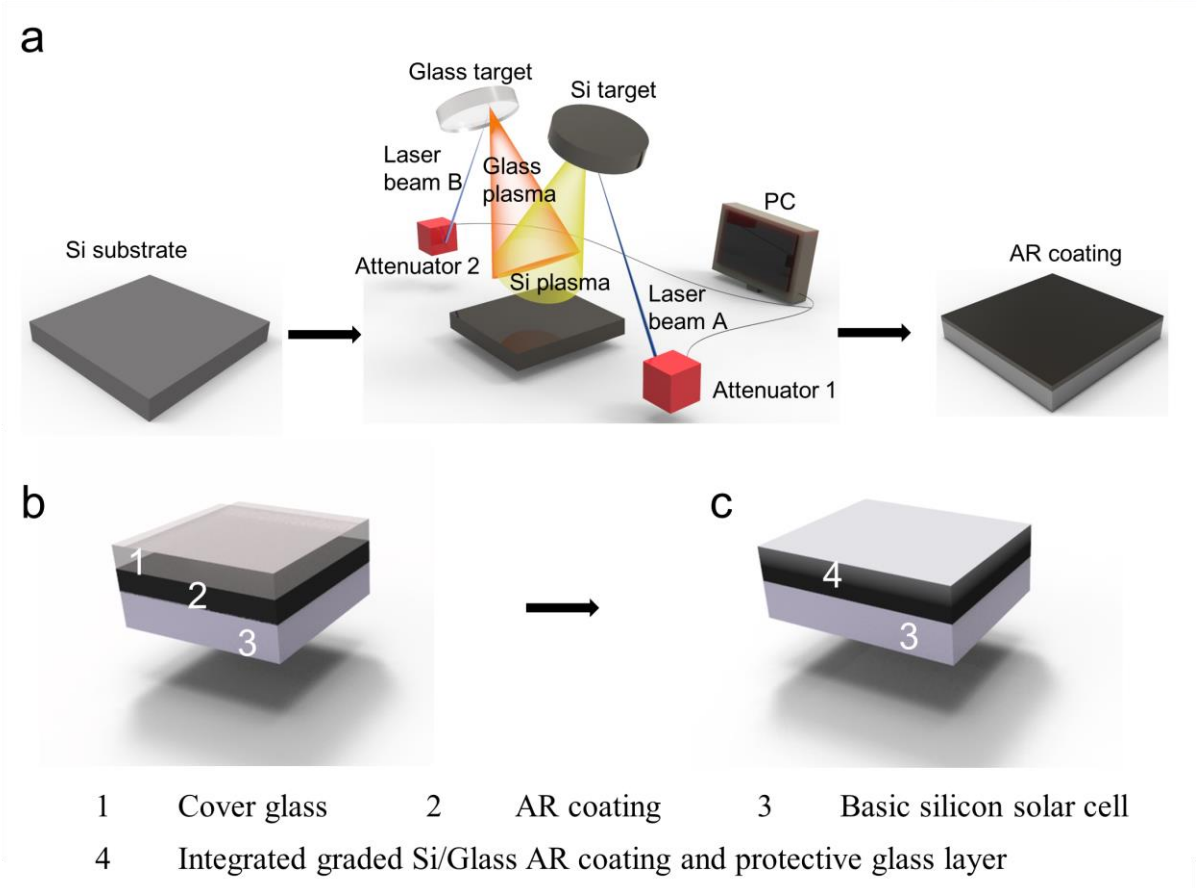

Figure 17. Fabrication of a Si/glass graded AR coating by the dual-beam pulsed laser deposition. (a) Schematic drawing of the overall experimental procedure for fabricating a Si/glass graded AR coating. (b) A generic silicon-based solar cell structure. (c) Simplified silicon-based solar cell structure using the present graded AR coating.

A graded antireflection coating with a graded refractive index can be realized by varying the composition of two optical materials along the coating growth direction. In order to design an index gradient profile, the refractive index of material mixture needs to be calculated as a function of mixture composition. Several mixture rules for refractive index are available in the literature[50], and in this study, the volume fraction method[42, 50] was adopted, which is described as:

$$n_{\text{mix}} = \phi_1 n_1 + \phi_2 n_2 \tag{14}$$

Where n_1, n_2 and n_{mix} are the refractive indices of material 1, material 2, and their mixture, respectively; ϕ_1 and ϕ_2 are the volume fractions of material 1 and material 2.

In this study, silicon and soda-lime glass were chosen as the two parent optical materials, and a 1 μm thick AR coating was designed on top of a silicon substrate. The composition changes from 100%

silicon at the substrate surface to 100% glass at the coating outer surface gradually, and two different refractive index profiles were considered, Southwell and linear profiles, which are mathematically expressed as

$$n_{Southwell}(x) = n_{Si} - (n_{Si} - n_{glass})\left[10\times\left(\frac{x}{1.0}\right)^3 - 15\times\left(\frac{x}{1.0}\right)^4 + 16\times\left(\frac{x}{1.0}\right)^5\right] \quad (15)$$

$$n_{linear}(x) = n_{glass}x + n_{Si}(1-x) \quad (16)$$

Where x is the coordinate measured from the substrate surface to the given location inside the AR coating and $0 \le x \le 1\,\mu\text{m}$.

Before the design and fabrication process of the graded AR coating, new refractive indices of deposited Si and soda-lime glass are investigated since the refractive index values for deposited material and original materials might be different. Two raw materials are deposited into pure thin coatings and their reflectance values are measured. The new refractive index can be calculated using Essential Macleod 7.1 software. **Figure 18** showed the refractive indices of deposited silicon and glass and the corresponding graded coating profiles. It turns out that index values for deposited Si and glass were quite stable for the whole spectral range, and the measured refractive index values of n_{Si}=1.8 and n_{glass}=1.5 will be used to design our AR coatings. The 355nm picosecond laser is used for the deposition.

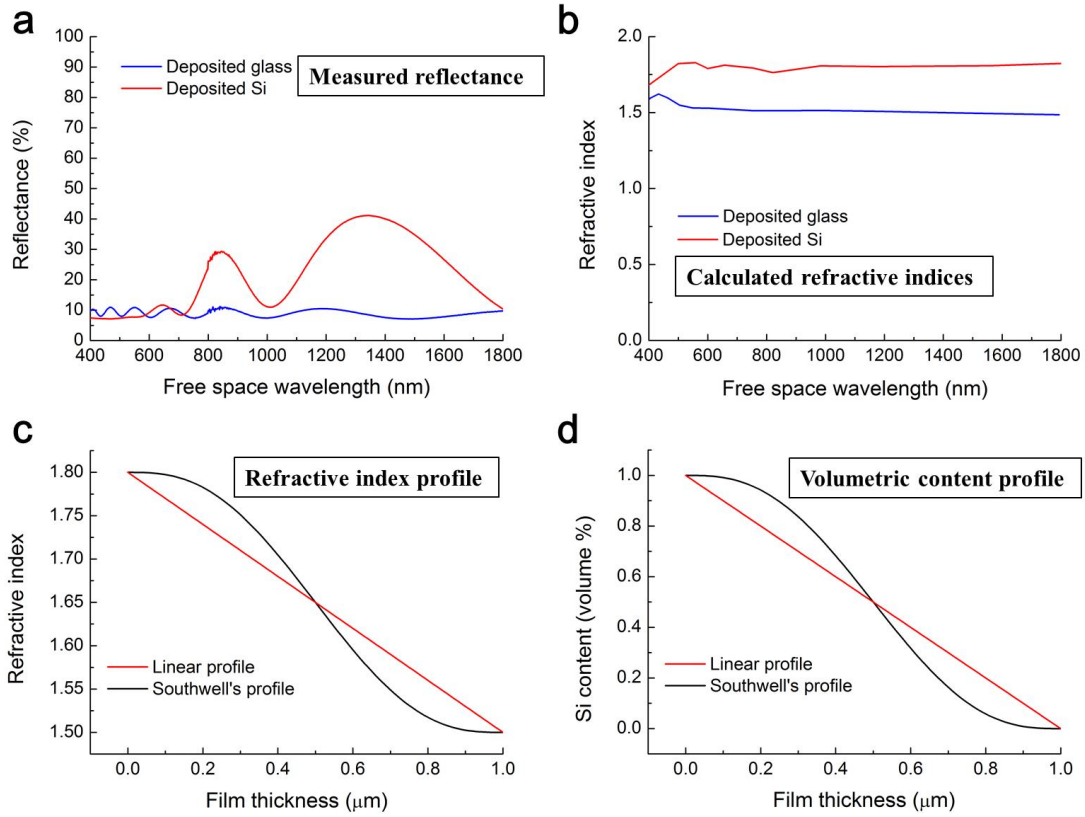

Figure 18. Refractive indices of deposited silicon and glass and the corresponding graded coating profiles. (a) Measured reflectance of the deposited silicon and glass films. (b) Calculated refractive indices of deposited silicon and glass using the commercial software Essential Macleod 7.1. (c) Graded index profiles (Linear and Southwell) based on the measured refractive indices. (d) Silicon volumetric content profiles corresponding to the refractive index profiles in (c).

In **Figure 18**, the refractive index of deposited glass has almost the same refractive index as the original glass while the deposited silicon has only about a half of the refractive index of silicon (~3.5), and this is probably due to the fact that deposited materials are less condense and more porous structures inside the materials are realized. Graded index profiles of two types and the corresponding silicon volumetric content profiles are presented in **Figure 18**c and **d**, respectively.

4.3 Fabrication of the graded AR coating

In order to build an AR coating with a designed content profile, the deposition rate of each material should be known precisely. Figure **19a** and b present the deposition data of soda-lime glass (obtained with a laser power of 2.8 W) and silicon (obtained with a laser power of 3.0 W), respectively, where the coating thickness versus deposition time is shown up to 20 minutes. The silicon coating thickness was

measured at a time interval of 2 min while the glass coating thickness was measured at 2, 4, 6, 8, 10, 15 and 20 minutes. Each deposition curve was then fitted to the Nelder model[29],

$$\theta(P,\ t)=\frac{t}{b_0+b_1t+b_2t^2} \tag{17}$$

Where θ is the coating thickness (given as a function of laser power P and deposition time t), and b_0, b_1, b_2 are fitting coefficients. The fitted lines are shown as blue (glass) and red (silicon) solid lines in **Figure 19a** and **b**.

With the obtained deposition data for silicon and glass, now AR coatings can be easily fabricated. To deposit a graded coating (1μm thick), we first divided the coating into equally spaced 30 layers and for each layer the amounts of silicon and glass were calculated based on the given profile as discussed in the previous sections with pulse control technique. **Figure 19c** and **e** show the designed content profiles while d and f show the calculated laser power schemes with the pulse control method. Red lines stand for silicon and blue lines stand for glass. With these methods, graded AR coatings can be fabricated with predesigned content profiles. In **Figure 20a** and **b** show the deposited AR coatings without and with an additional 400nm thick pure glass layer, respectively, demonstrating drastic changes in reflection characteristics. In each of **Figure 20a** and **b**, linear and Southwell profiles are compared with a polished bare silicon sample. As shown clearly, bare silicon samples reflect light quite strongly as the word “UNIST” is clearly visible on the surface. On the other hand, for the two graded films, regardless of the existence of a glass layer, the surface is almost pitch black and reflection can be hardly observed.

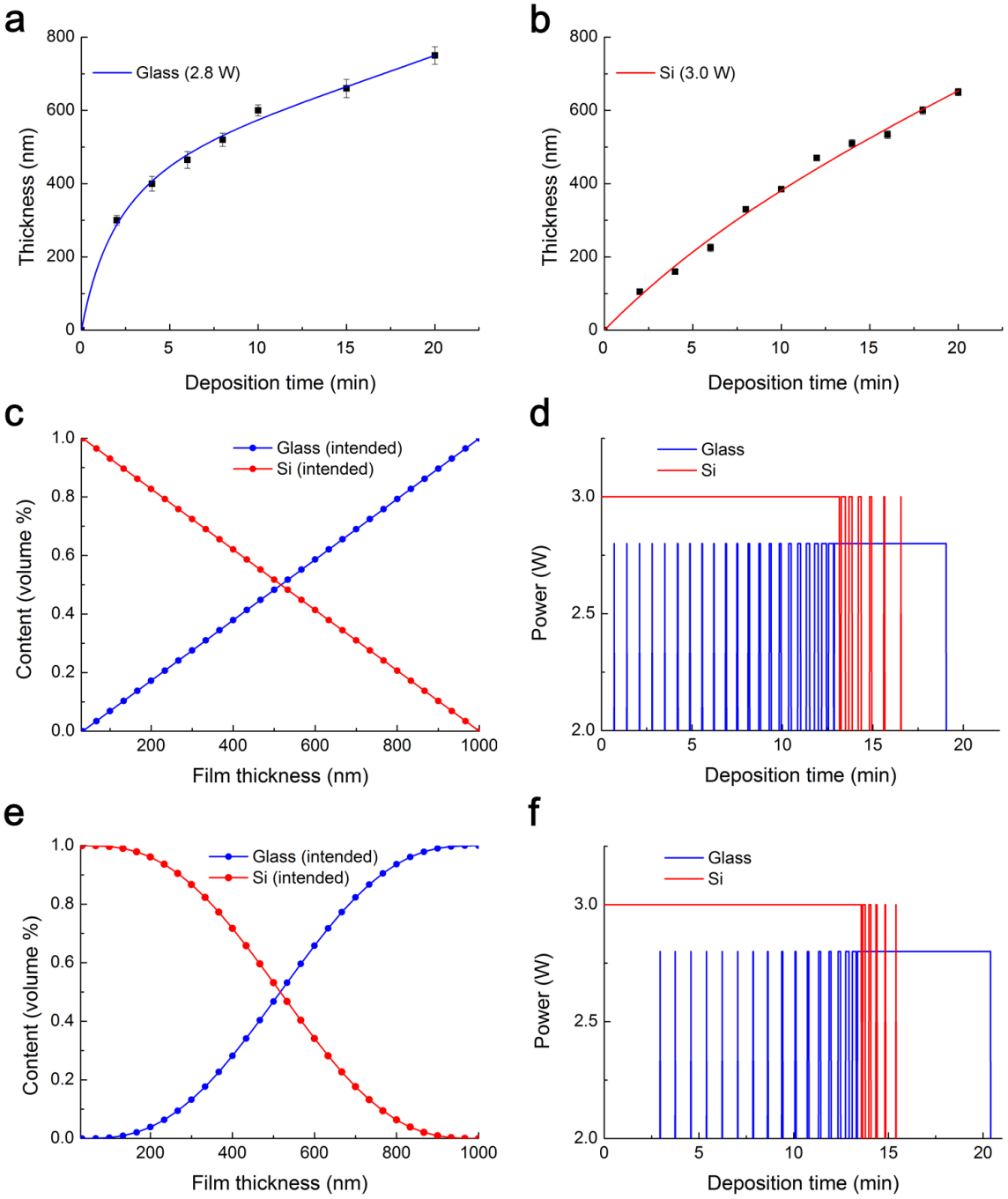

Figure 19. Dual-beam PLD of graded glass-silicon coatings. (a) Deposition rate data (black squares) of soda-lime glass corresponding to a laser power of 2.8 W. The blue line is the fitting line. (b) Deposition rate data (black squares) of silicon corresponding to a laser power of 2.8 W. The red line is the fitting line. (c) Designed silicon and glass volumetric content profiles for the linear profile. (d) Calculated power scheme corresponding to the linear profile shown in (c). (e) Designed silicon and glass volumetric content profiles for Southwell's profile. (f) Calculated power scheme corresponding to Southwell's profile.

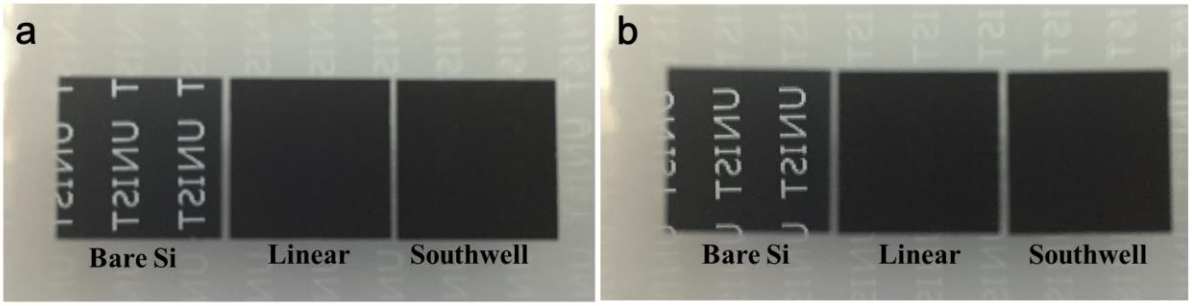

Figure 20. AR performance of the graded coatings. (a) Bare silicon wafer, linear profile without a glass layer and Southwell's profile without a glass layer (from left to right). (b) Bare silicon wafer, linear profile with a 400 nm glass layer and Southwell's profile with a 400 nm glass layer (from left to right). The wafer size is 15 mm × 15 mm.

4.4 Measured results

The coating thicknesses are measured with a surface profiler, and then all deposited coatings with bare silicon are measured with measured using a UV-VIS-NIR spectrophotometer (Agilent, Cary 5000) for the reflection values. Measured wavelength range was from 400 to 1800 nm and the data were obtained at a 2nm interval.

In order to validate the content profiles of the deposited AR films, the x-ray photoelectron spectroscopy (XPS, K-alpha spectrometer, Thermo Fisher) depth profiling method was employed and the measurement results for the linear and the Southwell profiles without a glass layer are presented in **Figure 21a** and **b**. As shown, measured profiles and intended profiles agree reasonably well. **Figure 21c** shows a measurement example for the linear profile, showing how the XPS peak evolves from the coating surface to the silicon substrate. Starting from the coating surface to inside, the Si (4+) peak decreases while the Si (2p3) peak increases, which indicates that, as expected, the SiO2 content decreases and the silicon content increases as we move inward. **Figure 21d** shows an XPS peak analysis conducted at one location inside the coating (the location shown with a green arrow in **Figure 21a** as an example. All possible valence states of Si (2p) peaks were added and fitted using XPSPEAK software, but no contents of Si (3+), Si (1+) and Si (2p1) were observed and only Si (4+), Si (2+) and Si (2p3) were found in the results.

All deposited samples were analyzed using the XPS depth profiling method for SiO2 (4+) and Si (2p3). The etching was conducted with 1 keV Argon ion energy. Etching area was 2 mm × 4 mm. SiO_2 is the major constituent of soda-lime glass, and the sputter etching rate ratio is reported [51] to be

$Si:SiO_2 = 1.04 \pm 0.10 \approx 1:1$. So, in **Figure 21a**, **b** and **Figure 22a**, **b**, the results were obtained at an etching rate of 1:1 for Si and SiO_2. The K-alpha spectrometer has aluminum Kα with a pass energy of 50 eV, a measuring spot size of 0.2 mm and an energy step size of 0.1 eV. The atomic ratio of Si (2p3) and Si (4+) can be calculated using the area ratio of each peak measured from XPS, and the peaks were fitted using the XPSPEAK software after the background was subtracted appropriately. A small amount of Si (2+) was also found in **Figure 21d**, and it is the side reaction product of the Si and SiO_2 at high temperatures: Si+SiO2→2SiO. Contributions to SiO from Si and SiO_2 are 50% and 50%, so when atomic ratio calculations of Si and SiO_2 were carried out, it was assumed that Si and SiO_2 equally contributed to SiO. In **Figure 21d**, the peak areas of SiO_2, SiO and Si are 15005, 1063 and 2687, respectively. Distributing a half of SiO to Si and the other half to SiO_2, the peak areas are now: 15537 for SiO_2 and 3219 for Si. Therefore, the atomic percentage of Si (2p3) can be calculated as 17.16%.

From the obtained atomic percentage values, now volumetric percentage values can be calculated considering the actual densities of the deposited silicon and glass. Since the deposited silicon has a refractive index of ~1.8 while the refractive index of bare silicon is ~ 3.5, from the mixture rule for refractive index now applied to silicon (n ~ 3.5) and air (n ~ 1), the volume of the deposited silicon can be considered to have expanded by roughly 3.1 times from the original silicon. On the other hand, the deposited glass volume was assumed to remain the same because the refractive indices of the original and the deposited glass are the same (both around 1.5). Note that because original silicon and SiO_2 have molar volumes of 12.17 cm^3 and 27.27 cm^3 [52], respectively, their volume ratio is $27.27:12.17 = 2.24:1$. Accounting for the silicon volume expansion, the volume ratio is $2.24:(1\times 2.8) = 2.24:3.1$. Soda lime glass has other constituents, such as Na_2O (14 wt.%) and CaO (9 wt.%), and their molar masses are 62 g and 100 g while their densities are 2.27 g/cm^3 and 3.35 g/cm^3, respectively. Their volume percentages in glass can be calculated to be ~14% and ~6% for Na_2O and CaO. Therefore, SiO_2 has a volume percentage of ~80% in glass. Combining the results together, we can calculate the volume ratio of deposited glass and silicon as $(27.27 \div 80\%):(12.17\times 3.1) \approx 1:1$, therefore the atomic percentages of Si (2p3) and Si (4+) can be used to directly represent the volumetric content percentages of the deposited materials. in **Figure 21a**, **b** and **Figure 22a**, **b**, all 4 volumetric content profiles were drawn based on these assumptions and calculations. XPS measured results agree well with the intended profiles, therefore our deposition method is correct.

Figure 21e and **f** show the measured spectral reflectance of linear and Southwell profiles without a glass layer. Reflectance was measured over a wavelength range from 400 to 1800 nm (visible to near

IR), and simulations were conducted for the same wavelength range at an interval of 200 nm. As clearly demonstrated, the reflectance is roughly 4% for the linear profile and between 2.2~5.5% for the Southwell profile, except for the wavelength region of $\lambda<\sim1.1$ μm. Note that the optical band gap energy of silicon is 1.1 eV ($\lambda=1.1$ μm) [53], and the reflectance increases considerably due to the band-to-band transition when the wavelength is larger than ~1.1 μm. Comparing the measurement results and the FDTD simulation results, we can see that the two agree with each other reasonably well for the wavelength region from 400 to 1000 nm but the current FDTD model does not account for the band-to-band transition and becomes inaccurate when $\lambda>\sim1$ μm. One thing to note here is that the AR performance of the Southwell profile is not necessarily better when judged from both experimental and simulation data. Apparently, the refractive index changes from 1.5 to 1.8, not from 1.0 to 1.8, so we cannot expect a near perfect AR performance of the Southwell profile in this case.

The measure results are also validated with the electrodynamic simulations of FDTD. A simulation domain size of (3.6p)×(3.6p)×(4p) μm with convolutional perfectly matched layer (CPML)[40] conditions on each boundary was adopted, where $p=2,3,\cdots,9$ for the wavelengths of 400 nm to 1800 nm with a 200 nm interval, respectively. **Figure 23** shows electric fields at the middle symmetric plane of the domain. For simulations, experimentally measured optical constants of the deposited silicon and glass were used (**Figure 18a**, **b**). **Figure 23** shows a simulation example. As shown, a Gaussian light pulse is incident on a graded coating from the top. **Figure 23b-g** present a series of electric field plots showing how a 400nm light propagates and interacts with a linearly graded AR coating without a glass layer. The pulse duration is 9.31 fs. It is clearly seen that only a very small portion of the light is reflected back and the majority is absorbed. The energy flux was calculated using the Poynting vector and the reflectance was calculated as the ratio of the reflected energy flux to the energy flux of the incident light.

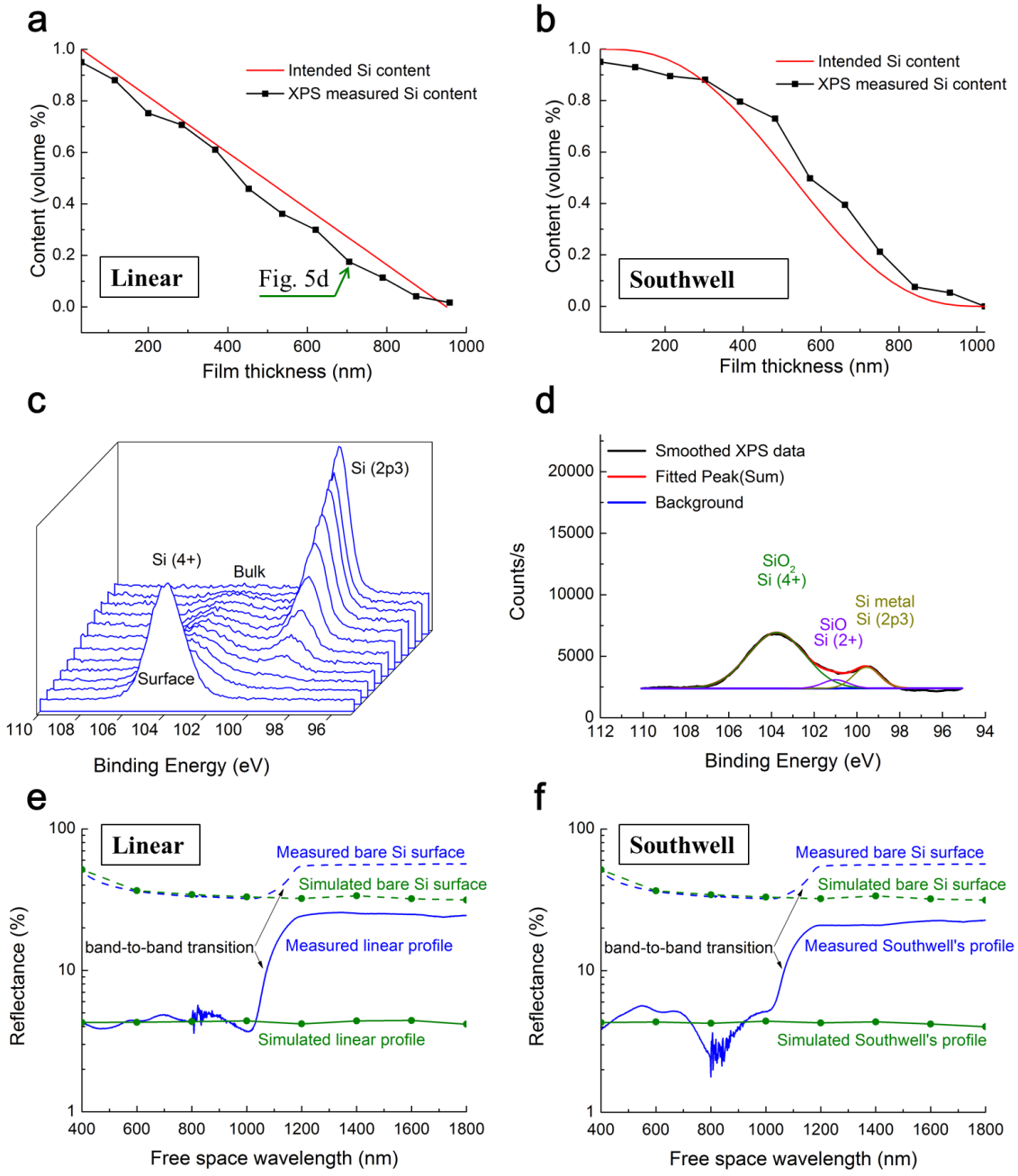

Figure 21. Content profile and reflectance measurement results and FDTD simulation results for AR coatings without a glass layer. (a) XPS content profile measurement result for the linear profile. (b) XPS content profile measurement result for the Southwell profile. (c) XPS peak variation along the coating thickness direction for the linear profile. (d) An XPS peak fitting example for the location shown with a green arrow in (a). (e) Measured and FDTD-simulated spectral reflectance curves for the linear profile and a bare silicon sample. (f) Measured and FDTD-simulated spectral reflectance curves for the Southwell profile and a bare silicon sample.

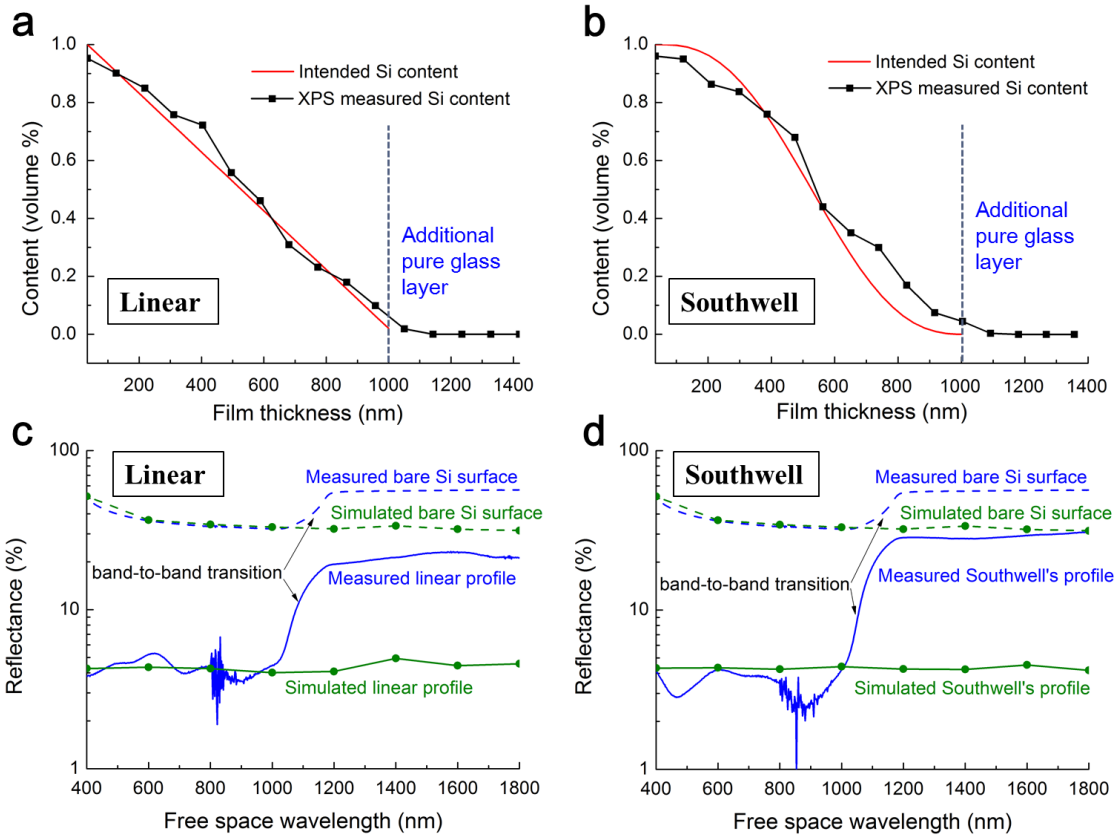

Figure 22. Content profile and reflectance measurement results and FDTD simulation results for AR coatings with a 400nm glass layer. (a) XPS content profile measurement result for the linear profile. (b) XPS content profile measurement result for the Southwell profile. (c) Measured and FDTD-simulated spectral reflectance curves for the linear profile and a bare silicon sample. (d) Measured and FDTD-simulated spectral reflectance curves for the Southwell profile and a bare silicon sample.

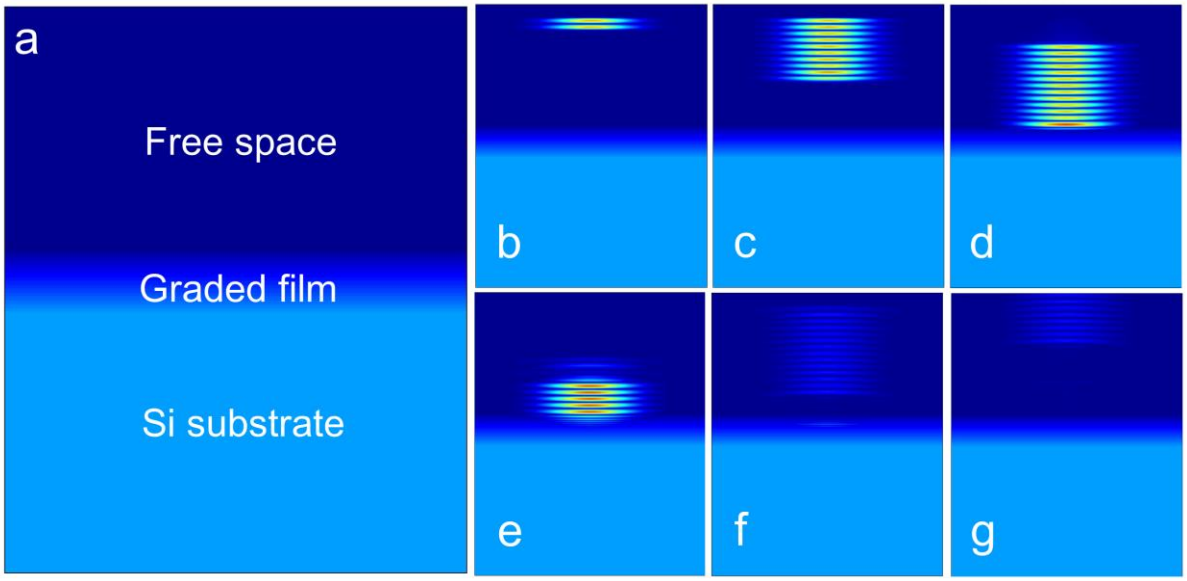

Figure 23. FDTD simulation domain and electrical field plots showing the interaction of 400 nm light with a linearly graded AR coating without a top glass layer. (a) Computational domain. (b-g) Electric field plots showing show the incident light pulse (400 nm wavelength) interacts with a linearly graded coating. As shown in f and g, the reflected light has a very small electric field, indicating that the majority has absorbed by the AR coating.

4.5 Conclusions

We have demonstrated index-graded AR coatings and their fabrication method based on the dual-beam pulsed laser deposition with a pulse control technique. The AR coatings were deposited on silicon substrates and the graded index was realized by continuously controlling the volumetric content percentage of silicon and glass along the coating thickness direction based on a mixture rule for refractive index. The fabricated AR coatings show spectral reflectance values of 2.2~5.5% for a wavelength range of 400~1000 nm. In the case of the Southwell profile with a 400nm pure glass layer, the AR performance was found to be 2.2~4%, which can be considered close to the theoretically best performance of silicon-based solar cells with a protective cover glass. Owing to the material choice of silicon and glass, this antireflection coating can be easily applied to silicon-based solar cells. It can simplify the solar cell structure considerably because from the solar cell to the outer cover glass the composition changes continuously from silicon to glass and the whole structure can be fabricated by one PLD procedure.

V. YSZ graded thermal barrier coatings for high temperature applications

5.1 Introduction of thermal barrier coating

High-temperature thermal barrier coatings (TBCs) are being widely used in the manufacturing of aero-engines, gas-turbine engines or other thermal components for improving efficiencies and increasing components durability, therefore high thermal insulation effect and high adhesion strength are desired for fabricating thermal barrier coatings. A typical TBC consists of two main layers, a MCrAlY superalloy type bond coat (where M=Co, Ni, Fe or combinations of them depending on the material composition of base material) and a YSZ thermal resistant coat [54, 55]. Though TBCs are of vital importance to increase the components durability, the induction of large thermal stress during thermal cycles due to thermal expansion mismatch between the YSZ coat and MCrAlY bond coat and the growth of the thermally grown oxide (TGO) are normally the reasons of TBCs' failure after a certain amount of thermal cycles [56-59]. To increase TBC coated thermal components' lifetime under working cycles, ceramic/metallic functional graded TBCs have drawn a lot of attention [54, 60]. In this section, we will introduce the design, fabrication and characterization of a ceramic/metallic graded thermal barrier coating using a dual-beam pulsed laser deposition method. The graded coating was realized by mixing two different materials, yttria-stabilized zirconia (YSZ), and SUS 316L stainless steel. Because of the gradually changing composition of the two materials, no abrupt interface is expected, therefore the adhesion strength of the coating is increased.

5.2 Design of the thermal barrier coating

A thermal barrier coating with a graded composition can be fabricated by varying the content composition of two different materials along the coating growth direction. Content composition can be calculated and designed using a mixture rule, and in this study, the volume fraction method [61] was employed, which can be described as

$$\alpha^{mc} = f_m \alpha_m + f_c \alpha_c \tag{18}$$

Where α denotes the physical properties of the species (density, thermal conductivity, etc.) and f is the volume fraction; super script mc stands for metallic/ceramic mixture while subscript 'm' and 'c' are for properties of metal and ceramic, respectively.

SUS 316L and 8 wt% YSZ are chosen as the corresponding metal and ceramic target materials and 1μm pure YSZ coating on top of 1μm SUS/YSZ graded coating was planned. Composition inside the

coating gradually varies from 100% SUS at the substrate/graded coating interface to 100% YSZ at the finish end of the graded coating, then another 1μm YSZ coating was deposited. For the graded coating design, only two materials are involved, therefore the linear profile in terms of thickness can be expressed as

$$\alpha_{graded} = (1-x)\alpha_m + x\alpha_c \tag{19}$$

Where x is the coordinate measured from the SUS substrate working surface to the given location inside the metal/ceramic graded coating and $0 \le x \le 1$ μm.When x locates in the region of $0 \le x \le 2$ μm, only pure YSZ will be deposited, so

$$\alpha_{YSZ} = \alpha_c \tag{20}$$

A same 355nm laser with pulse scheme control technique is also used for the design and fabrication of the thermal barrier coating. **Figure 24** shows the schematic view of the overall process procedures.

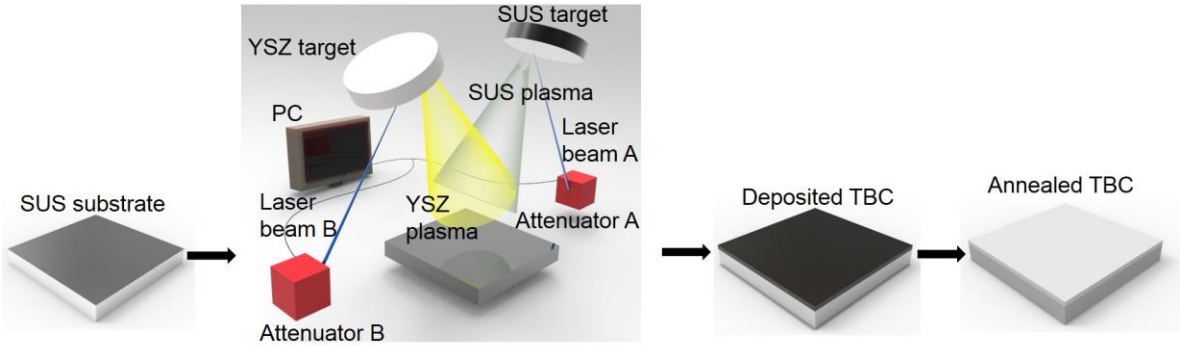

Figure 24．Schematic of overall fabrication process of a SUS/YSZ graded thermal barrier coating by the dual beam pulsed laser deposition technique.

The deposition data for YSZ and SUS 316L are also gathered and they are fitted in a Nelder's model. The designed profile (linear profile) and its corresponding power scheme are also calculated. They are shown in **Figure 25**. For the design of this coating, the whole coating is also divided into 30 small layers for the design and calculation of the graded compositions.

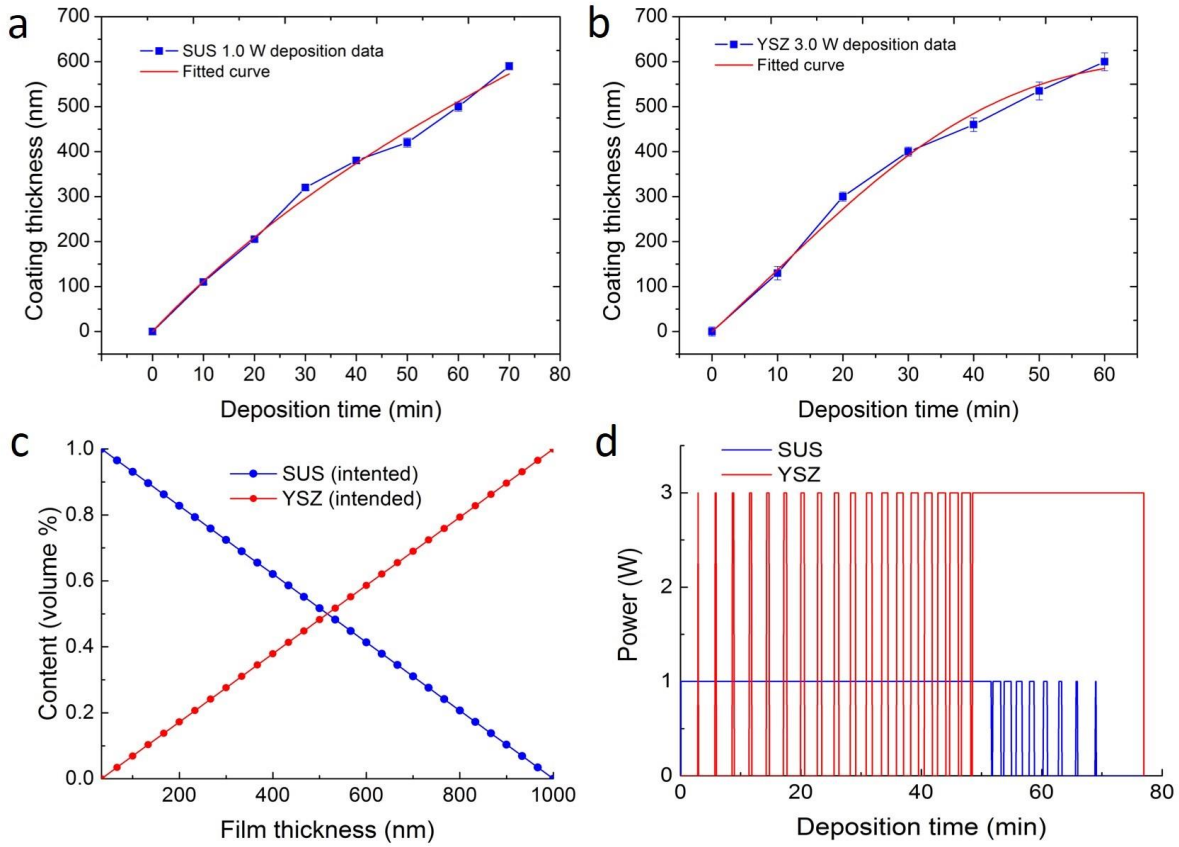

Figure 25. Dual beam pulsed laser deposition for SUS/YSZ thermal barrier coatings. (a) Deposition rate data (blue squares) of SUS 316L corresponding to a laser power of 1.0W. (b) Deposition rate data (blue squares) of 8 wt% YSZ corresponding to a laser power of 3.0W. (c) Designed SUS and YSZ linearly graded composition profile. (d) Calculated and designed power scheme corresponding to the linear profile shown in (c).

After the depositions of YSZ at room temperature, YSZ content appears dark grey due to low deposition temperature. In order to turn it back to white, coatings were simply left in the vacuum chamber and heated at 900℃ (actual temperature is between 300~400, heat resist tape upper limit 400℃, tape remained intact, so the temperature should be around 400 for 30mins. After the annealing treatment, YSZ content appears white again, as shown in **Figure 26**. Three types of coatings are deposited (sample A, B and C) and later, annealed (turned into sample a, b and c) here. Sample A has a 1μm pure YSZ coating on top of SUS/YSZ graded coating with 1μm thickness. Sample B has a 2μm thick pure YSZ coating. Both sample A and B were deposited on SUS foil substrates. In order to see the white color of YSZ better, an additional sample C was deposited with a 1μm pure YSZ on top of a transparent fused silica substrate. All three samples appear to be dark grey right after deposition, as shown in **Figure 26** sample A, B and C. But after annealing, sample A, B and C transformed into sample a, b and c, respectively. Sample a seems dimmer in color compared with sample b due to the SUS

content while sample c is pure white. Both b and c are pure YSZ coatings, so we think the grey-ish color is caused by the back color of SUS substrate.

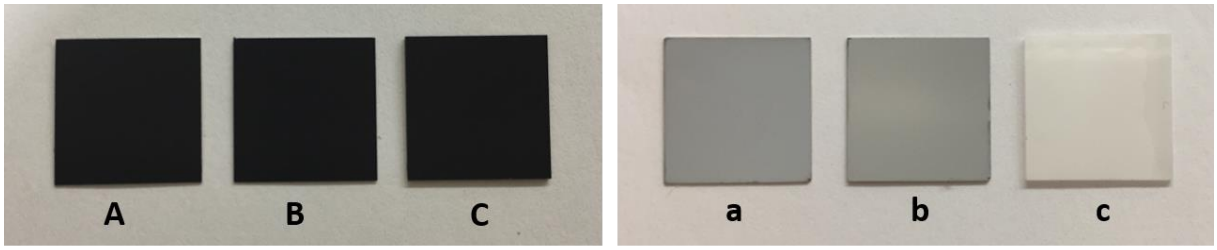

Figure 26. Deposited coatings after annealing. Sample A (a) is 1μm SUS/YSZ graded coating with 1μm pure YSZ coating on top of SUS substrate. Sample B (b) is 2μm thick pure YSZ coating on a SUS substrate. Sample C (c) is 1μm pure YSZ on a fused silica (transparent) substrate. Samples are originally dark grey after depositions, then turned into white after annealing.

5.3 Results of the graded thermal barrier coating

5.3.1 XPS depth profiling for composition validation

A 1μm SUS/YSZ graded coating (without the 1μm outer pure YSZ coating) was analyzed for Fe(2p) and Zr(3d) content. For different materials, sputter etching rates are usually different. Though the etching rates are very difficult to obtain, therefore in this study, we will use 1:1 as the etching rate ratio of SUS and YSZ for simplicity. And the major constituent of YSZ is ZrO_2 and Fe in SUS 316L, so we assume the etching rate ratio of Fe and ZrO_2 to be 1:1. The atomic ratio of Fe(2p) and Zr(3d) can be calculated with the knowledge of the XPS peak area ratios. XPSPEAKS software is employed for the curve fitting of the intensity peaks after the background was subtracted appropriately, and the areas under the peaks were calculated.

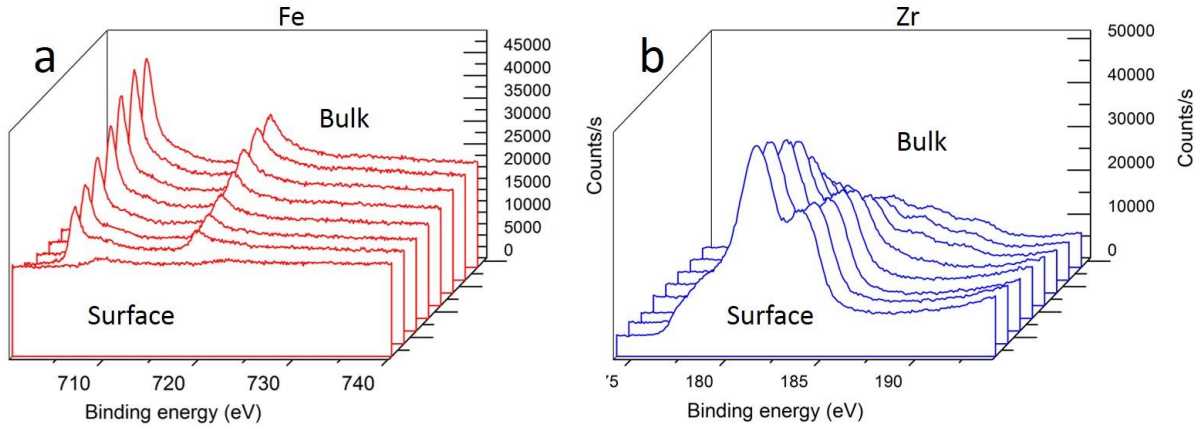

Figure 27. XPS measured results for both Fe and Zr elements; (a) Red lines are the Fe(2p) element evolving intensity peaks. (b) Blue lines are the Zr(3d) element evolving intensity peaks.

Figure 27a and **b** showed the measured Fe(2p) and Zr(3d) XPS intensity peaks, respectively. It is clearly seen that the intensity peaks for Fe(2p) in **Figure 27a** decrease from the inner bulk interface (SUS substrate/coating interface) outward while in **Figure 27b**, intensity peaks for Zr(3d) increase from the inner bulk interface outward. This indicates that the composition of Fe decreases from the bulk interface to the outer surface, and the composition of Zr increases from the bulk interface to the outer surface. Thus, this coating can be considered as metal/ceramic graded. In order to calculate the actual deposited composition profile, relative sensitivity factors for Fe(2p) and Zr(3d) are needed and found to be 2.957 and 2.576, respectively. Therefore, the atomic ratio of two elements can be calculated using

$$\frac{n_i}{n_j} = \frac{I_i / S_i}{I_j / S_j} \tag{21}$$

Where n_i, n_j are the number of atoms of element i and j; I is the XPS intensity and S is the relative sensitivity factor, respectively.

At each measured point (one peak curve in Figure **27a** and the corresponding curve in **Figure 27b**), the atomic ratios were calculated and the results are presented in **Figure 28**. Black squares are the calculated atomic ratios from measured XPS data at a certain depth and solid red line is the intended linear profile. As can be seen in **Figure 28**, deposited profile agrees with the intended linear profile reasonably well, therefore we think our design and depositions for graded coatings are valid.

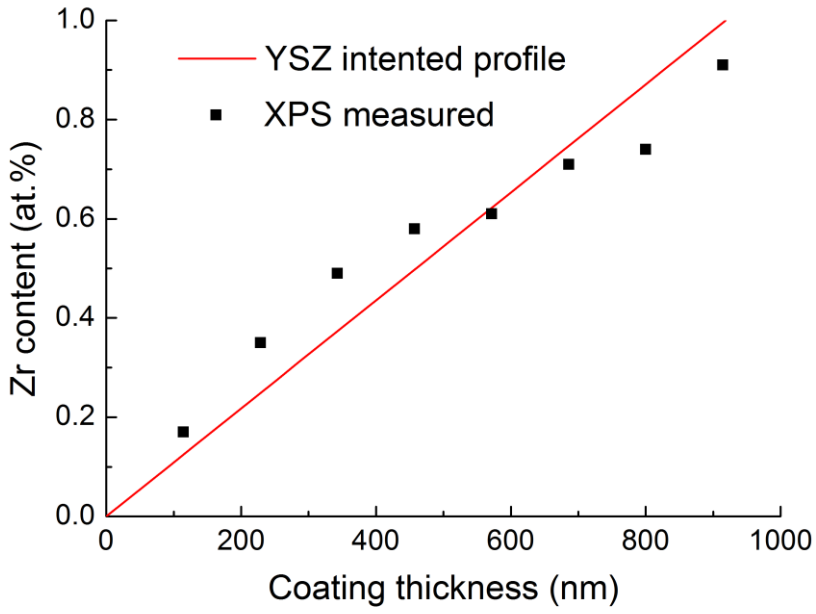

Figure 28. Calculated Zr composition (black squares) from measured XPS results

5.2.2 Thermal barrier effect measured with laser flash technique

For measuring the thermal barrier effect of deposited graded coatings, a thermal graphic camera (Thermo Tracer TH9260) and corresponding software (Thermal Movie) were used for the analysis. Thermal graphic camera can capture IR irradiations and form images. Different color schemes in the images indicate different temperature values. A 1020nm fiber laser (IPG YLS-2000) with a short pulse of 375ms and a power of 100W was used as the heat source for the measurement of the coatings. In order to perform comparisons, a 2μm pure YSZ on SUS substrate, a bare SUS substrate together with a graded coating (1μm SUS/YSZ graded coating + 1μm pure YSZ on top, 2μm in total) were tested. All specimens were irradiated by the same laser pulse on the coating surface and the backside thermal images were captured by the thermal graphic camera. Using the software to process the images, temperature history at the rear surface of each sample can be obtained.

Experimental scheme for measurement is shown in **Figure 29**. A 375ms fiber laser pulse was irradiated on the coating surface in order to emulate the actual working scenarios as heat fluxes reach the TBC first. A thermal graphic camera was setup behind the sample and recorded the thermal radiation due to heat transfer from the TBC to the rear surface of the specimen, therefore the temperature history (highest temperature) can be obtained through image analysis using the software. SUS is highly reflecting and surfaces of graded sample as well as pure YSZ sample are in white color. To increase the specimens' absorption and reduce the measurement noise, 500nm thick DLC coatings (black) were deposited on three types of samples before measurement. Also, the amount of energy input for all three samples can be guaranteed to be equal for reliable results. For each sample, three tests were conducted and the averaged temperature curves are shown in **Figure 30**.

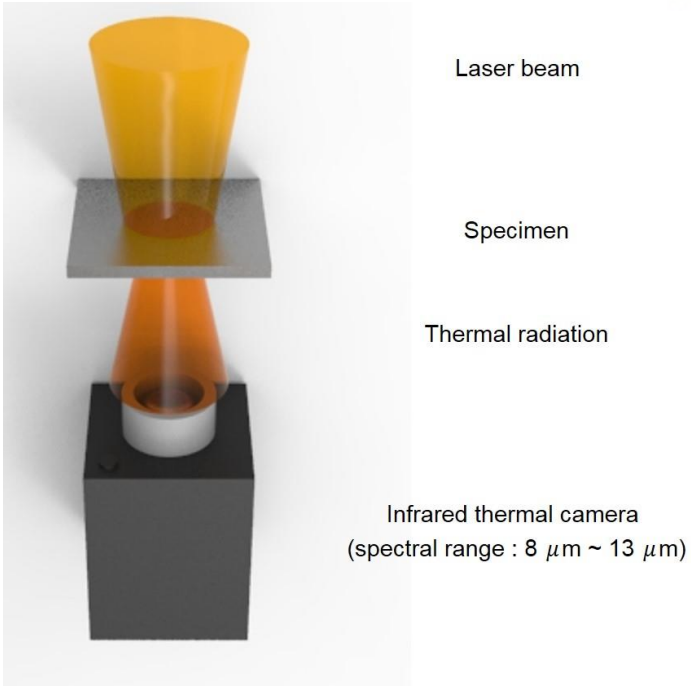

Figure 29. Schematics of thermal graphic camera setup for temperature measurement.

In **Figure 30**, temperature history curves for all three types of coatings are plotted. Black curve denotes the pure SUS substrate while red and blue curves denote graded coating and pure YSZ coating, respectively. All three samples were at the room temperature at first, then a 375ms laser pulse was irradiated at around 0.9s on the time scale. The short pulse was used to minimize the cooling during the measurements. Right after the laser pulse, backside temperatures of the samples increased dramatically to their respective maximum values, then naturally decreased back to room temperature over time. In the figure, maximum temperature of SUS substrate is the highest (~448℃) among all three cases, and this is obvious as pure SUS has higher thermal conductivity. Pure YSZ has the lowest maximum temperature of roughly ~383℃ due to the thermal barrier effect of YSZ. Graded coating case lies in between (maximum temperature ~407℃) because of the coexistence of SUS and YSZ content in the SUS/YSZ graded coating region. The tendency seems reasonable considering the mixture rules of physical properties. Due to the limitation of our thermal camera, maximum temperature of only 500℃ is tested, but we believe that similar behaviors also stand for higher temperatures.

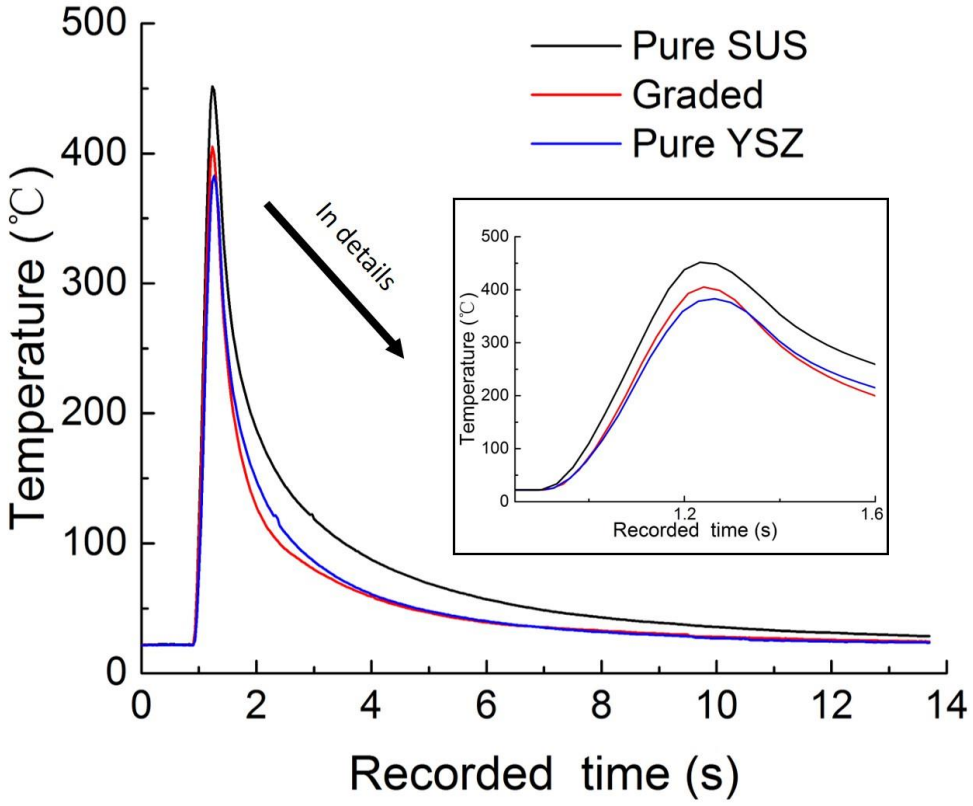

Figure 30. Averaged temperature history curves of three types of samples. Black curve denotes the temperature reaction of a pure SUS substrate after a laser pulse irradiation; red curve denotes the temperature reaction of a 1μm SUS/YSZ graded with a 1μm pure YSZ coating on top with a SUS substrate after a laser pulse irradiation; blue curve denotes the temperature reaction of a 2μm pure YSZ coating on a SUS substrate after a laser pulse irradiation. Laser pulse parameters used for three samples are the same.

For analyzing the thermal properties of the measurements, a method of using half time ($t_{1/2}$, time value at half signal height) and sample thickness (d) for calculating the thermal diffusivity (α) [62] is adopted here. The formula (drawn in **Figure 31**) is developed by Parker et al. in 1961 and can be mathematically expressed as $\alpha=0.1388\times\left(d^2/t_{1/2}\right)$, where d is in the unit of cm and $t_{1/2}$ in the unit of s. The densities ρ of pure SUS 316L and bulk YSZ are 8000 and 5900 kg/m3, and their specific heat c_p values are 500 and 600J/kg·K, respectively. From the measured raw data we can get the half time value $t_{1/2}$ for SUS, graded and YSZ samples and they are 0.1387, 0.1424 and 0.1427s, respectively. Therefore, all three thermal diffusivity values for three samples can be obtained easily as $\alpha_{SUS}=4.0029\times10^{-6}$, $\alpha_{Graded}=3.9773\times10^{-6}$ and $\alpha_{YSZ}=3.9687\times10^{-6}$ m^2/s. Using the diffusivities and density/specific heat values we can now calculate the thermal conductivities easily by getting the product of diffusivity, specific heat and density, described as $k=\alpha c_p\rho$. For three samples, their thermal

conductivity values (coating and substrate as one body) are now calculated as k_{SUS} = 16.0116, k_{Graded} = 15.9016, and k_{YSZ}=15.8645W/m·K. With the knowledge the thermal conductivity values (as one body) and use the mixture rule reversely, we can get the conductivity values for the graded coating and pure YSZ (without substrates), and they are $k_{Graded'}$=4.8573 and $k_{YSZ'}$=1.1431W/m·K. Therefore we have obtained the thermal conductivity values for pure SUS (16.0116 W/m·K) and pure YSZ (1.1431W/m·K), too. Compare the results with literatures ($k_{SUS''}$=21.5 W/m·K and $k_{YSZ''}$=1.5~2.05 W/m·K), we found out that our results are a lot smaller, possible reasons are experimental errors and during the measurements, our environment isn't perfectly isolated so there is heat loss during temperature rising, and that will account for the smaller conductivities. Also, our materials are PLD deposited so some extend of porous structures are expected, this will also contribute to the smaller conductivity values.

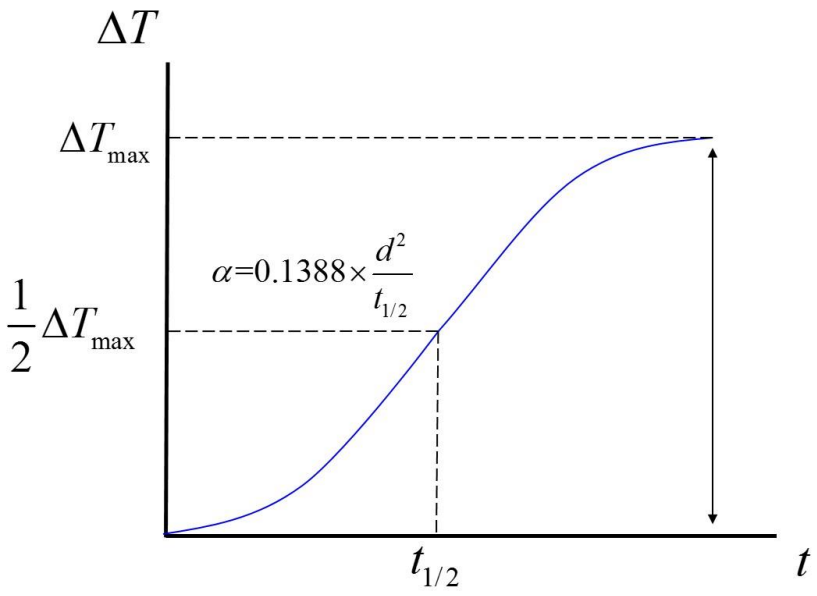

Figure 31. Scheme of thermal diffusivity calculation.

5.3.3 Adhesion strength measurement with indentation cracking method

In this study, TBCs' adhesion strength was also examined using the indentation cracking method [63, 64]. The measurements are performed with a Rockwell C type (KDMT-170) diamond indenter. The interfacial crack radius (c) and the indentation load (P) are the two main parameters required for the adhesion strength analysis. If the load P is applied sufficiently, crack radius c will increase with load P. Hence, the parameter dP/dc, can be calculated and considered as the critical parameter which is proportional to the TBCs' adhesion strength. For the measurements, three different loads, 600, 1000, 1500N were applied to two graded samples (1μm SUS/YSZ graded coating + 1μm pure YSZ on top),

2 pure YSZ samples (2μm thick) and 2 pure YSZ samples (1μm thick) for comparisons. Instead of using 200μm SUS 316L substrates, 2mm thick substrates were used for the measurements due to the indentation test requirements. Some example optical micrographs of the indentation tests are shown in **Figure 32**. From top to bottom, indentation load increases from 600 to 1000 to 1500N for each type of coatings. As expected, the areas of cracked regions (including micro-crack, color changing regions) marked with blue ellipses, increase with indentation loads. For the 2μm pure YSZ coatings, some notable cracks along with some micro-cracks and color changing regions are shown in the figure, indicates that the adhesion strength is relatively weak. 1μm pure YSZ coatings are also prepared for comparison purpose in the indentation tests. In terms of the failure mode of the coatings, 1 μm YSZ seem to have less delaminated areas but more microcracks and larger color changing regions. With the same indentation loads, neither notable cracks nor micro-cracks/color changing areas can hardly be seen, and virtually no substrate exposure. This indicates that due to the graded content of SUS in the coating, adhesion strength of the graded coating is good between the coating and the substrates. To quantify the results, three points for each load were tested on the samples and the averaged values were shown in **Figure 33** in terms of dP/dc values.

The cracked regions are normally not in a perfect circle shape, as shown in Figure **32**, in order to perform the calculation, crack radius c was estimated by the radius of a circle with the same amount of cracked area as the original ellipse. For each type of coatings, two sample were tested and three tests for one indentation load on each sample were conducted. The averaged results are shown in Figure **33**, dP/dc values for graded coatings and pure YSZ coatings are in black squares. Due to the nature of a graded coating, its adhesion strength is expected to be higher than non-graded ones, and our results agree well with this. The graded coating (1μm SUS/YSZ graded coating + 1μm pure YSZ on top) has the highest dP/dc value up to 9.41N/μm while other two types of coatings have the dP/dc values of 8.35 (2μm YSZ) and 8.43 N/μm (1μm YSZ), respectively. Regardless of the thickness differences of the two pure YSZ coatings, their dP/dc values are quite close to each other, indicates they have similar adhesion strength, but as can be seen in Figure **33**, 1μm thick coatings seem to be less stable in terms of dP/dc values, and we believe thinner coating thickness is the main reason. Comparing all three types of coatings, the graded coating has the largest adhesion strength, as well as coating's stability in terms of dP/dc values. The graded region can work as the bond coating in traditional TBCs.

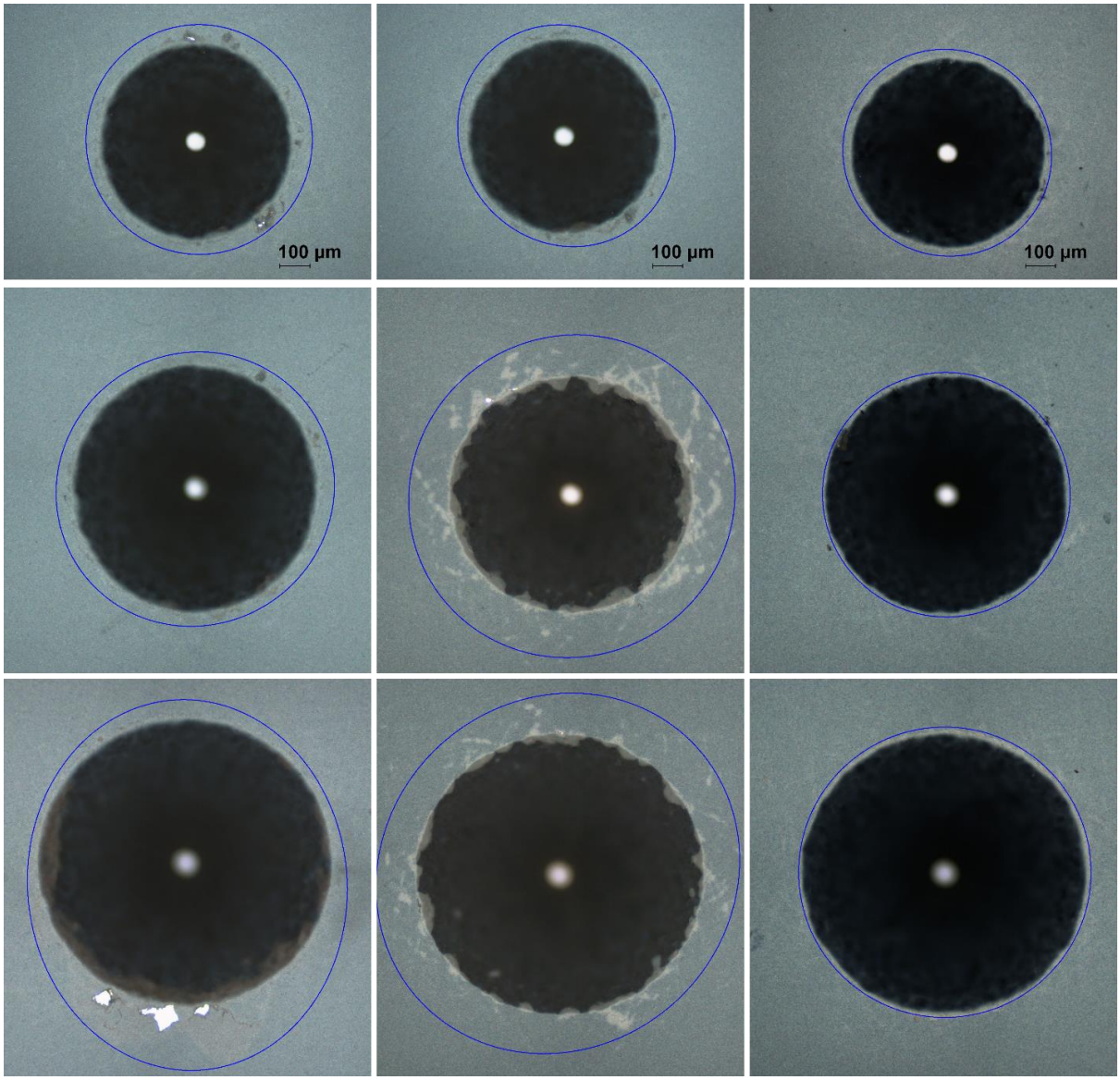

Figure 32. Optical microscope images of TBCs after Rockwell indentation cracking test. From top to bottom, indentation load increases from 600 to 1000 to 1500 N. Cracked regions (including micro-cracks) are denoted with blue ellipses.

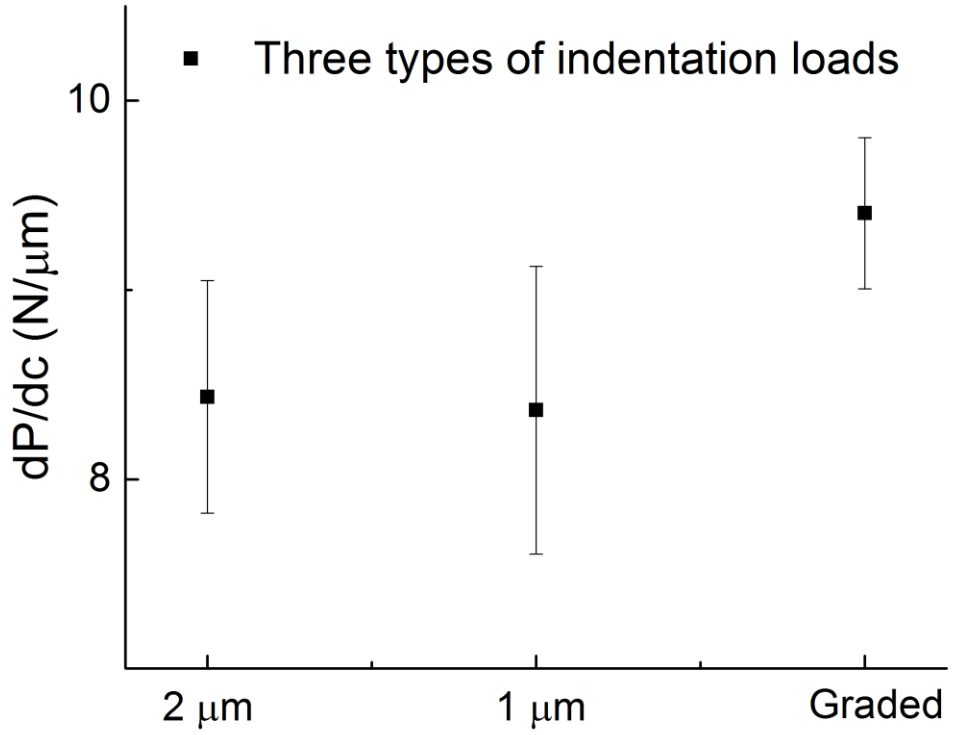

Figure 33. Calculated adhesion strength based on the dP/dc values. Black squares denote the averaged dP/dc values obtained from 600, 1000, 1500N indentation loads for three types of coatings.

5.4 Conclusion

In this tudy, we have successfully designed and fabricated YSZ-SUS graded coatings by using a dual-beam pulsed laser deposition method and investigated their properties in terms of thermal conductivity and adhesion strength. Deposited YSZ coatings showed a good thermal barrier characteristic (thermal conductivity of ~1.14W/(m·K)) and the graded region provided much improved adhesion strength in comparison to pure YSZ coatings. With further research, we believe that much thicker, industry-scale functionally-graded YSZ coatings (several hundred micrometers thick) could be fabricated based on this approach, if a high-power picosecond laser (say, 500−1000W) is used with a proper scaling-up method.

VI. FABRICATION OF ULTRA-SHORT FOCAL LENGTH INDEX-GRADED MICROLENS ARRAYS BY A FEMTOSECOND LASER ASSISTED WET ETCHING AND DUAL BEAM PULSED LASER DEPOSITION FOR NIR APPLICATIONS

6.1 Introduction

Optics and opto-electronics have played an increasingly significant role in today' world of information processing, as the performance of processing, photovoltaic devices, sensing, imaging, illumination and fiber communication is expected to be furtherly enhanced, as technology develops. Therefore, massive parallelism and micro miniaturization are introduced to make those photonic systems much faster and mush smaller in scale (Ottevaere et al., 2006)[65], and high precision, low cost micro lenses and micro lens arrays are drawing a lot of attention over the past a few years. A variety of design and fabrication techniques for refractive micro lenses and micro lens arrays have been developed by many research groups and laboratories.

The most commonly used materials for micro lens array fabrication is glass, and various fabrication techniques have been proposed for this purpose: Borrelli et al. (1985) presented 2D micro lens arrays produced in a homogeneous photosensitive glass by a photothermal expansion technique [66]; Oikawa et al. (1981) introduced a distributed-index planar micro-lens glass array prepared from ion exchange technique [67]; Gale (1997) illustrated the method of fabricating glass micro lens arrays with reactive ion etching [68]; Wakaki et al. (1998) successfully fabricated micro lenses and micro lens arrays which were formed directly on a surface of a glass plate by use of a CO2 laser irradiation [69]. Also, many new lightweight optical materials have emerged and become the research topic of interest. For example, optical graded polymers have been used in many applications due to its controllability of mechanical and thermal properties, workability and low cost. Several fabrication techniques have been reported: photoresist reflow (Popovic et al.,1988)[70], laser beam shaping (Jay et al., 1994) [71], photopolymerization (Croutxe-Barghorn et al. , 2001) [72], laser ablation (Naessens et al. ,2003) [73], microjet print (MacFarlane et al. 1994) [74] and direct laser (Gale , 1997) [68].

Most of the micro lens arrays fabrication methods are still viable up to date and the fabricated arrays can meet the optical quality requirements, though, some of them are more expensive or more complicated than others. Choosing which fabrication methods strongly depends on your material choices and merits of the techniques (mass production/ rapid prototyping/ or better integration).

Microlenses are basic elements for any miniaturized optical setups[75]. They exhibit low aberration and distortion[76], high temporal resolution and infinite depth of field [77-81], and are the key components in photonic and opteletronics with a wide range of applications, such as in 3D imaging systems, sensing systems, fiber optic communication and optical medical systems[76, 82, 83]. With the enhancement in performance of the optical sensing/imaging systems, there is an increasing demand for ultrasmall microlenses[84] (with lenslet diameter less than 10 μm) to be used for increasing the light collection efficiency, particularly in the infrared/near infrared spectrum in charge coupled devices (CCDs), which are the essential parts of the modern digital cameras and other sensor-type devices and applications[85]. As the pressing need continues to rise for higher resolution digital cameras, the call for smaller pixel size of CCDs leads to a very demanding challenge for smaller microlenses exhibiting shorter focal lengths, larger numerical aperture and less spherical aberrations.

In the recent decades, an enormous amount of research has been dedicated towards the fabrication of micrometer-scale microlenses with short focal lengths, such as thermal reflow technique [84, 86, 87]. Formation of the lenses is usually caused by the surface tension of the material when it is in a thermalpalstic or liquid state, resulting a spherical surface[88-90]. The fabrication processes are relatively simple and cost effective, which makes them economical in large volume. However, it is very difficult to fabricate arbitrary shaped microlenses since the shapes of the lenses are determined by the fabrication parameters only (such as wettability, temperature, pressure and process time, etc), and the fabricated lenses usually have the sizes of tens or several hundred micrometers, resulting the focal lengths in the similar range or larger. Limited results on ultrashort focal length (around or less than 10 μm) microlenses have been reported. Dai *et al.*[84] demonstrated a liquid-crystal (LC) based reconfigurable microlens, which utilizes vertically aligned carbon nanofibers (CNFs) grown on a Si substrate. Its focal length is reported to ranging from 6 to 12 μm (depends on the applied voltage). There is no physically formed spherical or aspherical lenses in this case, the microlens is “created” with the refractive index profile, which is generated via the electrical field from CNFs under voltage. Casse *et al.*[85] demonstrated a 2D photonic crystal microlens with an ultrashort focal length of ~12 μm using negative refractive materials. However, both methods are considerably difficult and complex, not suitable for mass fabrication.

In pursuit of a high-efficiency, low-cost fabrication technique, femtosecond laser assisted chemical etching method is adopted in this study for the well-controlled microlens array fabrication, then a standard replication process for convex lens array is carried out. Finally, a novel dual beam pulsed laser deposition is applied to deposit a considerably thick graded carbon/Si coating on top of the PDMS lenses, making them graded. In this study, a hexagonal-densely-packed PDMS convex microlens array

with an ultrasmall lenslet diameter around 6 μm, a sag height of 1.6 μm and a pitch of 8 μm is fabricated. The focal length is calculated to be around 4.12 μm and a large N.A value of 0.73 (based on FDTD simulations) is presented. A novel dual beam pulsed laser deposition technique was adopted to realize a 600 nm graded carbon/Si layer on top of the PDMS microlenses, making the lenses graded and shortening the focal length even more. The lenses after deposition have a smaller focal length of ~ 2.9 μm (validated via FDTD) and a higher N.A of ~1.24. This is the shortest focal length reported, and the first experimental realization of GRIN microlens arrays with dual beam pulsed laser deposition, to the best of the authors' knowledge. The 600 nm only graded region is proved to reduce the focal length by 29.6% and increase the N.A by ~66%. The lenses have the profile of a hyperbola line, which is the perfect profile for ideal refractive lenses. Imaging tests were also conducted for the lenses before and after deposition, clear and uniform images were captured, showing very good optical imaging properties of the lenses. Due to the extremely low transmission in the visible light region but much higher transmission in the near IR region for Si and carbon, the index-graded microlenses are suitable to cutoff visible lights and perform well for near IR lights, therefore they can be used in many near IR applications, such as near-field imaging, fine sampling of an object under consideration in integral imaging microscopy and shortwave detectors, etc.

6.2 Experimental section

The fabrication process of graded microlens arrays is divided into three main steps, as illustrated in **Figure 34**. Firstly, femtosecond laser microfabrication is employed to generate small lens patterns (pitch distance and hexagonal packed arrangement are controlled in this process.); the fabricated sample is then put in HF solution for etching in order to obtain perfectly shaped concave microlenses (Figure **34a**). Secondly, the replication process is conducted for the formation of convex lenses (Figure **34b**). Finally, a dual beam pulsed laser deposition is performed to form a graded coating on top of the fabricated PDMS lenses, making the lenses graded Figure **34c**.

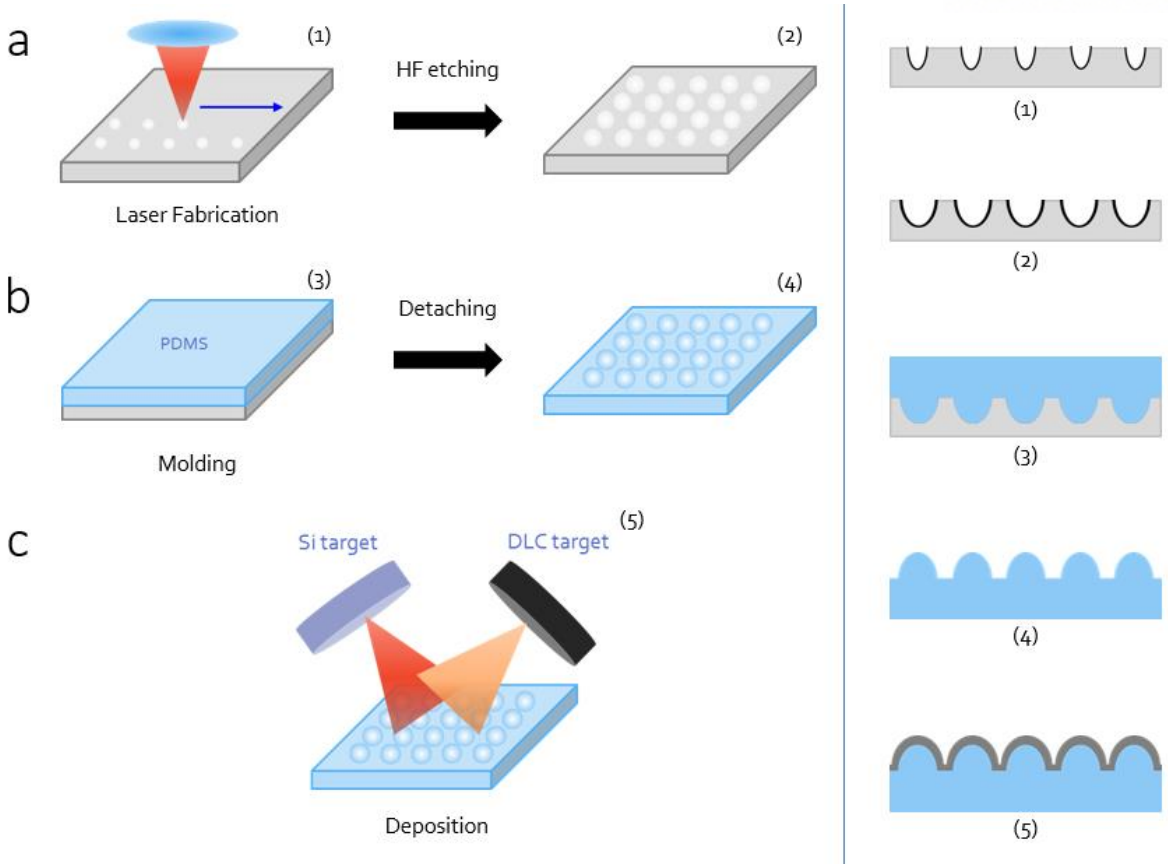

Figure 34. Fabrication of a DLC/Si graded lens array. (a) Femtosecond laser fabrication of negative lens array on fused silica with wet etching; (b) PDMS replication of making convex lenses. (c) PLD deposition for graded coating.

6.2.1 Fabrication of concave lens template mold with femtosecond laser and wet etching

Femtosecond laser assisted wet etching has been proved to be a very powerful and viable technique to fabricate uniformly distributed large-area microlens arrays with excellent optical performances[91]. A 1030 nm femtosecond laser (Pharos15-200-PP) is employed as the energy source for drilling smaller craters on the surface of a 0.5 mm thick fused silica substrate. The fused silica substrate is cleaned in an ethanol solution with ultra-sonic bath for 20 min to remove the grease and contaminations, then it is dipped in DI water with ultra-sonic bath for another 15 min for a clean surface. After dried with N2 gas, the cleaned substrate is fixed on a 3D x-y-z linear stage. The femtosecond laser (1030 nm, 220 fs, 200 kHz) is initially focused at the upper surface of the fused silica substrate. The incoming laser beam irradiate on the surface in the normal direction to the substrate surface with a microscope objective lens (Mitutoyo Plan Apo NIR ×20, N.A=0.4). Breakdown induced craters on the fused silica substrate surface are achieved with one or multiple laser shots and the initial crater diameter and depth are determined by the laser parameters, such as laser power, irradiation time and the number of shots given

at each location. Higher power, longer irradiation time and larger shot numbers all contribute to larger and deeper crater dimensions. After finishing the irradiation of one position, the substrate was translated to another position and the process repeats until a whole well-designed lens array are fabricated. In this study, the pulse energy used for the fabrication is chosen to be 0.6375 μJ. Pitch distance of the arrays is 8 μm by design and the lenses are hexagonally packed. After the femtosecond laser irradiation, the inner surfaces of the craters are not smooth at all, therefore another ultra-sonic cleaning process is carried out to remove the debris before chemical etching. For the wet etching process, 10% of HF is used for 30 min and it is also put in an ultra-sonic bath for removing air bubbles and uniform etching. The laser induced craters evolve and form smooth, uniform concave spherical-like microstructures in the isotropic chemical etching process.

6.2.2 Fabrication of convex lenses with a replication process

After the concave lens array is successfully fabricated, the convex lens array can be made with a standard replication process. The polydimethylsiloxane (PDMS) pre-polymer is prepared by mixing Dow Corning Sylgard 184 silicone elastomer and Sylgard 184 curing agent together with the ratio of 10:1. After being thoroughly mixed, it is put in the vacuum chamber and degassed for 30 min to remove air bubbles. Once the degassing is done, the liquid mixture is poured onto the fused silica substrate top surface (with the fabricated concave lenses) and the substrate is baked in an oven for 6 hours at the temperature of 60 ℃. The liquid polymer solidifies in the oven, then cured PDMS is carefully peeled off. After the de-molding, convex lens array is successfully fabricated. The replication process is shown in **Figure 34b**.

Figure 35a shows the scanning electron microscope (FE-SEM, Quanta 2000, FEI) observation of the fabricated PDMS microlens array. As shown in the SEM image, the lenses are in a hexagonal arrangement and they are uniformly packed. The diameter of each lens is measured to be around 6 μm. The 3D surface morphology is also investigated with a laser scanning confocal microscope (LSCM, Olympus LEXT OLS3100). The result is shown in **Figure 35b**. The cross-section lens profile is measured as well with the confocal microscope and the lens profile is shown in **Figure 35c**, and it is fitted into a hyperbola line since it is the ideal profile for a perfect refractive lens. And we can see the fabricated lens profile agrees very well with the hyperbola fitting line. The height of the sag is measured to be around 1.6 μm from the profile result. Based on the measured results and the hyperbolic fitting curve of the lens profile, the focal length f of the lenses can be calculated based on the equation below[92],

$$f = \frac{R}{n-1} \tag{22}$$

Where n is the refractive index of PDMS (n=1.406) and R is the radius of curvature at the vertex,

$$R = \frac{(K+1)H}{2} + \frac{r^2}{2H} \tag{23}$$

Where K is the aspherical constant, H is the sag height and r is the lens radius, respectively. For a hyperbola, K= - e2 < -1, and e = 2.202 is the eccentricity of the fitting hyperbolic equation. The calculated focal length of the microlenses is around 4.5 μm.

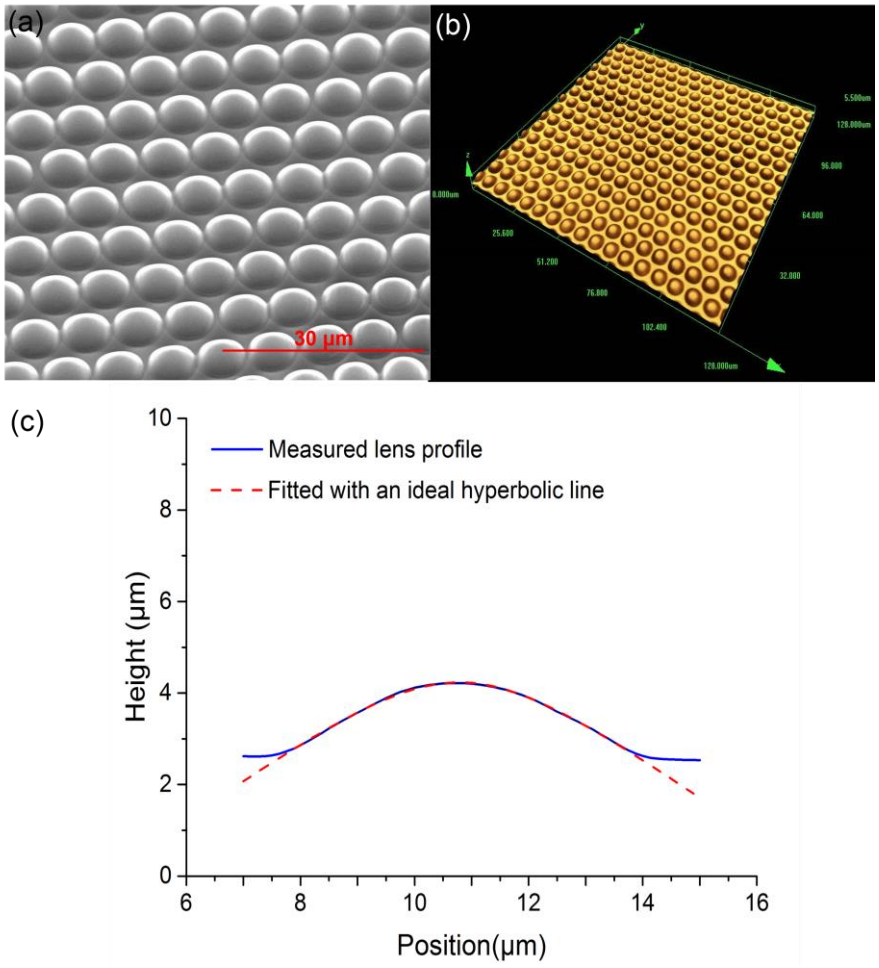

Figure 35. (a) SEM observations (45°tilted) of the fabricated PDMS convex microlens array; (b) (c) Confocal measurements for 2D and 3D surface morphology of the fabricated PDMS lenses; (d) Measured lens profile and a hyperbolic fitting line.

The intensity distribution (measured with a Laser Scanning Confocal Microscopy FV1000, Olympus) of the PDMS lens array are also investigated with microscopes and CCD cameras. The light intensity distribution test results are shown in **Figure 36**. **Figure 36a** shows the 3D image of the microlens array taken by the confocal microscopy. The dotted blue line crosses through the centers of three microlenses, and the intensity distribution result along this line is shown in **Figure 36c**. **Figure 36b** shows the microscopy confocal image of the lenses in **Figure 36a** illuminated by a normally incident 488nm laser beam. Each red dot stands for a focusing point of the lens. The white-dotted line selects three dots, and they are the center positions of the three lenses crossed by the blue dotted line in **Figure 36a**. From the results we can see that the lenses are uniformly distributed in a hexagonal arrangement (**Figure 36a** and **b**); each single lenslet works well and form a clear focusing point (in **Figure 36b**); and the sharp intensity distribution of the three focusing points shows that each lens possesses a well focusing ability despite there is noise in between of the sharp points.

The imaging test is conducted with a Total Internal Reflection Microscopy (Olympus). The light source for this test is a Halogen lamp, which emits the lights from visible to near IR range. An “S” letter is used as the imaging object. As is shown in **Figure 37**, very clear and crisp image of “S” is presented in every single lenslet. It demonstrates that the fabricated PDMS lenses have very good optical imaging properties under the halogen lamp lights.

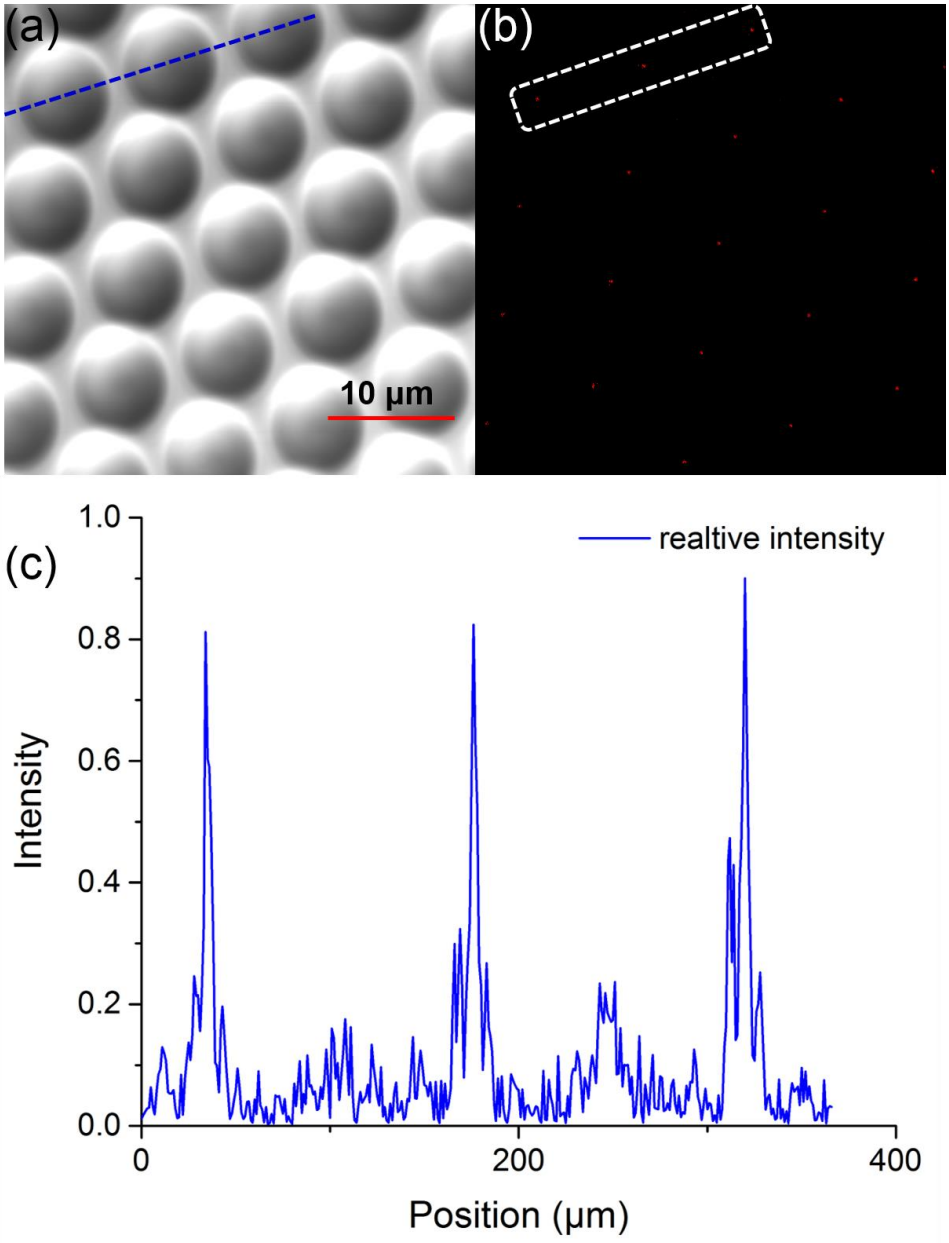

Figure 36. Intensity test results. (a) 3D image of the microlens array taken from confocal microscopy; (b) Microscopy confocal images of the lenses illuminated by a normally incident laser beam. (c) Intensity distribution of the focusing points in (a) along the dotted blue line, it is also the results of the white dotted line selected rectangular area in (b).

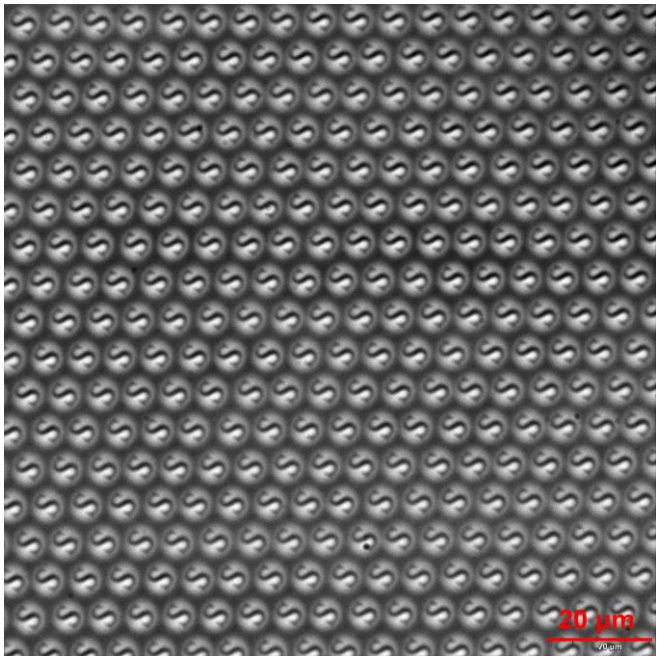

Figure 37 . Imaging performance of the PDMS microlens array with a Halogen lamp as the light source and a “S” letter as the imaging object.

6.2.3 Graded deposition with a dual beam pulsed laser deposition

A graded coating with a linear refractive index profile can be fabricated by depositing two different optical materials along the coating growth (thickness) direction with good control of the material flux for each constituent. Before the deposition, a predesigned index profile needs to be determined. In this study, we will adopt the linear profile for simplicity. In order to design an index gradient profile, the refractive index of material mixture needs to be calculated as a function of mixture composition. Several mixture rules for refractive index are available in the literature[50], and in this study, the volume fraction method[42, 50] is applied, which can be written as

$$n_{mix} = \phi_1 n_1 + \phi_2 n_2 \tag{24}$$

Where n_1, n_2 and n_{mix} are the refractive indices of constituent 1, constituent 2 and the mixture, respectively; ϕ_1 and ϕ_2 are the volume fractions of constituent 1 and constituent 2.

In this study, DLC (carbon) and Si are chosen as the two optical materials for the GRIN lens (graded coating) fabrication because of their low transmission in the visible light region and higher transmission in the near IR region, making them desirable for near IR applications and devices. A 600nm thick graded coating is planned on top of the fabricated PDMS microlens array. The intended

composition varies from 100% of pure DLC at the microlens surface to 100% of pure Si at the lens-air interface smoothly and gradually. The linear profile is mathematically expressed as

$$n_{linear}(x) = n_{Si}x + n_{DLC}(1-x) \tag{25}$$

Where x is the coordinate measured from the PDMS lens surface to the given location inside the graded coating and $0 \le x \le 600$ nm.

Volumetric content profiles of both materials are presented in **Figure 38c**. Blue line stands for the intended content profile of DLC while red line stands for Si. As seen in the figure, the composition of DLC decreases linearly from the PDMS lens interface to the coating-air interface while that of Si increases, therefore we can expect the index of the graded coating changes gradually as well based on the volume fraction mixture rule.

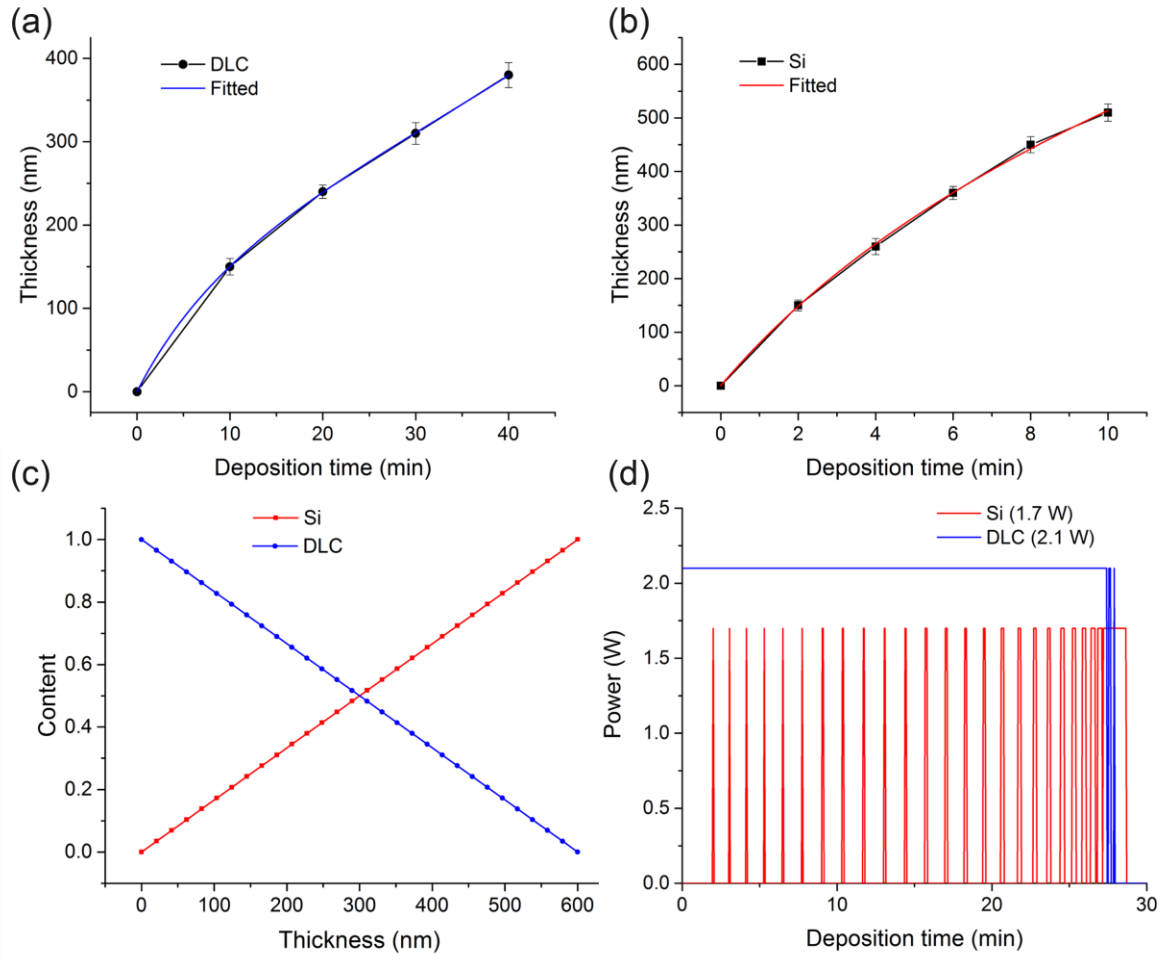

Figure 38. Dual-beam PLD design of graded DLC-silicon coatings. (a) Deposition rate data (black circles) of DLC corresponding to a laser power of 2.1 W. The blue line is the fitting line. (b) Deposition rate data (black squares) of silicon corresponding to a laser power of 1.7 W. The red line is the fitting line. (c) Designed silicon and DLC volumetric content profiles for the linear profile. (d) Calculated power scheme corresponding to the linear profile shown in (c).

For the novel pulsed laser deposition technique, a 355 nm, 6 W picosecond laser (Coherent Talisker 355-4) is used as the energy source. The picosecond laser has a pulse width of 10~15 ps and a repetition rate of 200 kHz. A single laser beam is split into 2 beams using a 50/50 reflection/transmission beam splitter, and each split beam is controlled by a motorized attenuator (Metrolux ML 2100). Both attenuators are connected to a PC via an attenuator controller and the action of the attenuators are governed by an inhouse LabVIEW program. In this manner, the intensity of each split beam can be monitored and varied independently and simultaneously for the deposition process (**Figure 34c**). One of the split beams is focused on the DLC target inside the deposition vacuum chamber and the other beam is focused on the Si target. When the beams hit the target materials, silicon and glass plasmas are induced. The generated plasma plumes are mixed together uniformly in space inside the vacuum chamber and then are deposited on the prepared PDMS lens array sample. In this way, a mixture of two materials can be deposited on one single sample. By controlling the material fluxes of both materials, a graded optical coating with a pre-designed content profile can be fabricated[27, 28]. In this study, high purity graphite (99.999%) and silicon (99.999%) are used as the targets, and prefabricated PDMS microlens array (**Figure 35a**) is used as the substrate. The PLD process is carried out at room temperature (~20∘C) in a vacuum chamber, and the pressure is maintained at ~10^{-5} Torr using two turbo molecular pumps. Note that both materials are easily ablated by a 355 nm picosecond laser, therefore it is not easy to maintain the material fluxes for a long enough time to build a coating because of the defocusing of the beams. To overcome this issue, in this study, both target materials' positions are shifted by 100 μm to new spots for every 2 min deposition, for the purpose of generating continuous plasma plumes during the course of the coating deposition process.

For building up a graded coating with a designed linear content profile, deposition rate of each material has to be known precisely for accurate deposition. **Figure 38a** and **b** show the deposition data curve of graphite (obtained with a laser power of 2.1 W) and silicon (obtained with a laser power of 1.7 W), respectively. Due to the low deposition (ablation) rate of graphite target, the data is gathered up to 40 mins with a 10 mins interval. Si has much a higher deposition rate, therefore 10 mins of total deposition time is sufficient to build a 600 nm thick graded coating, since only 300 nm thick of Si and 300 nm of graphite are required. Deposition data for Si are gathered with a 2 mins interval. Each deposition curve was then fitted to the Nelder model[29],

$$\theta(P,\ t)=\frac{t}{b_0+b_1t+b_2t^2} \tag{26}$$

Where θ is the coated thickness (given as a function of the laser power P and deposition time t), and b_0, b_1, b_2 are fitting coefficients. The fitting lines are shown as blue (DLC) and red (silicon) solid lines in **Figure 38a** and **b**.

With the knowledge of the obtained deposition data for DLC and Si, now the graded coatings can be fabricated. For a predesigned 600 nm thick linearly graded coating, equally spaced 30 layers (hypothetically) can be assumed for the calculation and design. For each layer the amounts of silicon and graphite required to build this specific layer can be easily calculated based on the given linear profile. In **Figure 38c**, the dotted points represent the locations of the layer boundaries. Apparently, the number of layers can be changed. A larger layer number leads to a thinner layer thickness, which makes the deposition (based on the intended linear profile) smoother and more accurate. Knowing the amounts of materials in each hypothetical layer, the required effective deposition times for both materials can be easily calculated from the presented fitted deposition data (fitting curves in **Figure 38a** and **b**). (Note that the effective deposition time is the amount of time required to deposit the required amount of specific material (in this case, DLC and Si), which is obtained from the fitting deposition curve when a split laser beam with the given power is continuously irradiated on the target material.) Comparing with the effective deposition time, the actual deposition time to deposit one layer for both materials, which is the naturally marching time, should be the same. In this study, we devised a method to make each of the two attenuators function as a beam shutter to control the physical deposition time for each material, making it equal to the required effective time for this layer. In other words, for both target materials, split incident laser beams can be pulsed using the attenuators to deposit the exact amount of required materials for this layer during the same amount of actual deposition time. This method is based on pulse control scheme, therefore only one deposition curve (one power value) for each material is sufficient to build any reasonable profile, and only two transmission values of the attenuator are needed for one material. The calculated laser power scheme for the linearly graded coating is presented in **Figure 38d**.

Once the deposition is finished, SEM observations (FE-SEM, Quanta 2000, FEI) and confocal measurements for the lenslet cross-section profile (LSCM, Olympus LEXT OLS3100) are conducted. Results are shown in **Figure 39a** and **b**. In **Figure 39a**, the GRIN lenses are also uniformly packed and distributed but not as smooth as the PDMS lenses in **Figure 35a**. Some small particle can be observed on the surface of the lens array. And this is due to the PLD deposition process since the generated plasmas during the course of deposition contain particles or droplets of different sizes. The particle sizes

can be somewhat controlled by PLD parameters, such as laser power, material type, distance between the material target and the substrate, etc.

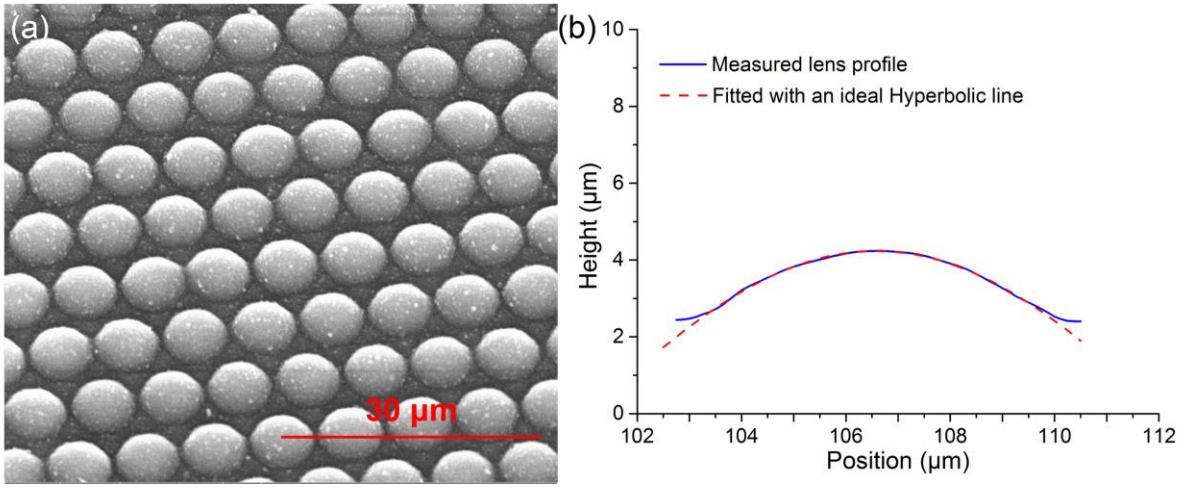

Figure 39. (a) SEM observations (45°tilted) of the graded convex microlens array; (b) Measured lens profile and a hyperbolic fitting line.

For the graded refractive index validation, the content profiles of DLC and Si from the graded coating are examined. The x-ray photoelectron spectroscopy (XPS) depth profiling method (K-alpha spectrometer, Thermo Fisher) was adopted and the measured XPS peak variation results for both C1s (that of carbon) and Si2p (that of Si) are shown in **Figure 41a** and **b**. Starting from the coating surface (air-coating interface) to bulk (PDMS lens surface) inside, the Si2p peak decreases while the C 1s peak increases, indicating that, as expected, the Si content decreases and the DLC content increases as the location moves inward. In another word, the coating is a Si/DLC graded coating. The XPS depth profiling etching is conducted with 1 keV Argon ion energy. Etching area was 2 mm × 4 mm. Si and graphite are the major constituents of the graded coating, and the sputter etching rate ratio is assumed to be $\mathrm{Si{:}C} \approx 1{:}1$ for simplicity. The K-alpha spectrometer has aluminum Kα with a pass energy of 50 eV, a measuring spot size of 0.2 mm and an energy step size of 0.1 eV. The atomic ratio of Si2p and C1s at one location can be calculated using the area ratio of each peak measured from XPS, and all peaks are fitted using the XPSPEAK software after the background was subtracted appropriately. The atomic ratio is defined as

$$\frac{N_C}{N_{Si}} = \frac{I_C / S_C}{I_{Si} / S_{Si}} \tag{27}$$

Where I_C, I_{Si}, S_C and S_{Si} are the calculated total peak area of graphite, total peak area of Si, sensitivity factor of C1s and sensitivity factor of Si2p, respectively. $S_C = 0.25$ and S_{Si}=0.27.

Figure 41c shows an example of XPS peak analysis conducted at one location inside the coating (the location shown with a blue arrow in **Figure 41a**. All possible valence states C1s peaks are added and fitted using XPSPEAK software, but no content of C-O is observed and only C-C and C-Si bonds are found in the results. In **Figure 41c**, the total area of the two peaks (C-C and C-Si) is calculated as 35915. While for the same location, the total peak area for Si is 15290. Based on the atomic ratio formula, the atomic ratio of carbon and Si can be calculated as C : Si ≈ 2.53 : 1. Molar volume of carbon is 5.29 cm^3 and molar volume of Si is 12.17 cm^3, and the volume ratio per atom can be calculated as v_C : v_{Si}= 5.29 : 12.17 = 1 : 2.3. Therefore, the volume ratio of carbon and Si at this plane is $V_C : V_{Si}$=1×2.53 : 2.3×1 = 2.53 : 2.3. Finally, the volumetric content of carbon can be calculated as 2.53 / (2.53+2.3) ≈52.4%. Volumetric content of each plane (7 planes in total as shown in **Figure 41a** and **b**) has been calculated and the results are drawn in **Figure 41d**. As can be seen that the measured results agree with the intended linear profile very well, which validates the fact that the refractive index profile of the coating is graded based on the mixture rule mentioned. Note that the volumetric content is calculated under the assumptions that the deposited materials are dense and no gaps are between the atoms, therefore the actual errors might be slightly larger than the results presented. Another thing to note is that at the very outer layer, we can still see a small carbon peak (theoretically it should not exist here) in **Figure 41a**, and the reason is that a thin layer of carbonaceous material is usually found on the surface of most air exposed samples, this layer is generally known as adventitious carbon. Even small exposures to atmosphere can produce these films. Similar situation for the most outer layer of Si peaks as well (**Figure 41b**), oxygen content is observed, and it also comes from the exposures to atmosphere environment. Therefore, at the both ends of the graded coating, no100% carbon nor Si can be reached.

FDTD simulations is also conducted for the focal length validation. A domain of 15 μm × 15 μm × 20 μm with convolutional perfectly matched layer (CPML)[40] conditions on each boundary was adopted at the wavelength of 1000 nm. The refractive indices used for the simulation are n_{PDMS}=1.406, n_{DLC}=1.88 and n_{Si}=3.57, respectively. Figure **40** shows electric fields at the middle symmetric plane of the domain for both pure PDMS lens and PDMS lens with a graded coating. As shown, a 1000 nm wavelength near Infrared Gaussian light is incident on the lens from the top. Figure **40a** presents the beam interact with the pure PDMS lens. Figure **40b** shows the near IR beam interact with the GRIN lens. A clear focal length reduction is observed. The focal length before deposition is around 4.12 μm, very close to the theoretically calculated result 4.5 μm, and the focal length after deposition is around only 2.9 μm. The focal length reduction from the graded coating is calculated to roughly 29.6%, which meets our requirement for the ultrashort focal length.

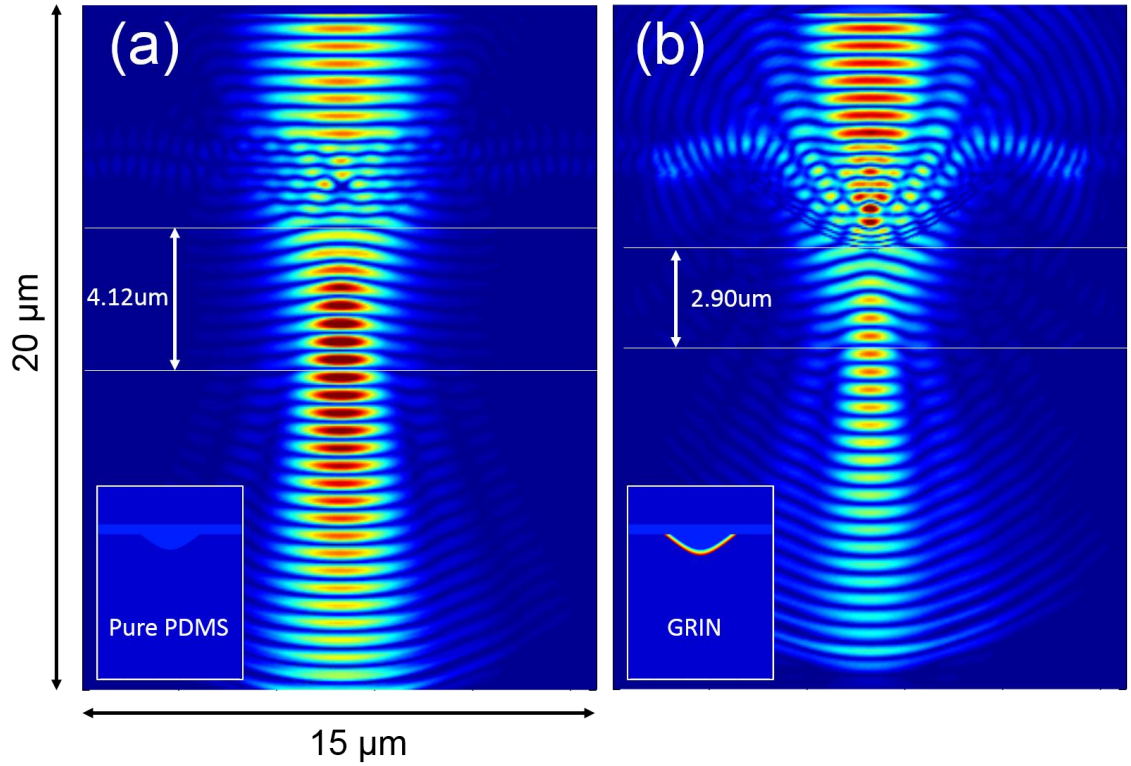

Figure 40. FDTD simulation results with a 1000 nm light on the focal length reduction of the graded coating. (a) pure PDMS lens. (b) PDMS lens with the graded coating.

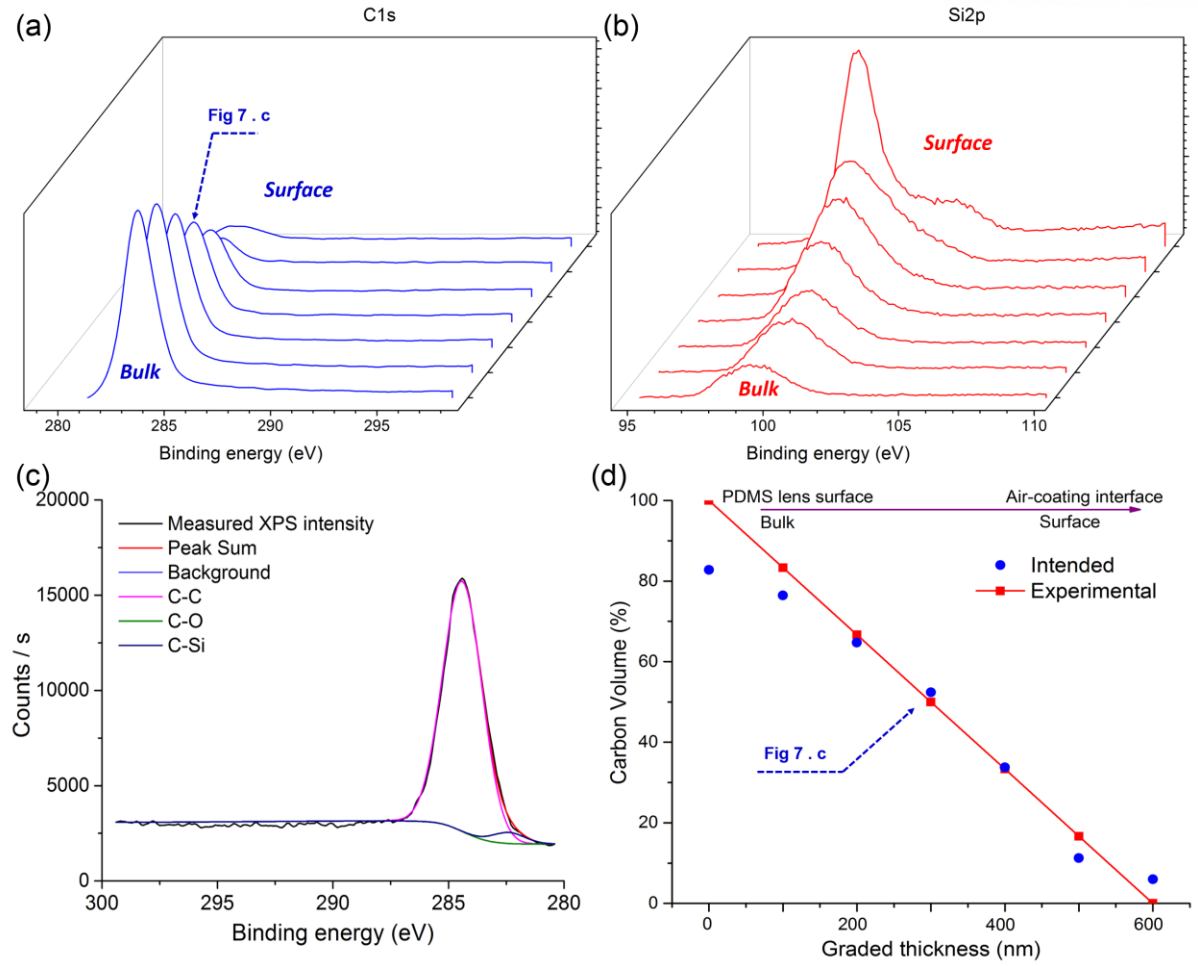

Figure 41. (a) XPS measured C1s peak variation along the coating thickness direction for DLC content; (b) XPS measured Si2p peak variation along the coating thickness direction for Si content; (c) An C1s XPS peak fitting example for the location shown with a blue arrow in (a) and (d); (d) Calculated DLC volume percentage at each location inside the graded coating.

Transmission curves of a pure DLC (~600 nm), pure Si (~600 nm), Pure PDMS (~2 mm) and the graded coating (~600 nm) (each was deposited/fabricated on top of a 0.5mm thick fused silica substrate) are investigated with a UV-VIS-NIR spectrophotometer (Agilent, Cary 5000). And the results are shown in **Figure 42**. Black solid line stands for the transmission curve of PDMS polymer, it is almost always transparent for the whole measured spectrum range; red and green solid lines are the measured transmission values for deposited DLC and Si, respectively. As we can see that Si has larger transmission in the near IR region comparing with DLC, but for both materials, the transmission become very small when the wavelength decreases from near IR to around 700 nm, which is the upper limit for visible light (from 380 nm to 700 nm). Therefore, we can say that both deposited DLC and Si coatings are somehow opaque in the visible light range, and they can be used as a filter to cutoff visible lights while perform well in the near IR region since they have higher transmission in the near IR light range.

The DLC/Si graded coating also exhibits similar properties, thus it can serve for many near IR applications and devices.

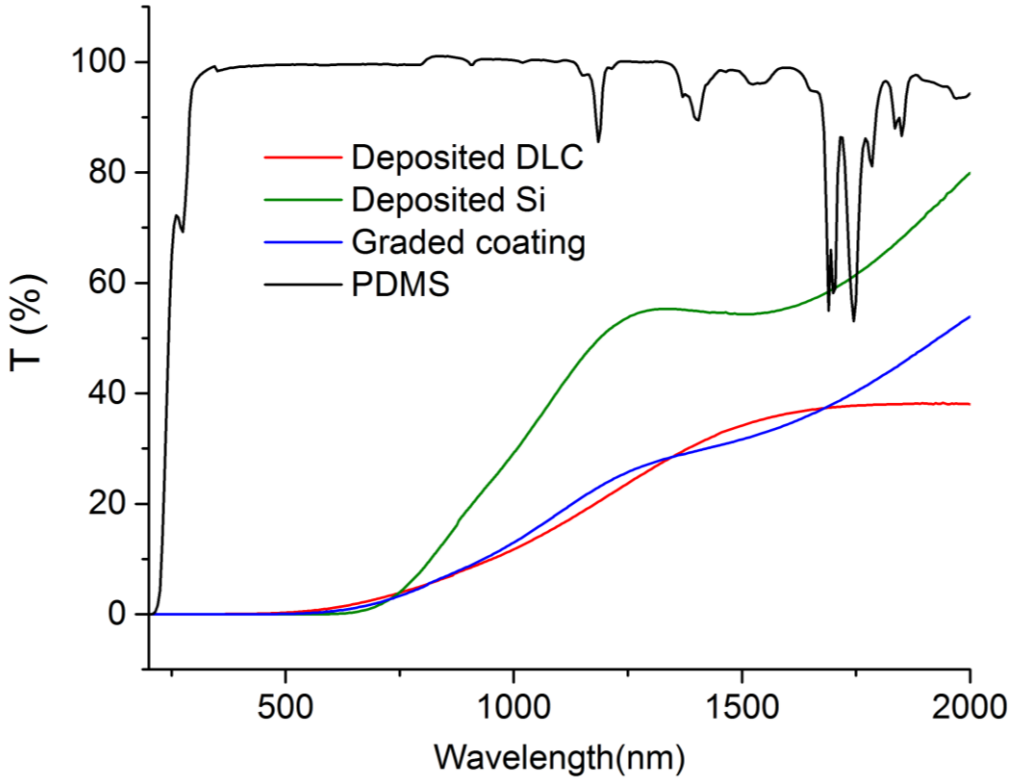

Figure 42. Transmission curves for deposited DLC (red solid line), deposited Si (green solid line), graded coating (blue solid line) and pure PDMS (black solid line) from 200 nm to 2000 nm.

The imaging test for the GRIN lens array is finally conducted with a Total Internal Reflection Microscopy (Olympus) and a Photoactivated Localization Super Resolution Microscopy (Carl Zeiss). The light source of the Total Internal Reflection Microscopy is a Halogen lamp, which contains the lights from visible to near IR range (though most of the visible lights will be blocked due to the extremely low transmission of the graded coating in the visible range). Same "S" letter (as the one for pure PDMS imaging test) is used as the imaging object. As is shown in **Figure 43a**, very clear and crisp image of "S" is presented on every single lenslet. It demonstrates that the fabricated GRIN lenses have very good optical imaging properties under the halogen lamp lights. The light source of a Photoactivated Localization Super Resolution Microscopy uses a monochrome laser beam as the light source. A very clear image of "S" is also formed on each lenslet under the irradiation of a near IR laser (1000 nm). Due to the limitation of the equipment, 1000 nm is the largest monochrome laser wavelength we can use,

but we believe the lens array will perform well for lager near IR wavelengths as well, since the transmission values increases as the wavelengths increase.

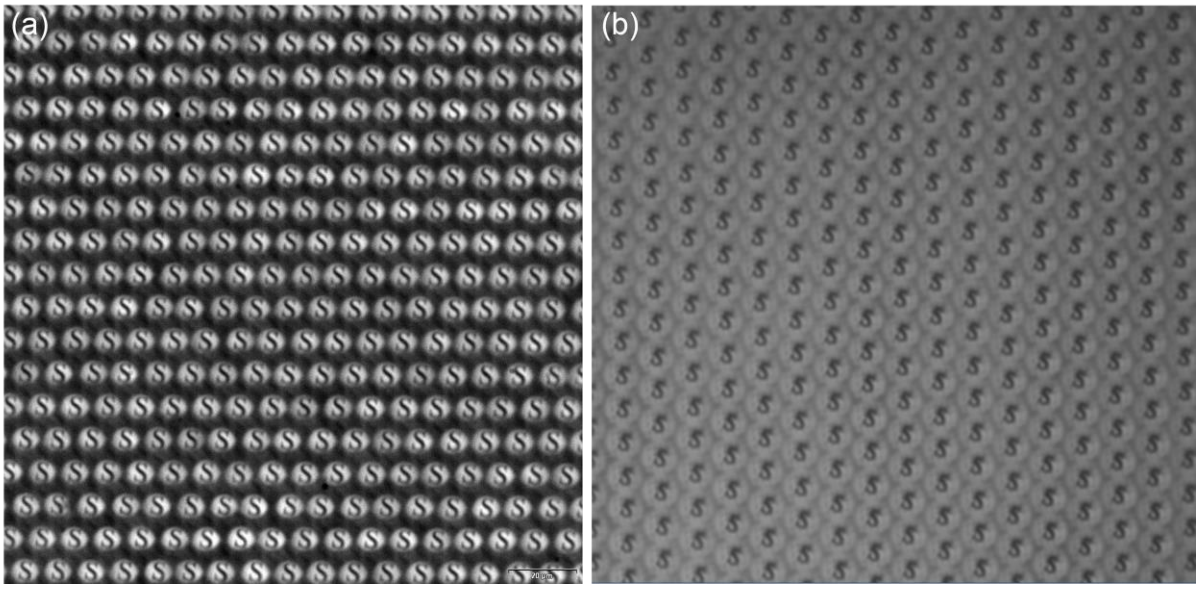

Figure 43. Imaging tests for the GRIN lens array with different microscopies. (a) Image from a Total Internal Reflection Microscopy with a halogen lamp; (b) Image from a Photoactivated Localization Super Resolution Microscopy with a 1000 nm wavelength laser beam.

6.3 Conclusions

In this study, the successful design, fabrication and characterization of an index-graded microlens array with an ultrashort focal length is reported. A 1030 nm femtosecond laser was used to fabricate negative microlens array patterns on a fused silica substrate, then a chemical wet etching process was employed for the negative lens array. The negative microlens array was used as a molding template for duplicating polydimethylsioxane (PDMS) convex microlens arrays. The fabricated positive PDMS microlens array is proved to have an ultrasmall lenslet diameter of ~ 6 μm and a sag height of ~1.6 μm, providing an ultrashort focal length of ~4.12 um and a high N.A value of 0.73. A dual beam pulsed laser deposition was adopted to fabricate a 600 nm graded DLC/Si layer on top of the PDMS microlenses, making the lenses graded and shortening the focal length even more. The lenses after deposition have a smaller focal length of ~ 2.9 μm and a higher N.A of ~1.21. This is the shortest focal length reported, to the best of the authors' knowledge. The focal length is increased by 29.6% and the N.A is increased by ~66% due to the existence of the 600 nm graded coating. The content profile of the graded region is validated with XPS depth profiling analysis, the measured results agree well with design, therefore the graded index profile is expected. Imaging tests were also conducted for the lenses before and after

deposition, clear and uniform images were captured, showing very good optical imaging properties of the lenses. Due to the extremely low transmission in the visible light region but much higher transmission in the near IR region for Si and carbon, the index-graded microlenses are suitable to cutoff visible lights and perform well for near IR lights, therefore they can be used in many near IR applications, such as near-field imaging, fine sampling of an object under consideration in integral imaging microscopy and short wave detectors, etc.

VII. CONCLUSIONS AND FUTURE WORK

7.1 Conclusions

In this research, the authors have discussed the picosecond laser dual beam pulsed laser deposition technique and pulse control scheme for several types of functional graded coating depositions for optical and thermal applications. In Chapter one, the overview of FGMs and PLD and its research background, motivations and literature reviews were presented. Many fabrication methods for thin coating deposition are introduced in this section. In chapter two, we presented our research objectives and our methods, including the experimental setup - dual beam pulsed laser system with a pico/femtosecond laser combined scheme for depositing functionally graded coatings; our theoretical design of fabricating efficient and precise functional graded coatings – the pulse control scheme (attenuators are used to regulate laser beams into desirable pulses of difference lengths for accurate depositions). In chapter 3, an optical design tool for electrodynamic simulations - finite-difference time-domain (FDTD) algorithm for testing the optical coatings. It is an algorithm used for simulating electro-magnetic waves by solving the Maxwell's equations directly. Many optical characteristics can be preserved using this algorithm and accurate electromagnetic wave propagations can be obtained. In the FDTD section, an example of using FDTD for the simulations of keyholes' laser absorption is presented. In chapter 4, the design, fabrication and testing of a broadband antireflection coating for silicon based solar cell is presented. Glass-Si graded antireflection coatings are achieved by the design scheme and pulse control technique fore-mentioned, and its antireflection characteristics are measured with spectrometers and validated using FDTD simulations. In chapter 5, YSZ/SUS graded thermal barrier coating is introduced with the same fabrication techniques. Its thermal barrier effect is tested with a laser flash method with an infrared thermal camera and adhesion strength is tested with indentation cracking method. And in chapter 6, we will talk about the design, fabrication and characterization of an ultrashort focal length GRIN microlens array combining both PLD and femtosecond laser micro-fabrication. Its optical properties such as focusing ability and imaging ability are tested and good results are illustrated.

This research presented a novel laser pulse control scheme and pulsed laser deposition technique of some functionally graded coatings in optical or thermal applications. Some conclusions based on some chapters will be listed below.

Keyhole absorption simulation proves that FDTD is a powerful design tool for optical problems

In this section, we discussed the electrodynamic simulation algorithm FDTD and illustrated an example of using FDTD for the simulation of calculating the laser absorption of keyholes during laser

welding. It shows that FDTD is a very powerful tool for electrodynamic simulations. The simulation will mainly be used as a design tool and validation method for the optical graded coatings.

The major findings of this study are summarized as follows:

The FDTD method with the enlarged wavelength scheme was effectively used for keyhole absorption problems. In this study, the keyhole shapes that were measured experimentally were used for simulation, and the beam divergence, polarization and focusing characteristics of the laser were matched. In this way, all the electromagnetic characteristics of the problem were naturally accounted for.

Multiple reflections phenomena occur more conspicuously for the zinc-coated steel. As the energy density decreases, the number of reflections also increases in order to absorb an enough amount of laser energy to sustain a keyhole.

For the uncoated steel, the keyhole absorptance is controlled by the keyhole bottom aperture size.

When the bottom aperture is small, laser energy is highly concentrated around there. In this case, concentrated heating will take place, and the bottom aperture will be forced to open again. This is believed to be the mechanism of the opening and closing of the bottom keyhole aperture.

For uncoated steel, the keyhole absorptance decreases as $I_o t^{1/2}$ increases, and the pattern is very regular. For zinc-coated steel, the keyhole absorptance decreases sharply first, and then increases somewhat to follow the trend of the uncoated steel. The overall pattern is more irregular.

Zinc-coated steel has a much lower keyhole absorptance than uncoated steel at the same experimental condition, which was experimentally validated by melt pool size measurement.

Fabrication of a broadband antireflection coating for Si based solar cells

We have demonstrated index-graded AR coatings and their fabrication method based on the dual-beam pulsed laser deposition with a pulse control technique. The AR coatings were deposited on silicon substrates and the graded index was realized by continuously controlling the volumetric content percentage of silicon and glass along the coating thickness direction based on a mixture rule for refractive index. The fabricated AR coatings show spectral reflectance values of 2.2~5.5% for a wavelength range of 400~1000 nm. In the case of the Southwell profile with a 400nm pure glass layer, the AR performance was found to be 2.2~4%, which can be considered close to the theoretically best performance of silicon-based solar cells with a protective cover glass. Owing to the material choice of

silicon and glass, this antireflection coating can be easily applied to silicon-based solar cells. It can simplify the solar cell structure considerably because from the solar cell to the outer cover glass the composition changes continuously from silicon to glass and the whole structure can be fabricated by one PLD procedure.

Fabrication of a YSZ/steel graded thermal barrier coating for high temperature applications

In this tudy, we have successfully designed and fabricated YSZ-SUS graded coatings by using a dual-beam pulsed laser deposition method and investigated their properties in terms of thermal conductivity and adhesion strength. Deposited YSZ coatings showed a good thermal barrier characteristic (thermal conductivity of ~1.14W/(m·K)) and the graded region provided much improved adhesion strength in comparison to pure YSZ coatings. With further research, we believe that much thicker, industry-scale functionally-graded YSZ coatings (several hundred micrometers thick) could be fabricated based on this approach, if a high-power picosecond laser (say, 500−1000W) is used with a proper scaling-up method.

Fabrication of an ultrashort focal length index-graded microlens array for NIR applications

In this study, the successful design, fabrication and characterization of an index-graded microlens array with an ultrashort focal length is reported. A 1030 nm femtosecond laser was used to fabricate negative microlens array patterns on a fused silica substrate, then a chemical wet etching process was employed for the negative lens array. The negative microlens array was used as a molding template for duplicating polydimethylsioxane (PDMS) convex microlens arrays. The fabricated positive PDMS microlens array is proved to have an ultrasmall lenslet diameter of ~ 6 μm and a sag height of ~1.6 μm, providing an ultrashort focal length of ~4.12 um and a high N.A value of 0.73. A dual beam pulsed laser deposition was adopted to fabricate a 600 nm graded DLC/Si layer on top of the PDMS microlenses, making the lenses graded and shortening the focal length even more. The lenses after deposition have a smaller focal length of ~ 2.9 μm and a higher N.A of ~1.21. This is the shortest focal length reported, to the best of the authors' knowledge. The focal length is increased by 29.6% and the N.A is increased by ~66% due to the existence of the 600 nm graded coating. The content profile of the graded region is validated with XPS depth profiling analysis, the measured results agree well with design, therefore the graded index profile is expected. Imaging tests were also conducted for the lenses before and after deposition, clear and uniform images were captured, showing very good optical imaging properties of the lenses. Due to the extremely low transmission in the visible light region but much higher

transmission in the near IR region for Si and carbon, the index-graded microlenses are suitable to cutoff visible lights and perform well for near IR lights, therefore they can be used in many near IR applications, such as near-field imaging, fine sampling of an object under consideration in integral imaging microscopy and short wave detectors, etc.

7.2 Future work

Due to the defocusing effect caused by the material ablation during the deposition, we have to shift the target materials in order to maintain continuous and strong plasmas, and this issue can be resolved with a dynamic control of the target holders. This could be a possible work for future, in order to improve the deposition process. However, during my last project of microlens array fabrication, I have grown interest in micro/nano fabrication, surface texturing, micro/nano optics, etc. Hense I'd like to do more related work in those area in the future.

REFERENCES

1. Koizumi, M., *FGM activities in Japan.* Composites Part B-Engineering, 1997. **28**(1-2): p. 1-4.
2. Pindera, M.J., et al., *Use of Composites in Multi-Phased and Functionally Graded Materials.* Composites Engineering, 1995. **5**(7): p. R7-R9.
3. Koizumi, M. and M. Niino, *Overview of Fgm Research in Japan.* Mrs Bulletin, 1995. **20**(1): p. 19-21.
4. Pindera, M.J., et al., *Use of Composites in Functionally Graded Materials - Invited Papers - Functionally Graded, Advanced Composites Materials Symposium University-of-Virginia, Charlottesville, USA - 6-9 June 1993 - Foreword.* Composites Engineering, 1994. **4**(1): p. R7-R9.
5. Erdogan, F. and B.H. Wu, *Crack problems in FGM layers under thermal stresses (vol 19, pg 237, 1996).* Journal of Thermal Stresses, 1997. **20**(3-4): p. 437-437.
6. Birman, V. and L.W. Byrd, *Modeling and analysis of functionally graded materials and structures.* Applied Mechanics Reviews, 2007. **60**(1-6): p. 195-216.
7. Gupta, A. and M. Talha, *Recent development in modeling and analysis of functionally graded materials and structures.* Progress in Aerospace Sciences, 2015. **79**: p. 1-14.
8. Jha, D.K., T. Kant, and R.K. Singh, *A critical review of recent research on functionally graded plates.* Composite Structures, 2013. **96**: p. 833-849.
9. Tsui, Y.C., S.J. Howard, and T.W. Clyne, *The Effect of Residual-Stresses on the Debonding of Coatings .2. An Experimental-Study of a Thermally Sprayed System.* Acta Metallurgica Et Materialia, 1994. **42**(8): p. 2837-2844.
10. Howard, S.J., Y.C. Tsui, and T.W. Clyne, *The Effect of Residual-Stresses on the Debonding of Coatings .1. A Model for Delamination at a Bimaterial Interface.* Acta Metallurgica Et Materialia, 1994. **42**(8): p. 2823-2836.
11. Fukui, Y., *Fundamental Investigation of Functionally Gradient Material Manufacturing System Using Centrifugal Force.* Jsme International Journal Series Iii-Vibration Control Engineering Engineering for Industry, 1991. **34**(1): p. 144-148.
12. Bunshah, R.F., *Handbook of Deposition Technologies for Films and Coatings*. 2nd Edition ed. 1994, Park Ridge,N J: Noyes Publications.
13. Groves, J.F. and H.N.G. Wadley, *Functionally graded materials synthesis via low vacuum directed vapor deposition.* Composites Part B-Engineering, 1997. **28**(1-2): p. 57-69.
14. Jin, G., et al., *Properties of multilayered mullite/Mo functionally graded materials fabricated by powder metallurgy processing.* Materials Chemistry and Physics, 2005. **89**(2-3): p. 238-243.
15. Lin, C.Y., et al., *Production of silicon carbide Al 2124 alloy functionally graded materials by mechanical powder metallurgy technique.* Powder Metallurgy, 1999. **42**(1): p. 29-33.

16. Zhu, J.C., et al., *Fabrication of ZrO2-NiCr functionally graded material by powder metallurgy.* Materials Chemistry and Physics, 2001. **68**(1-3): p. 130-135.
17. Zhang, W.F., et al., *Microstructure and resisting thermal shock behaviors of TiC-Al2O3/Fe functionally graded materials prepared by SHS/PHIP.* Journal of Materials Science & Technology, 2001. **17**(1): p. 65-66.
18. Choi, K.H., et al., *High-Temperature Thermo-Mechanical Behavior of Functionally Graded Materials Produced by Plasma Sprayed Coating: Experimental and Modeling Results.* Metals and Materials International, 2016. **22**(5): p. 817-824.
19. Lowndes, D.H., et al., *Synthesis of novel thin-film materials by pulsed laser deposition.* Science, 1996. **273**(5277): p. 898-903.
20. Smith, H.M. and A.F. Turner, *Vacuum Deposited Thin Films Using a Ruby Laser.* Applied Optics, 1965. **4**(1): p. 147-&.
21. Vaziri, M.R.R., F. Hajiesmaeilbaigi, and M.H. Maleki, *Microscopic description of the thermalization process during pulsed laser deposition of aluminium in the presence of argon background gas.* Journal of Physics D-Applied Physics, 2010. **43**(42).
22. Ong, C.K., S.Y. Xu, and W.Z. Zhou, *A novel approach for doping impurity in thin film in situ by dual-beam pulsed-laser deposition.* Review of Scientific Instruments, 1998. **69**(10): p. 3659-3661.
23. Gusarov, A.V. and I. Smurov, *Gas-dynamic boundary conditions of evaporation and condensation: Numerical analysis of the Knudsen layer.* Physics of Fluids, 2002. **14**(12): p. 4242-4255.
24. Kelly, R. and B. Braren, *On the Direct Observation of the Gas-Dynamics of Laser-Pulse Sputtering of Polymers .1. Analytical Considerations.* Applied Physics B-Photophysics and Laser Chemistry, 1991. **53**(3): p. 160-169.
25. Gamaly, E.G., A.V. Rode, and B. Luther-Davies, *Ultrafast ablation with high-pulse-rate lasers. Part I: Theoretical considerations.* Journal of Applied Physics, 1999. **85**(8): p. 4213-4221.
26. Rode, A.V., B. Luther-Davies, and E.G. Gamaly, *Ultrafast ablation with high-pulse-rate lasers. Part II: Experiments on laser deposition of amorphous carbon films.* Journal of Applied Physics, 1999. **85**(8): p. 4222-4230.
27. Cho, H., S. Kim, and H. Ki, *Pulsed laser deposition of functionally gradient diamond-like carbon (DLC) films using a 355 nm picosecond laser.* Acta Materialia, 2012. **60**(18): p. 6237-6246.
28. Deng, C. and H. Ki, *Pulsed laser deposition of refractive-index-graded broadband antireflection coatings for silicon solar cells.* Solar Energy Materials and Solar Cells, 2016. **147**: p. 37-45.
29. Nelder, J.A., *Inverse Polynomials a Useful Group of Multi-Factor Response Functions.* Biometrics, 1966. **22**(1): p. 128-&.

30. Won, Y.J. and H. Ki, *Fabricating functionally graded films with designed gradient profiles using pulsed laser deposition.* Journal of Applied Physics, 2013. **113**(17).
31. Ki, H. and J. Mazumder, *Numerical simulation of femtosecond laser interaction with silicon.* Journal of Laser Applications, 2005. **17**(2): p. 110-117.
32. Deng, C., et al., *Electrodynamic simulation of energy absorption in laser keyhole welding of zinc-coated and uncoated steel sheets.* Journal of Materials Processing Technology, 2016. **231**: p. 412-421.
33. Abderrazak, K., et al., *Numerical and experimental study of molten pool formation during continuous laser welding of AZ91 magnesium alloy.* Computational Materials Science, 2009. **44**(3): p. 858-866.
34. Graf, S., et al., *Generation of a dynamic polarized laser beam for applications in laser welding.* Journal of Applied Physics, 2010. **107**(4).
35. Hadi, I., *Mathematical estimation of melt depth in conduction mode of laser spot remelting process.* Journal of Applied Physics, 2012. **112**(12).
36. Wei, P.S., et al., *Origin of wavy weld boundary.* Journal of Applied Physics, 2009. **105**(5).
37. Deng, C. and H. Ki, *FDTD method for laser absorption in metals for large scale problems.* Optics Express, 2013. **21**(21): p. 25467-25479.
38. Deng, C. and H. Ki, *Finite-difference time-domain simulation of laser beam absorption in fully penetrated keyholes.* Journal of Applied Physics, 2013. **114**(16): p. 164901.
39. Kim, J., S. Oh, and H. Ki, *A study of keyhole geometry in laser welding of zinc-coated and uncoated steels using a coaxial observation method.* Journal of Materials Processing Technology, 2015(submitted).
40. Roden, J.A. and T. Kramer, *The Convolutional PML For FDTD Analysis: Transient Electromagnetic Absorption from DC to Daylight.* 2011 Ieee International Symposium on Electromagnetic Compatibility (Emc), 2011: p. 892-898.
41. Siegman, A.E., *Lasers*. 1986, USA: University Science Books.
42. Walheim, S., et al., *Nanophase-separated polymer films as high-performance antireflection coatings*. Science, 1999. **283**(5401): p. 520-522.
43. Steen, W.M. and J. Mazumder, *Laser material processing*. 4th ed. 2010, London: Springer-Verlag.
44. Sohail, M., et al., *Numerical investigation of energy input characteristics for high-power fiber laser welding at different positions.* International Journal of Advanced Manufacturing Technology, 2015. **80**(5-8): p. 931-946.
45. Kim, J. and H. Ki, *Scaling law for penetration depth in laser welding.* Journal of Materials Processing Technology, 2014. **214**(12): p. 2908-2914.
46. Nava, G., et al., *Scaling of black silicon processing time by high repetition rate femtosecond lasers.* Optical Materials Express, 2013. **3**(5): p. 612-623.

47. Bouhafs, D., et al., *Design and simulation of antireflection coating systems for optoelectronic devices: Application to silicon solar cells.* Solar Energy Materials and Solar Cells, 1998. **52**(1-2): p. 79-93.
48. Zhang, G.F., et al., *Studies on Diamond-Like Carbon-Films for Antireflection Coatings of Infrared Optical-Materials.* Journal of Applied Physics, 1994. **76**(2): p. 705-707.
49. Chhajed, S., et al., *Nanostructured multilayer graded-index antireflection coating for Si solar cells with broadband and omnidirectional characteristics.* Applied Physics Letters, 2008. **93**(25).
50. Heller, W., *Remarks on Refractive Index Mixture Rules.* Journal of Physical Chemistry, 1965. **69**(4): p. 1123-&.
51. K. Mogi, T. Ogiwara, and M. Suzuki, *Sputtering Etching Rate Ratio of Si to SiO_2 using Mesh-Replica Method.* Journal of Surface Analysis, 2002. **9**(4): p. 514-523.
52. Franssila, S., *Introduction to Microfabrication*. 2 ed. 2010, The Atrium Southern Gate, Chichester West Sussex PO19 8SQ, United Kingdom: John Wiley & Sons, Ltd.
53. Vorobyev, A.Y. and C.L. Guo, *Antireflection effect of femtosecond laser-induced periodic surface structures on silicon*. Optics Express, 2011. **19**(19): p. A1031-A1036.
54. Nath, S., I. Manna, and J.D. Majumdar, *Compositionally Graded Thermal Barrier Coating by Hybrid Thermal Spraying Route and its Non-isothermal Oxidation Behavior.* Journal of Thermal Spray Technology, 2013. **22**(6): p. 901-917.
55. Yao, J.Q., et al., *Thermal barrier coatings with (Al2O3-Y2O3)/(Pt or Pt-Au) composite bond coat and 8YSZ top coat on Ni-based superalloy.* Applied Surface Science, 2013. **286**: p. 298-305.
56. Bolcavage, A., et al., *Thermal shock testing of thermal barrier coating/bondcoat systems.* Journal of Materials Engineering and Performance, 2004. **13**(4): p. 389-397.
57. Rico, A., et al., *Mechanical properties of thermal barrier coatings after isothermal oxidation. Depth sensing indentation analysis.* Surface & Coatings Technology, 2009. **203**(16): p. 2307-2314.
58. Busso, E.P., et al., *A physics-based life prediction methodology for thermal barrier coating systems.* Acta Materialia, 2007. **55**(5): p. 1491-1503.
59. Pan, W., et al., *Low thermal conductivity oxides.* Mrs Bulletin, 2012. **37**(10): p. 917-922.
60. Lee, W.Y., et al., *Concept of functionally graded materials for advanced thermal barrier coating applications.* Journal of the American Ceramic Society, 1996. **79**(12): p. 3003-3012.
61. Farimani, M.R. and M. Mohadeszadeh, *Thermo-elastic bending analysis of FGM rotating plate with axial grading and modified rule of mixture.* Journal of the Brazilian Society of Mechanical Sciences and Engineering, 2017. **39**(1): p. 299-307.
62. Parker, W.J., et al., *Flash Method of Determining Thermal Diffusivity, Heat Capacity, and Thermal Conductivity.* Journal of Applied Physics, 1961. **32**(9): p. 1679-&.

63. Jindal, P.C., D.T. Quinto, and G.J. Wolfe, *Adhesion Measurements of Chemically Vapor-Deposited and Physically Vapor-Deposited Hard Coatings on Wc-Co Substrates.* Thin Solid Films, 1987. **154**(1-2): p. 361-375.
64. Mehrotra, P.K. and D.T. Quinto, *Techniques for Evaluating Mechanical-Properties of Hard Coatings.* Journal of Vacuum Science & Technology a-Vacuum Surfaces and Films, 1985. **3**(6): p. 2401-2405.
65. Ottevaere, H., et al., *Comparing glass and plastic refractive microlenses fabricated with different technologies.* Journal of Optics a-Pure and Applied Optics, 2006. **8**(7): p. S407-S429.
66. Borrelli, N.F., et al., *Photolytic Technique for Producing Microlenses in Photosensitive Glass.* Applied Optics, 1985. **24**(16): p. 2520-2525.
67. Oikawa, M., et al., *Array of Distributed-Index Planar Micro-Lenses Prepared from Ion-Exchange Technique.* Japanese Journal of Applied Physics, 1981. **20**(4): p. L296-L298.
68. Gale, M.T., *Micro-optics: Elements, Systems and Applications*. 1st ed, ed. H.P. Herzig. 1997 Replication, London: Taylor and Francis.
69. Wakaki, M., Y. Komachi, and G. Kanai, *Microlenses and microlens arrays formed on a glass plate by use of a CO2 laser.* Applied Optics, 1998. **37**(4): p. 627-631.
70. Popovic, Z.D., R.A. Sprague, and G.A.N. Connell, *Technique for Monolithic Fabrication of Microlens Arrays.* Applied Optics, 1988. **27**(7): p. 1281-1284.
71. Jay, T.R. and M.B. Stern, *Preshaping Photoresist for Refractive Microlens Fabrication.* Optical Engineering, 1994. **33**(11): p. 3552-3555.
72. Croutxe-Barghorn, C., O. Soppera, and D.J. Lougnot, *Fabrication of refractive microlens arrays by visible irradiation of acrylic monomers: influence of photonic parameters.* European Physical Journal-Applied Physics, 2001. **13**(1): p. 31-37.
73. Naessens, K., et al., *Direct writing of microlenses in polycarbonate with excimer laser ablation.* Applied Optics, 2003. **42**(31): p. 6349-6359.
74. Macfarlane, D.L., et al., *Microjet Fabrication of Microlens Arrays.* Ieee Photonics Technology Letters, 1994. **6**(9): p. 1112-1114.
75. Beinhorn, F., et al., *Micro-lens arrays generated by UV laser irradiation of doped PMMA.* Applied Physics a-Materials Science & Processing, 1999. **68**(6): p. 709-713.
76. Yuan, W., et al., *Fabrication of Microlens Array and Its Application: A Review.* Chinese Journal of Mechanical Engineering, 2018. **31**(1).
77. Fu, Y.Q. and B.K.A. Ngoi, *Investigation of diffractive-refractive microlens array fabricated by focused ion beam technology.* Optical Engineering, 2001. **40**(4): p. 511-516.
78. Floreano, D., et al., *Miniature curved artificial compound eyes.* Proceedings of the National Academy of Sciences of the United States of America, 2013. **110**(23): p. 9267-9272.

79. Duparre, J.W. and F.C. Wippermann, *Micro-optical artificial compound eyes.* Bioinspiration & Biomimetics, 2006. **1**(1): p. R1-R16.
80. Daly, D., et al., *The Manufacture of Microlenses by Melting Photoresist.* Measurement Science and Technology, 1990. **1**(8): p. 759-766.
81. Chen, F.Z., et al., *Development of a double-sided micro lens array for micro laser projector application.* Optical Review, 2012. **19**(4): p. 238-241.
82. Ye, C.F. and R.R. McLeod, *GRIN lens and lens array fabrication with diffusion-driven photopolymer.* Optics Letters, 2008. **33**(22): p. 2575-2577.
83. He, M., et al., *Single-step fabrication of a microlens array in sol-gel material by direct laser writing and its application in optical coupling.* Journal of Optics a-Pure and Applied Optics, 2004. **6**(1): p. 94-97.
84. Dai, Q., et al., *Ultrasmall Microlens Array Based on Vertically Aligned Carbon Nanofibers.* Small, 2012. **8**(16): p. 2501-2504.
85. Casse, B.D.F., et al., *Nano-optical microlens with ultrashort focal length using negative refraction.* Applied Physics Letters, 2008. **93**(5).
86. Yang, H.H., et al., *High fill-factor microlens array mold insert fabrication using a thermal reflow process.* Journal of Micromechanics and Microengineering, 2004. **14**(8): p. 1197-1204.
87. Lian, Z.J., et al., *Rapid fabrication of semiellipsoid microlens using thermal reflow with two different photoresists.* Microelectronic Engineering, 2014. **115**: p. 46-50.
88. Kim, J.Y., et al., *Directly fabricated multi-scale microlens arrays on a hydrophobic flat surface by a simple ink-jet printing technique.* Journal of Materials Chemistry, 2012. **22**(7): p. 3053-3058.
89. Kim, J.Y., et al., *Hybrid polymer microlens arrays with high numerical apertures fabricated using simple ink-jet printing technique.* Optical Materials Express, 2011. **1**(2): p. 259-269.
90. Jeong, K.H., J. Kim, and L.P. Lee, *Biologically inspired artificial compound eyes.* Science, 2006. **312**(5773): p. 557-561.
91. Bian, H., et al., *Direct fabrication of compound-eye microlens array on curved surfaces by a facile femtosecond laser enhanced wet etching process.* Applied Physics Letters, 2016. **109**(22).
92. Nussbaum, P., et al., *Design, fabrication and testing of microlens arrays for sensors and microsystems.* Pure and Applied Optics, 1997. **6**(6): p. 617-636.

ACKNOWLEDGEMENTS

First and foremost I'd like to express my deepest gratitude to my advisor, Professor Hyungson Ki. It has been an honor to be one of his Ph.D. students. He has taught me, both consciously and unconsciously, how good research work is done. I appreciate all his contributions of time and ideas to make my Ph.D. experience productive and stimulating. The joy and enthusiasm he has for his research was contagious and motivational for me, even during tough times in the Ph.D. pursuit. I am also thankful for the excellent example he has provided as a successful scientist and professor.

Besides my advisor, I would like to thank my reading and oral defense committee members: Prof. Sung-Youb Kim, Prof. Jaesung Jang, Prof. Gun-Ho Kim and Prof. Soon-Yong Kwon for their precious time, interest, helpful comments and insightful questions to help me improve my doctoral dissertation and widen my research from various perspectives. Without their help, this dissertation wouldn't have been possible. I would also like to thank the Department of Mechanical Engineering at UNIST for giving me the opportunity to study in their graduate program.

I'd also like to thank Prof. Ki's group (Laser processing & Multiphysics System Laboratory). The members have contributed immensely to my personal and professional time at UNIST. They have been a source of friendships as well as good advice and collaboration. My time at UNIST was made more enjoyable by them. I am especially grateful for the fun group members who are in grad school with me: Keunhee Lee, Haram Yeo, Sehyeok Oh, Hyeongwon Kim, Hyung Kook Jin and Myeong Gyun Son. I also would like to acknowledge our former graduate students, who I have had the pleasure to work with or alongside: Hongrae Cho, Yoo Jai Won, Sanseo Kim, Sangwoo So and Jaehun Kim, and I very much appreciated their enthusiasm and help.

Lastly, I would like to thank my family for all the love and encouragement. For my parents who raised me with a love of science and supported me unconditionally. For my sister who has been taking care of our parents while I am in another nation and supported me and encouraged me for all my pursuits. Thank you.